Micro-Plasma in Porous Media and Dielectric Barrier Discharges with Advanced Agricultural Applications

by

Kenneth Wesley Engeling

A dissertation submitted in partial fulfillment
of the requirements for the degree of
Doctor of Philosophy
(Nuclear Engineering and Radiological Sciences)
in the University of Michigan
2019

Doctoral Committee:

Professor John E. Foster, Chair
Professor Ronald Gilgenbach
Research Scientist John Hoard
Professor Mark J. Kushner

Kenneth W. Engeling

kenengel@umich.edu

ORCiD: 0000-0003-0408-6510

ACKNOWLEDGEMENTS

I would like to thank all of those that had helped me along the way.

Kenneth Wesley Engeling

September 2019

TABLE OF CONTENTS

LIST OF FIGURES

LIST OF TABLES

ABSTRACT

A range of chemical processing applications feature the passage of process gas through porous media. Such media such as foams with interconnected pores or packed beds of aggregate media are desirable for chemical reactions since the reaction surface area to volume ratio is typically quite high. Applications of such reactors include the removal of volatile organic compounds from flues, plasma treatment of aggregate organic media such as seeds, and low temperature, efficient combustion. Conventional applications featuring packed bed media contain catalytic particles often at high temperature. The chemical reactivity of such porous media can be greatly enhanced non-thermally through the production of plasma in the pores. The plasma electrons drive non-equilibrium chemical reactions allowing for a high degree of reaction selectivity. Such plasmas are also the source of reactive radicals. The production and subsequent propagation of plasma within the pores of such media is not well understood.

The goal of this thesis work is to understand the plasma production process in porous media and the subsequent propagation of the plasma through such media. This work also involves understanding the induced chemical reactivity induced by the propagating plasma. The ultimate goal is to obtain insight into how the plasma imparts reactivity to the flow through gas and how these effects can be controlled. This insight will serve as the basis for optimization of existing packed media plasma reactors and the

development of new, novel sources for a range of applications including chemical processing.

The goal of this study is to generate Micro-Plasmas (MPs) as a function of controlled variables throughout the sub-millimeter media. If the plasma properties may be manipulated, then the application of low temperature plasmas (LTPs) in the modern industrial world will be greatly expanded with chemical processing applications alone.

In this work, the MP was created in a 2-dimensional cell and a 3-dimensional reactor using a pulsed, nanosecond high voltage system. Plasma production and propagation was studied using time-resolved optical techniques and optical emission spectroscopy. In the process of investigation, optical studies had found that the dielectric constant value of the packing media had a great influence on the plasma propagation methods and species production. The higher dielectric had shown more intense filamentary microdischarges (FMs) and produced more species than the lower dielectrics. The FM structure for each of the dielectric materials formed at the initialization of the pulse and then transitioned into surface ionization waves (SIWs). Although the FM structure was more apparent with high dielectrics, both plasma propagation structures were observed.

Species identification was performed using band pass filters and optical emission spectroscopy. Experiments have shown the intensity of the 337.1 nm nitrogen emission band as a function of time through a 2d reactor. A secondary emission peak was observed through the discharge with the inorganic aggregate. The second peak may be corresponded to sheath collapse and then re-expansion, ultimately leading to the additionally observed peak. This secondary peak was not observed with the organic

aggregate material. The unobserved secondary emission here may be related to the off-gassing of the organic aggregate effecting the amount of residual charge and therefore sheath collapse and re-expansion. Additionally any off gassing of the material would locally modify the plasma propagation and formation properties.

Also included are plasma interactions with biological organisms such as a soybean seed. Plasma propagation and formation with organic material was found to slightly vary pulse-to-pulse and this was due to organic material morphology. A modification of germination rates and early root development over a 14-day growth trial were observed. Plasma treatment of the seed was seen to promote various root developmental traits such as the length of the taproot or secondary root development. Lastly, the direct plasma treatment of seeds found increased water uptake. This report sheds light on the effects of the packing aggregate intrinsic properties as well as the biological response of the soybean seed after plasma treatment.

Chapter I

Introduction

1.1 The problem at hand

As the world becomes more populated and as humans effects on the environment become more apparent (e.g. pollution and climate change), technological solutions will likely be necessary to ensure sustainable habitation. Scarcity of clean water, the need for more efficient/low carbon footprint fuels, improved agricultural techniques, chemical processing, and advancements in medical practices are fueling environmentally focused research and development worldwide.[1,2,3] Plasma engineering solutions are presently being investigated to address a range of these environmental problems.

The utilization of plasma, specifically low temperature, atmospheric pressure plasmas as demonstrated on the laboratory scale offers a compelling solution. Moreover since plasmas are produced by electrical energy, plasma solutions can be powered by sustainable, renewable energy sources such as wind, solar and nuclear. In particular, the dielectric barrier discharge (DBD) is a compelling tool for selectable control of reaction chemistry.[4] The novelty of the DBD is related to its capacity to generate non-thermal gas discharges at atmospheric pressures with high efficiency. Since these plasmas can be generated in bounding aggregate or porous media with high surface to volume ratios, they can catalyze surface reactions for enhance efficiency without the need for a physical

catalytic particle otherwise subject to fouling. In order to advance DBD technology, an improved fundamental understanding the formation of micro-plasmas in high surface-to-volume ratio media and the mechanism of plasma propagation through such media is needed.

To date, the underlying physics of micro-plasmas is not well understood.[5] Such discharges have demonstrated the capacity to increase the conversion efficiency of chemical processes while being inherently non-thermal and controllable. Scale up will require an understanding of the propagation mechanism of these discharges. Tu et al published a comprehensive study on discharge sensitivity to aggregate morphology in packed bed DBDs.[6] They also reported on power sensitivity and discharge evolution as inferred optically. Tu also investigated the effect of packing materials on a helium gas feed packed bed dielectric barrier discharge at atmospheric pressure.[7] Their work concluded that solid packing led to a multiple current-peak effect that was ascribed to the enhancement of charge density on the pellet surfaces. The combination of the solid aggregate and plasma additionally had a weak effect on electron temperature and density within the discharge.

1.2 Scope of Thesis

The goals of this dissertation are to improve the fundamental understanding of plasma-surface interactions of micron size discharges through aggregate material. An expansion of the physics involved in micro-plasma formation and propagation is investigated in two- and three-dimensional aggregate media with time-resolved imaging and spectroscopy. Employing a fast camera provided visual observations that were related to the localized plasma physics such as Meek's criterion and localized field enhancements. This dissertation expands upon the previous works by identifying the

transient filamentary micro-discharges and surface ionization waves based upon location, pressure, and localized field enhancement of a two-dimensional packed bed reactor. These observations were compared to a miniature 3-d packed bed reactor for validation of the 2d results. With these characteristics identified, further investigation was performed to identify the species populations within the regions of interest. The importance of differing propagation modes was investigated in an agricultural application (seed aggregate) and how it affected contact angle and water absorption. This work ultimately, provides insight into a laboratory scale growth application of biological organisms.

Chapter II introduces the history of packed bed reactor discharges and micro-plasma formations. The chapter also discusses basic theory of plasma physics of packed bed reactors. A great deal of insight may be found via investigations of the current and voltage plots, time-resolved imaging with known distances, and optical emission spectroscopy techniques. These methods are utilized in this dissertation and discussed in detail. The discussion here focuses on packed bed reactor discharges, streamer formation, and electric field enhancement effects.

Chapter III presents the time-resolved emission and imaging measurements used to understand the discharge formation and propagation in a 2-dimensional cell. Modeling is computed using commercially available ANSYS:Maxwell and the solver *nonPDPSIM*. The system is investigated as a function of dielectric constant, voltage, pressure, and the presence of catalytic particles. Characterization involved time-resolved imaging, utilizing an iCCD camera and software image analysis that characterized two discharge

modes. The results of this section are compared to a custom-built miniature three-dimensional packed bed reactor for validation.

Chapter IV details the evolution of plasma-generated species with inorganic and organic aggregate media in the 2-dimensional cell. The evolution is characterized utilizing an optical emission spectroscopy system. The findings presented in this chapter are presented as a function of time and location within the cell as the nanosecond pulsed discharge travels through the aggregate. The relationship between the species produced and physical aggregate properties is discussed at characteristic locations in the 2D cell. The locations of study were near a positive electrode, negative electrode, and the gap between dielectric-to-dielectric media.

Chapter V provides comparative insight into discharge formation and propagation in organic and inorganic material. The time-resolved imaging experimental campaign presented in Chapter III was reproduced within this chapter. The organic material revealed similar, yet differing transients due to surface effects and provides fundamental knowledge into future applications for the treatment of biological organisms.

Appendix A expands on Chapter V with an application focus. It is essentially an introduction to such an application of micro-plasmas within a packed bed reactor with seeds of the soybean plant as the aggregate. The effect of plasma treatment of seeds (organic aggregate in a packed bed) was assessed by characterizing the seeds post treatment. Here plasma effects on seed physical properties as well as germination rates, root development, and shoot growth are quantified. Studies shown in this portion of the dissertation allude to the application of plasma science on agricultural technology.

1.3 The Impact of the dissertation findings

The ultimate goal of research into micro-plasma discharge is to manage the high current density plasmas with surfaces to enhance and manipulate the formation of a product. Plasma interactions between dielectric aggregate and interstitial spaces are complex. Understanding how the plasma forms and spreads throughout these media provides insight into mechanisms to control the chemical pathways of gas flowing through the aggregate media. These findings may be directly applied to plasma-aided combustion.

1.4 Experimental Set up

1.4.1 2-dimensional cell

A two-dimensional packed bed reactor was utilized to allow for direct imaging of plasma propagation along dielectric surfaces and through interstitial spaces thus providing insight into plasma propagation through packed bed discharges. In three dimensions, the overlapping layers prevent direct imaging of discharge evolution from within as they progress through the media. The two dimensional reactor that was chosen allowed for top-down visual inspection between two, stacked quartz plates with a 2.54 cm x 2.54 cm x 0.375 cm reaction well. The quartz plates were designed within Solidworks and with the drawing shown below in Figure 1-1. The plates had horizontal holes drilled into them to allow for pin electrodes to be mounted as well as feedstock gas and vacuum lines. Holes were on the order of 1.5875 mm with the electrodes and vacuum lines sealed into place with Apiezon Torr-seal putty. A 3 mm thick gasket was placed in between the quartz plates to ensure a vacuum seal for the sub-atmospheric experiments.

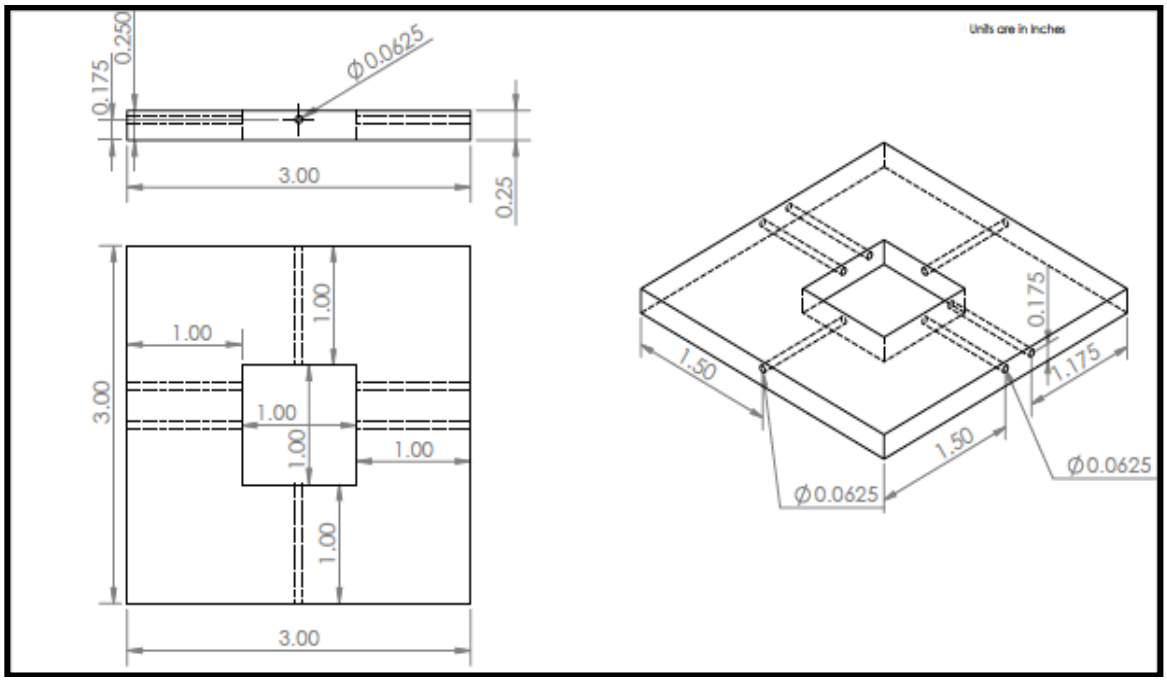

Figure 1-1: SolidWorks schematic of the lower quartz plate utilized in the 2-dimensional experimental setup. Imperial unit dimensions are used in the Solidworks drawing as the manufacturing company required them.

The cell was coupled to a vacuum chamber for evaluation. The base pressure of the chamber was 2.5 x 10^{-5} Torr. The 2-dimensional cell was connected with the Inficon PCG500 (Pirani capacitance manometer gauge) recording a pressure down to 500 mTorr within the reaction chamber cell. Not shown in Figure 1-1 are four vertical through-holes near each of the corners of the quartz plates. The holes were made so that nylon bolts may be inserted and tightened down creating a seal with the gasket.

The 2-dimensional quartz plates and mounting structure was enclosed in a light tight enclosure to prevent the intrusion of ambient light during imaging. Images were acquired using an Andor iStar 334T intensified charge coupled device (iCCD) camera. The electrodes were set up with a pin-to-planar configuration and are discussed in more detail in Chapter III of this text.

1.4.2 Optical Emission Spectroscopy

An investigation of the 2-dimensional setup also included the use of a Princeton Instruments Acton 2300 Spectrometer coupled with a Pi-MAX3 camera. The collected

spectra were analyzed in WinSpec32 software. The spectra were taken at three points of interest for inorganic and organic material. The collected emission was over a 10 ns timeframe that allowed for time-resolved evolution of the discharge and species produced at each of the various locations.

1.4.3 3-dimensional packed bed reactor

The 3-dimensional plasma packed bed dielectric barrier discharge reactor was constructed out of a pyrex tube with stainless steel conflate terminations. The Larson Electronic's glass tubing that was ≈ 20.32 cm in length with a standard 1.33" stainless steel conflat flange attachments on either end of a ≈ 15 cm glass portion. End caps were designed via Solidworks drafting and 3d printed at the University of Michigan CAEN 3d printing laboratory. The electrodes were placed in a coaxial design with a central stainless steel rod of diameter 2.5 mm and a copper mesh electrode enveloping the central 7 cm of glass tubing to act as the negative high voltage terminal. An example of the 3-d PBR with soybean seed as the aggregate material is shown in Figure 1-2.

Figure 1-2: An image capturing the 3-dimensional packed bed reactor filled with soybean aggregate.

The packed bed reactor also had 3d printed 'plugs' that could be inserted into either end of the reactor as 1.5 cm segments. These were printed and implemented to

ensure that the aggregate material was held within the region of plasma formation. The plasma formation within the tube occurred throughout the region within the volume enclosed by the outer copper mesh that served as the grounding electrode. Therefore, aggregate was kept slightly within the edges presented by the copper mesh via the plug inserts.

1.4.4 Aggregate material

A range of dielectric aggregate both organic and inorganic was explored in this work. The 2-dimensional cell experiments utilized zirconia, quartz, and soybean seed. The 3-dimensional cell efforts involved silicon nitride spheres and soybean seed.

1.4.5 Organic material

The interaction of low-temperature plasma with organic media is of great interest in emerging applications such as plasma medicine and agriculture. However the mechanisms involved here are very poorly understood and therefore an organic material such the *Gylcene max* or commonly known as the soybean was investigated.

1.4.6 Joint modeling efforts

Computational modeling performed using nonPDPSIM was carried out by Juliusz Kruszelnicki and supported the experimental effort. The computational experiments provided insight into underlying physics of discharge formation and propagation in the 2D cell. Fields in the 2D cell were also modeled using the commercially available software ANSYS: Maxwell.

1.5 Scope of Dissertation

The scope of this dissertation provides insight into the nature of discharge propagation through dielectric media with direct insight into packed bed discharges, including the effect of dielectric constant of aggregate material, packing fractions,

aggregate morphology, and pressure. The effort also provides insight into application areas such as plasma agriculture. The report provides observation of the propagation mode of the discharge as it spreads throughout the dielectric media including species produced based on location and time of the pulse. The effort utilizes numerical experiments to gain insight into experimental observations as well as guidance for experimental direction.

Chapter II

Micro-Plasmas in Porous Media with Applications to Agriculture: Current Status and Questions to be Answered

2.1 Introduction to micro-plasmas, dielectric barrier discharges, and packed bed reactors

The application of filamentary microdischarges dates back to the work of Siemens who developed dielectric barrier discharges for ozone generation in 1857.[8] Although he did not invent the technology, he was the first to apply it. This apparatus was developed for water treatment. Presently, modern ozonizers are used in water treatment facilities around the world as a form of advanced oxidation.[9] Dielectric barrier discharges feature electrodes in which at least one is covered or obstructed by a dielectric layer. In Siemen's apparatus, air was passed through the annular gap between a central powered electrode and ground, separated by a glass tube. The electrodes powered by alternating high voltage generated the time dependent microdischarges. The air chemistry driven by the plasma is a copious producer of ozone. The dielectric barrier plays a key role in preventing the discharge from developing into an arc. In fact the peak current and thus charge transferred during an active microdischarge is dependent on the capacitance of the apparatus. The barrier therefore prevents the discharge from thermalizing by limiting "on time" as well as protects the electrodes from erosion both plasma chemistry driven and sputtering.[10] The discharge is non-equilibrium with electrons of mean energies of a few

eV and the ions and background gas with temperatures of order 300 K. A typical configuration of an ozonizer is shown in Figure 2-1. These dielectric barrier discharges or DBDs have many applications ranging from gas lasers, to plasma displays, to lighting to the surface modifications of polymers.

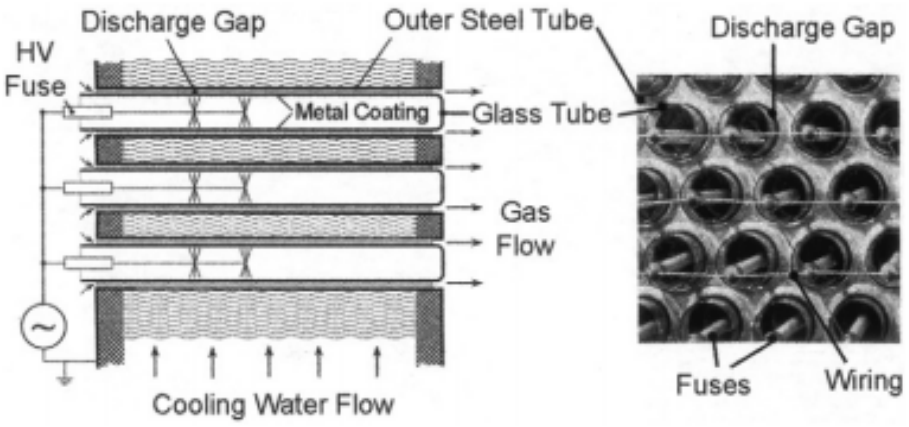

Figure 2-1: Diagram representing a typical layout of a technical ozone generator.[4]

Dielectric barrier discharges can be configured in many ways as shown in Figure 2-2. Discharge gaps are generally on the order of 0.1-10mm. DBDs and other atmospheric plasma sources generally require high voltages for discharge operation, historically with most operating with AC high voltage in the kHz-range. In recent years, pulsed power systems are currently being investigated.[11] Much of this thesis work features pulsed power. The sub-microsecond pulses have also been investigated featuring two breakdowns per pulse–occurring at the rising edge and falling edge of the voltage pulse.[12] It has been shown that the secondary pulse can be attributed to accumulated surface and space charges left by the primary discharge.[13]

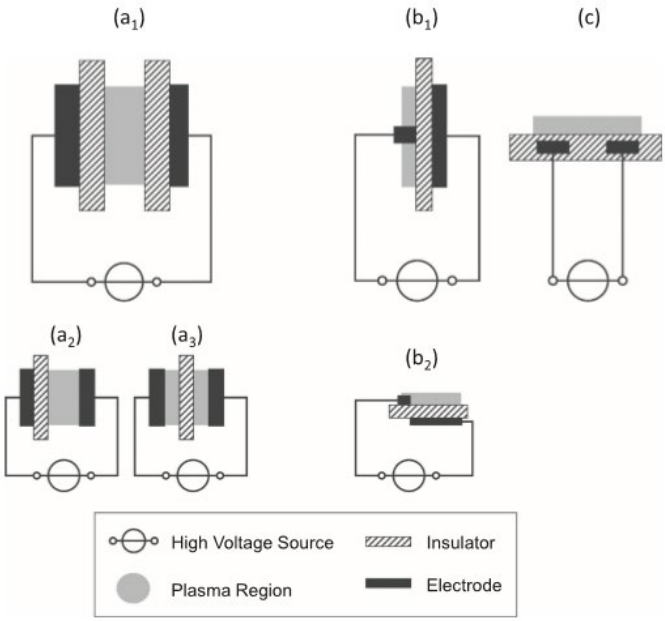

Figure 2-2: Basic planar configurations of DBDs: (a) volume DBD (1-symmetric, 2-symmetric, 3-floated dielectric); (b) surface DBD (1-symmetric, 2-asymmetric 'actuator' design); (c) coplanar discharge.[8]

Electrical diagnostics of DBDs and packed bed reactors can be studied as a lumped-element equivalent circuit. The typical method of power deposition into DBDs powered by a low frequency, AC source utilizes the Lissajous method otherwise known as a Voltage-Charge (V-Q) plot. This approach to the characterization of DBDs was introduced by Manley[14] The reader is referred to this work as well as a review by Pip and Brandenburg for an extensive review of the classical theory and recent developments in the diagnostics of dielectric barrier discharges using the QV method.[15] This method has gained more accurate representations as improvement of experimental techniques and diagnostic equipment are developed. A typical QV-plot results in a parralellogram but new types of QV-plots are seen and may not be explained by classical theory. An example of a parallelogram taken from a sinusoidal voltage-driven ozonizer is shown in Figure 2-3. The classical theory is based upon measurements of applied voltage V(t), current waveform i(t), and charge as a function of the applied voltage Q(V). The charge

as a function of time may be found as an integral of the measured current waveform or can be measured as a voltage drop $V_0(t)$ across a given capacitor C_0.

Equation 1

$$Q(t) = C_0 V_0(t)$$

The charge may also be measured via capacitance and leave a parallelogram as seen in Figure 2-3 (a). Each side of the shape corresponds to one of the discharge phases with the power averaged over the period T, resulting in:

Equation 2

$$P = \frac{1}{T}\oint_T Q(V)dV$$

When the cell does not have an ignited discharge, it behaves as a capacitor, C_{cell}, and can be represented as a serial connection of capacitances associated with a gas gap C_g and dielectric barriers C_d. When the discharge occurs, the plasma connects the electrodes and the dielectric barriers determine the capacitance.

Equation 3

$$C_{cell} = \frac{C_d C_g}{C_d + C_g}$$

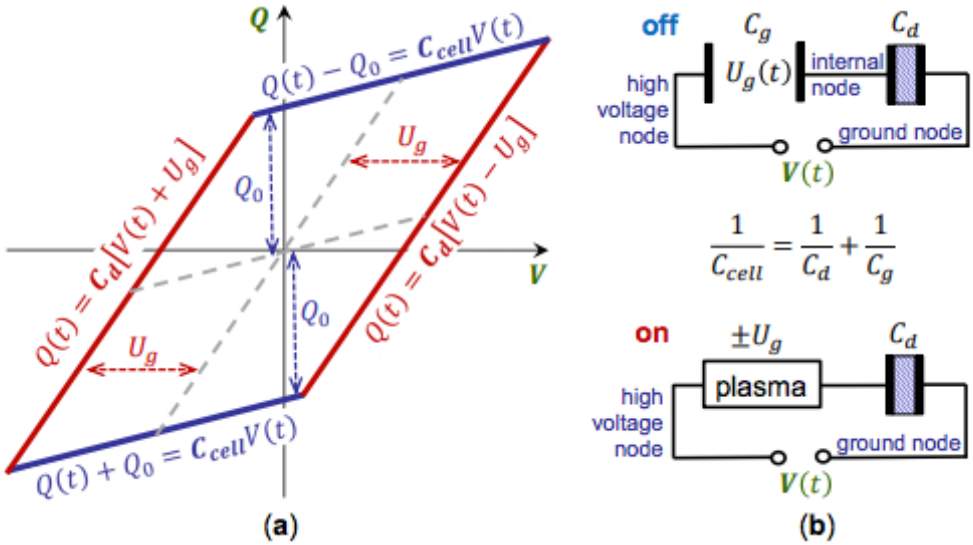

Figure 2-3: Diagrams representing the classical QV-plot on a plasma system with the equivalent circuits represented in (b) with plasma on and plasma off phases.[15]

Another important diagnostic tool is optical emission spectroscopy (OES). OES is a noninvasive diagnostic that provides insight on plasma parameters such as density, effective electron temperature, gas temperature, equilibrium state and excited state distribution. While the diagnostic is relatively straightforward to implement, usually a model is required to interpret the emission spectra collected. Typically a collisional radiative model is required to assess the average electron temperature. The model takes into account the various excitations and ionization processes prevailing in the plasma and allows for the generation of synthetic spectra. By fitting this synthetic spectra to the observed corrected emission spectra, one can determine the electron temperature. Here the electron temperature is the adjustable parameter to facilitate the fit. If one assumes the plasma is in local thermal equilibrium where electron collisions drive a detailed balance wherein excitation and deexcitation is driven by electron impact, then it is possible to estimate the electron temperature via a so-called Boltzmann plot:

Equation 4

$$\ln\left(\frac{I_{ki}\lambda_{ki}}{g_k A_{ki}}\right) = \ln\left(\frac{hcN_o L}{4\pi Z}\right) - \frac{E_k}{k_B T_e}$$

where I_{ki} is the measured intensity, λ_{ki} is the wavelength, g_k is the degeneracy, A_{ki} is the Einstein coefficient, h is Planck's constant, c is the speed of light, L is the optical length of the plasma, N_o/Z is a constant, E_k is the energy of level k, k_B is the Boltzmann constant, and T_e is the electron temperature. The electron temperature is determined from the slope of a plot of the corrected intensity versus level energy. In most atmospheric pressure plasmas, local thermal equilibrium does not prevail and thus this method can only be used to assess qualitative trends. Figure 2-4 depicts a Boltzmann plot for a neon plasma.

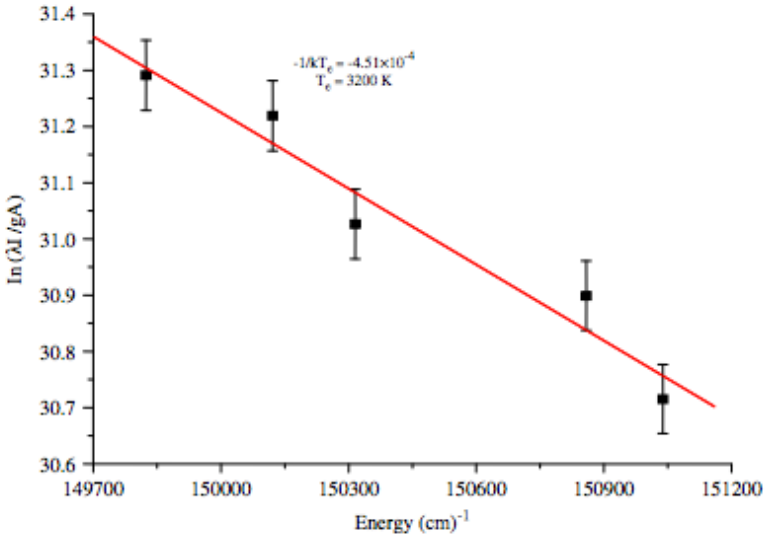

Figure 2-4: Atomic Boltzmann line plot for neon gas.

The line-ratio technique is based upon experimental excited levels and the CRM is employed to generate a line of best fit. The line of best fit is chosen by inputting discharge parameters, gas temperature, and species involved. These techniques are discussed in detail by Zhu et al.,[16] A selection of using the various line ratio methods is dependent upon the pressure and ionization ratio and the reader is referred to Zhu's work for an in-depth review beyond the scope of this work.

2.2 Brief overview of experimental efforts to date

One common dielectric barrier discharge (DBD) is the packed bed reactor (PBRs). Such a configuration consists of dielectric aggregate between electrodes. The configuration is ideal for the treatment of process gases.[17] These systems generally utilize a DC (direct current), AC (alternating current), or a nanosecond-pulsed power source in order to generate plasma. The electrical geometry of dielectric barrier discharges is generally configured either coaxial or planar. The coaxial setup consists of a central, rod electrode and a mesh electrode on the outside of a dielectric tube usually glass or quartz. A diagram representing a packed bed reactor is shown in Figure 2-5.[18]

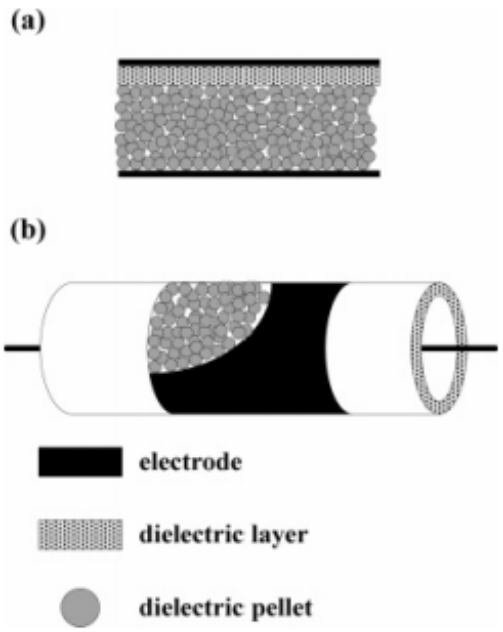

Figure 2-5: Diagram representing a common setup style for a packed bed dielectric barrier discharge reactor.

The space between the rod and the inner wall of the tube is filled with dielectric aggregate. Upon application of high voltage, the field is enhanced near the bounding surfaces of high K dielectric aggregate. When the field satisfies the Meek's Criterion[19,20] the streamer mechanism persists but is typically terminated prematurely owing to discharge contact with bounding dielectric surfaces.

A planar packed bed DBD reactor consists of plate electrodes whose inter-electrode gap is filled with dielectric packing aggregate. Process gas flows through the interstitial spaces and is treated by the plasma discharge in those regions. Whether cylindrical or planar, conversion efficiencies are enhanced not only due to plasma chemistry driven in the interstitial spaces but also due reactions catalyzed on the surface on the aggregate by the plasma and high fields there.[21] Figure 2-2 represents variations of basic planar configurations taken from Brandenburg's work.

Tu and colleagues compared DBD reactors with and without aggregate (alumina in this case).[22] They found that the number of current peaks tripled over the frequency of

30-70 kHz whenever aggregate was in the reactor. Not only were the current spikes higher but also the average temperature within the reactor was 5-10 °C lower at the same input power when aggregate was presented. Additionally they reported that the average electron density was ≈ 2x greater than without the packing aggregate.

Modeling and experimental efforts show opportunities for manipulation of streamer formation and propagation as well as surface ionization waves based upon the dielectric aggregate used as the packing medium. For instance, Butterworth, Elder, and Allen demonstrated that the particle size of Al_2O_3 (aluminum oxide) and $BaTiO_3$ (barium titanate) had an effect on the reduction of CO_2.[23] They showed that the highest conversion was found with Al_2O_3 aggregate particles with characteristic sizes ranging between 180-300 μm. Nguyen et al studied DBDs as a function of relative humidity for the decomposition of toluene and CO_2 selectivity.[24] A reaction chamber's relative humidity of 20% was determined to be ideal. The complexity of the reaction kinetics was shown with the differing specific energies with higher energies generating higher densities of ozone and limiting the desired reactions. In addition to traditional DBDs, adding packing aggregate such as glass beads has been shown to have an effect on the waste conversion.[25,26]

Butterworth and Allen attempted to isolate dielectric aggregate effects by simplifying the packed bed reactor to a single spherical pellet, placed between two planar electrodes within a quartz glass reactor.[27] Discharge morphology and power dissipation were studied as a function of dielectric constant. The equivalent circuit model is for this system is relatively straightforward. Once again, the discharge cell capacitance can be

described by equation 5 where the capacitance of the cell C_{cell}, the capacitance of the dielectric material C_{diel}, and the capacitance of the gap C_{gap}:

Equation 5

$$\frac{1}{C_{cell}} = \frac{1}{C_{diel}} + \frac{1}{C_{gap}}$$

A representation of the equivalent circuit is shown in Figure 2-6 with the Q-V plot. The group was able to show that discharge ignition occurred at lower voltages with higher dielectric constant media. This dependence is attributed to the enhanced E field with the higher K materials.

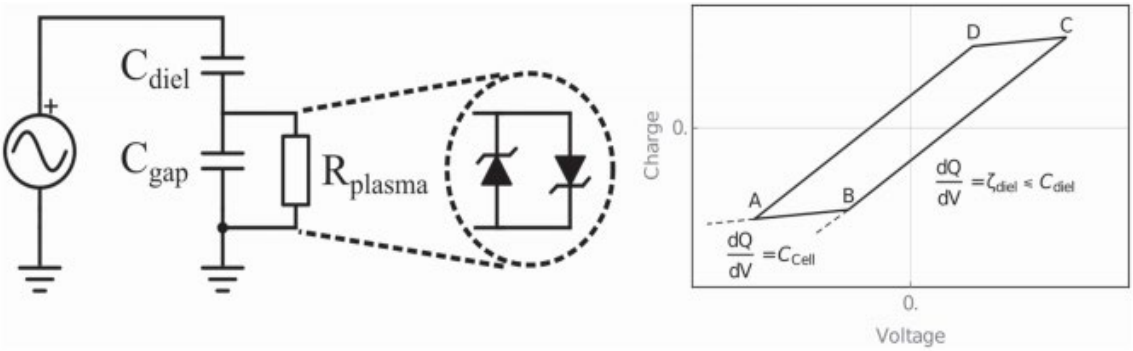

Figure 2-6: Classic equivalent circuit model shown by Butterworth et al. in their work.

This effort also correlated discharge morphology energy consumed per cycle with applied voltage. They were able to identify a number of discharge regimes and the associated transitions to these regimes. These variations are depicted in Figure 2-7.

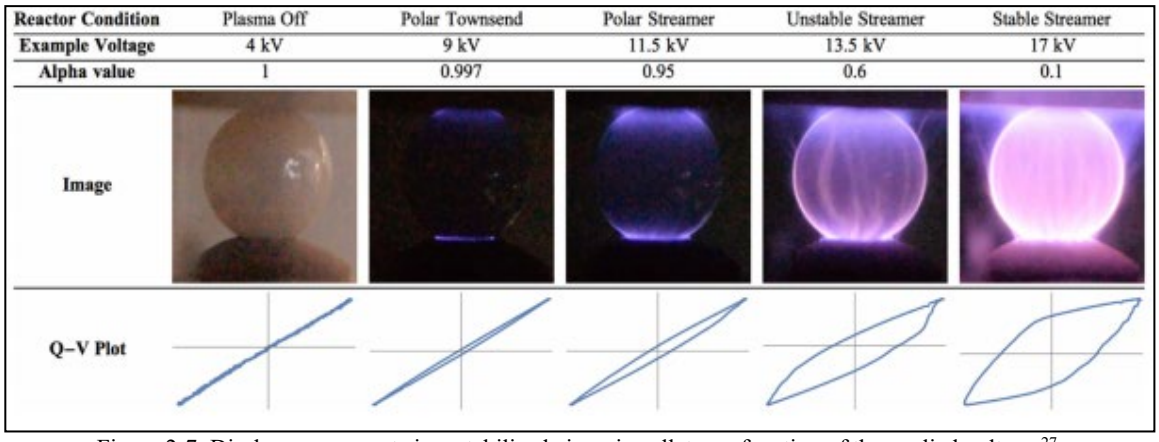

Figure 2-7: Discharge across ytrrium stabilized zirconia pellet as a function of the applied voltage.[27]

This work suggests that it is important to identify the type of discharge prevailing in the cell if ones goal is to optimize overall discharge performance to include surface catalysis augmented by the plasma.

2.3 Review of 0-D, 2-D, and 3-D kinetic modeling of microplasma systems

Packed bed DBDs are numerically simulated using a number of approaches. These models include 0-D, 1-D, 2-D, and 3-D types. The zero dimensional model ZDPlaskin is a plasma kinetics solver.[28] The model uses BOLSIG+ to solve the electron Boltzmann equation:

Equation 6

$$\frac{\partial f}{\partial t} + \vec{v} \cdot \nabla f - \frac{e}{m}\vec{E} \cdot \nabla_v f = C[f]$$

where f is the electronic energy distribution function (EEDF), v is the electronic speed vector, E is the electric field vector, C[f] accounts for changes in f due to collisions, e is the electron charge, and m is the electron mass.[28] The electronic Boltzmann equation is then coupled to a kinetic model describing the state of the plasma mixture. Species concentrations are then iteratively updated as a function of time-steps and provide insight into overall population densities.

Two-dimensional models are advantageous because they provide spatial and temporal insight into plasma production, propagation, and species production without the expensive efforts of 3-dimensional modeling. Within 2-D models, Poisson and Vlasov equations are solved in a steady state in an iterative process.[29] In some cases many assumptions about the plasma is made in order to simplify the computational load on the plasma. This work is complemented by a 2d model called *nonPDPSIM* developed by Mark Kushner, which is discussed in some detail in Chapter III.

Bogaerts and colleagues have also developed a 2D axisymmetric fluid model using the COMSOL Multiphysics Simulation platform.[30] Model results from this group agrees well with experimental findings described within this dissertation such as streamer propagation, localized electric field enhancements as shown in Figure 2-8, and filamentary micro-discharges and surface ionization waves.[32]

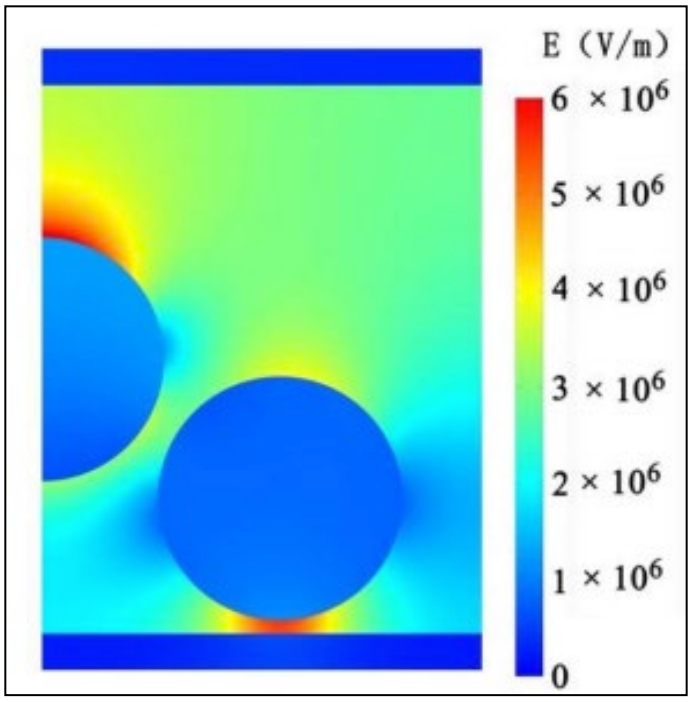

Figure 2-8: Planar view of the localized electric field enhancement in a packed bed reactor for a dielectric constant of 5.[36]

Their work also included comparison between various packing fractions. The simplified model only employed a list of 23 reaction mechanisms with the helium gas.[31] Within this work a 'contact point model' was investigated in which some of the dielectric beads were physically touching. It was found that wherever the pellets are in direct contact plasma formation and propagation was no longer favorable. Therefore plasma forms in the region in between the pellets where electric field enhancement is still high but the gap distance between the beads is enough for Paschen's Law to be satisfied and

plasma formation occurs. Their findings involving the gap formation with contacting beads is shown in Figure 2-9.

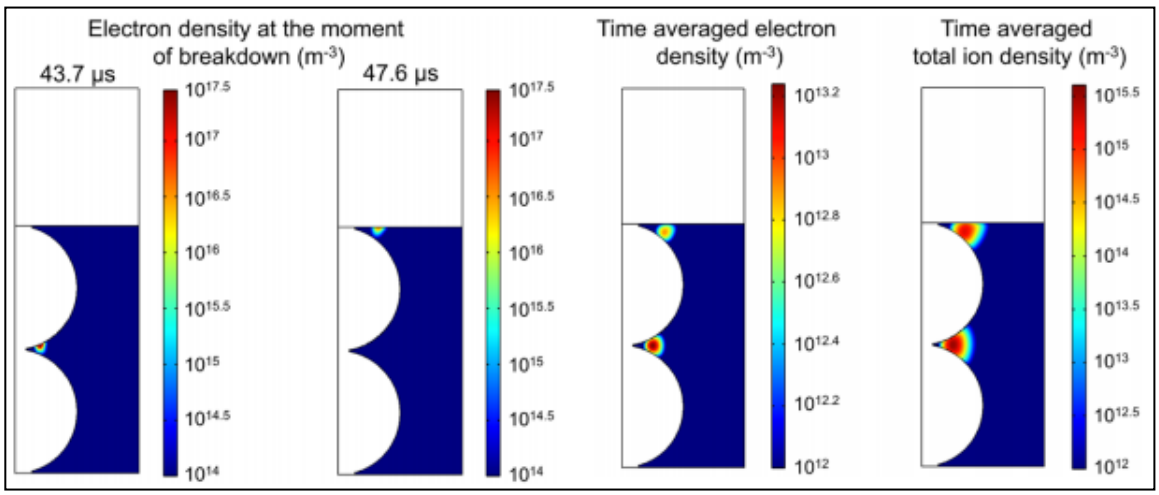

Figure 2-9: Electron density at the moment of breakdown, time averaged electron density, and time averaged total ion density computations from the COMSOL multiphysics 2d modeling effort from Van Laer and Bogaerts.

In regards to the packing fraction study carried out by this group, it was found that a higher packing fraction had a higher localized electric field enhancement with the smaller beads as to be expected. The localized electric fields resulted in higher electron densities throughout the media but were also dependent upon the applied voltage and dielectric constant value. Typical results are shown in Figure 2-10 for a series of dielectric beads.

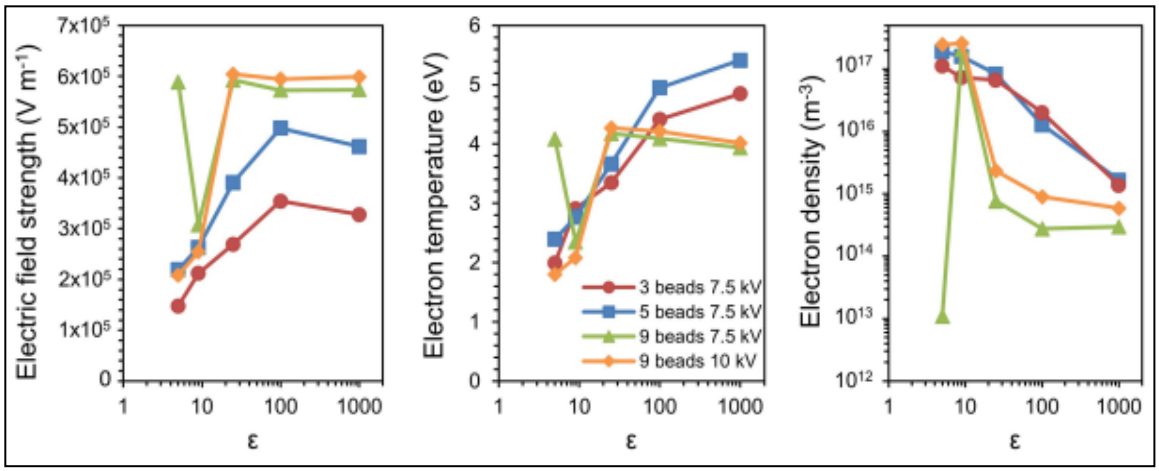

Figure 2-10: Plots from Van Laer and Bogaerts that show the influence of dielectric constant on the space- and time-averaged electric field strength, electron temperature, and electron density.

Their work is introduced here to the reader for work that agrees with the experimental findings in this report. The computations performed were independent of any collaboration with the experimental work presented here but are an additional source that provides insight into the findings reported.

2.4 The synergy enigma of plasma-catalytic systems

Because PBRs feature dielectric aggregate in contact with plasma, such systems have potential applications in catalysis. Plasma catalysis features the interaction of plasma with catalytic particles (such as platinum, gold, or silver) embedded in the dielectric aggregate to enhance reactivity in the input feed or process gas. Under such conditions enhanced reactivity is observed. These processes remain poorly understood.[32,33] Chung et al.,[34] performed the dry reforming of methane within such a reactor using a hybrid plasma catalytic system. In this case, a photocatalyst was used resulting in a 42% enhancement from 13.0 to 18.5 mol per kilowatt-hour in syngas generation. Apparently the plasma enhanced the lifetime of the surface structure of the photocatalyst. This means that the plasma was able to decrease particle build-up on the reactor that would otherwise cover the catalytic particles in a non-plasma system.

Non-thermal plasma catalysts have also been investigated for the reduction of NO_x and diesel particulates in engines as well.[35,36,37] Catalytic abatement of volatile organic compounds has also been investigated with toluene as the model compound. Subrahmanyam et al showed that the implementation of a Mn and Co on the electrode gave rise to CO_2 selectivity being 80% and 100% conversion of the toluene input to a CO_2 output.[38] Indeed, in this work, it was found that the energy cost was only 235 J/l for complete conversion of 100 ppm of toluene using plasma in comparison to the ~1000 J/l required using conventional thermal destruction methods. This of course assumes the reactors can actually scaled for industrial process levels.

Kim and Ogata investigated non-thermal plasma catalyzed decomposition of volatile organic compounds or VOCs.[39] In this work, gas chromatography (GC) and Fourier Transform Infrared analysis (FTIR) was used to assess the decomposition of benzene and toluene. Zeolite pellets impregnated with silver nanoparticles were utilized in this work. It was found that metal nanoparticles enhanced the carbon balance and CO_2 selectivity. The observed reactivity and associated selectivity was dependent upon the type of metal nanoparticles chosen suggesting that further optimization was possible.

2.5 Application of PBRs and Micro-plasmas To Environmental Problems

The work discussed in this thesis provides insight into the discharge propagation and formation mechanisms, species produced via inorganic and organic discharges, as well as applications to agriculture. DBDs have the potential to greatly impact the way chemicals are synthesized as well as remediated post-use. These applications are now being investigated in diverse areas such as plasma-aided combustion, plasma medicine, and plasma agriculture.[40,41] DBDs and PBRs are a potentially scalable technology and

the goal of this thesis is to contribute to advancing our knowledge base on this discharge type so that these applications are one day realized.

This work hopes to address a number of questions regarding PBR operation. For example, how do these plasmas form and propagate in various media as a function of voltage, pressure, intrinsic material properties, and frequency? How do catalytic components effect these mechanisms? Are these characteristics able to be manipulated for reaction selectivity and application efficiency? What happens to organic material in contact with plasma in PBRs? Does plasmas damage the surface of aggregate material?

Chapter III

2-Dimensional Cell: Classification of Discharge Formation and Propagation

3.1 Experimental Approach

Plasma formation propagation in a 2-dimensional array of dielectric elements was studied using an iCCD fast-camera imaging and a computational model. A schematic of the experimental apparatus is shown in Figure 3-1. Dielectric aggregate is sealed between two quartz plates 6.35 mm in thickness. One plate contains a recessed area to accommodate the dielectric disks and the electrodes. The plates make contact with the quartz, which prevents plasma propagating over the dielectric plates, thus constraining the plasma to through the dielectric media.

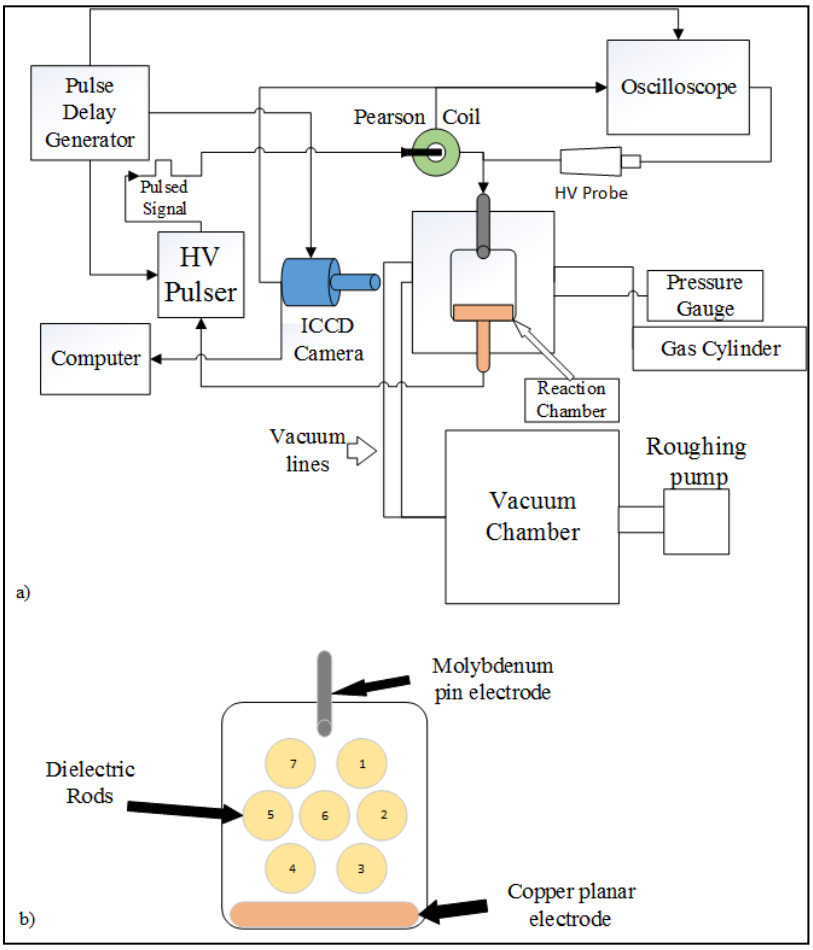

Figure 3-1: Experimental setup for the time-resolved microdischarge analysis. (a) Schematic of apparatus. (b) Overhead view of reaction chamber with media.

An array of seven dielectric disks consisting of either quartz (5 mm in diameter and 3 mm thick) or zirconia (6.2 mm in diameter and 3.5 mm thick) was studied in this investigation. The dielectric media, which was arranged in a hexagonal array with a span of 20 mm, was located between two metal electrodes configured in a pin-to-plane configuration as can be seen in Figure 3-2.

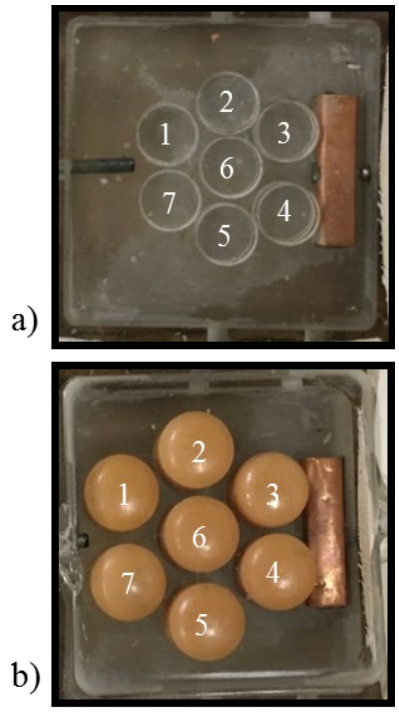

Figure 3-2: Hexagonal pattern of dielectric disks in a pin-to-planar electrode setup (a) quartz (5 mm diameter), (b) zirconia (6.1 mm in diameter).

The hexagonal configuration mimics the highest packing fraction layout of spherical beads in a 3-D PBR. The pin electrode was a 2 mm diameter molybdenum rod and planar electrode was a 25 mm wide x 4 mm thick copper plate. The quartz disks had a dielectric constant of ε_r=3.8. For this study, the dielectric constant of the zirconia disks were determined via a resonant post technique described elsewhere.[42,43] The measured dielectric constant for the zirconia disks was ε_r=26.6±0.24 at 6.2 GHz. For the quartz disk arrangement, the average disk center to center spacing was 6 mm with a minimum gap of ≈1 mm. For the zirconia disks, the center to center spacing was 7.2 mm also with a minimum separation of ≈1 mm. The geometrical placement of the dielectric disks determines the initial spatial distribution of the electric field in the gaps between the disks.[44,45,46] For example, the vacuum electric field distribution is shown in Figure 3-3 for the 2D-PBR with quartz and zirconia disks for an applied voltage of 20 kV. The electric field was using ANSYS: Maxwell, a commercially available electrostatic field

solver. Electric field enhancements naturally occur at the poles of the disks due to the presence of induced surface charge associated with polarization of the dielectric disks.

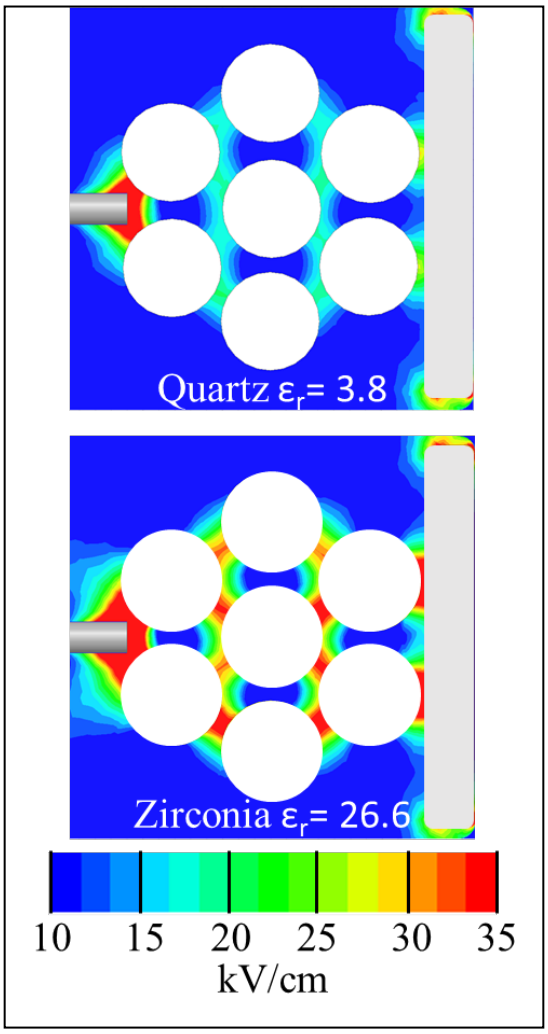

Figure 3-3: Simulated vacuum electric field within *ANSYS: Maxwell* for applied voltage of 20 kV in the 2D-PBR for (top) quartz ($\varepsilon/\varepsilon_0$=3.8) and (bottom) zirconia ($\varepsilon/\varepsilon_0$=26.6).

The electric field is essentially refracted into regions of reduced dielectric strength—the interstitial spaces. Although additional field enhancement can also occur due to surface roughness, the disks in this study were relatively smooth, with a surface roughness on the order of few tens of microns as determined by manufacturing specifications.

The pin electrode was biased to high voltage using an isolated output, high voltage pulser [Eagle Harbor Technologies Nanosecond Pulser -120 (EHT NSP-120)] as

shown in Figure 3-1(a). The voltage pulse used for operation at 1 atm had a peak amplitude of 20 kV DC and a pulse-width of 120 ns. For sub-atmospheric pressure tests (200 Torr to 1 Torr), 12 kV DC, 120 ns wide pulses were used. A Tektronix P6015A High voltage probe was used to acquire voltage measurements. A current transformer (Pearson Model 6585) was used with a Tektronix MDO 3024 Mixed Domain Oscilloscope to measure current. The discharge was imaged using an Andor iStar 334 ICCD camera fitted with a microscope lens of 2.5× magnification that captured images with a 5 ns integration time.

The discharges were single shot with each image corresponding to a single applied voltage pulse. Using a delay generator, one can vary the position of the ICCD camera's trigger pulse relative to the time of application of the high voltage pulse thereby facilitating time resolved imagery, albeit on separate pulses. The initial time, t = 0, is the instant at which the power supply delivers voltage to the electrodes, which occurs ≈335 ns after the power supply is triggered as there is an inherent time delay in the power supply and lines. Images were acquired on successive discharge pulses with additional delay of 5 ns to generate a time sequence of discharge formation. This process proceeded until emission from the cell was no longer distinguishable from the background. The 2.5× magnification lens provided a resolution of 5.6 microns/pixel. A macro lens providing a resolution of 127 microns/pixel was used to study discharge propagation over the entirety of the dielectric array. The camera was enclosed in a Faraday cage to minimize electromagnetic interference (EMI) generated by the power supply and discharge.

3.2 Modeling within ANSYS:Maxwell

In order to gain a greater understanding of the electric field enhancement due to the dielectrics, a commercially available software ANSYS:Maxwell was implemented. The software is an electromagnetics solver that in this case the expected electric field as a function of position. This field is determined by the geometry of the system, applied voltages, and the materials chosen within the model. For our investigations, the 2-dimensional cell was modeled as well as a 3-dimensional packed bed reactor with varying dielectric constant and packing fraction.

3.2.1 The 2-dimensional cell

The expected electric field enhancement effects between the quartz and zirconia dielectric disks as a function of the dielectric constant was determined with an identical setup within the *ANSYS:Maxwell* software. The exact dimensions of the 2d cell were constructed with a 20 kV potential applied to the system, identical to the atmospheric pressure cases. Although the quartz and zirconia disks are slightly different in diameter, simulations were performed utilizing the dielectric constant values of each material at each of their respective sizes as well as identical sizing. Figure 3-4 are the results of the simulations involving the different dielectric constants at the differing sizes. One can easily see that at each size, when directly comparing the quartz electric field enhancement to the zirconia electric field enhancement, that the higher dielectric constant value of 26.6 for the zirconia significantly improves the localized field. When examining the simulated electric field strength map of Figure 3-4, the 'red' coloring represents the electric field strength that is equal to or higher than the breakdown condition in air of 4×10^4 [V/cm]. The zirconia dielectric simulations in Figure 3-4 (a) held maximum field strength of greater than 7 kV/cm near the electrodes at the larger size. The quartz localized field

enhancement had only reached a peak value of near 4kV/cm at the pin electrode but only 2.6 kV/cm at the planar for the larger size as shown in Figure 3-4 (b).

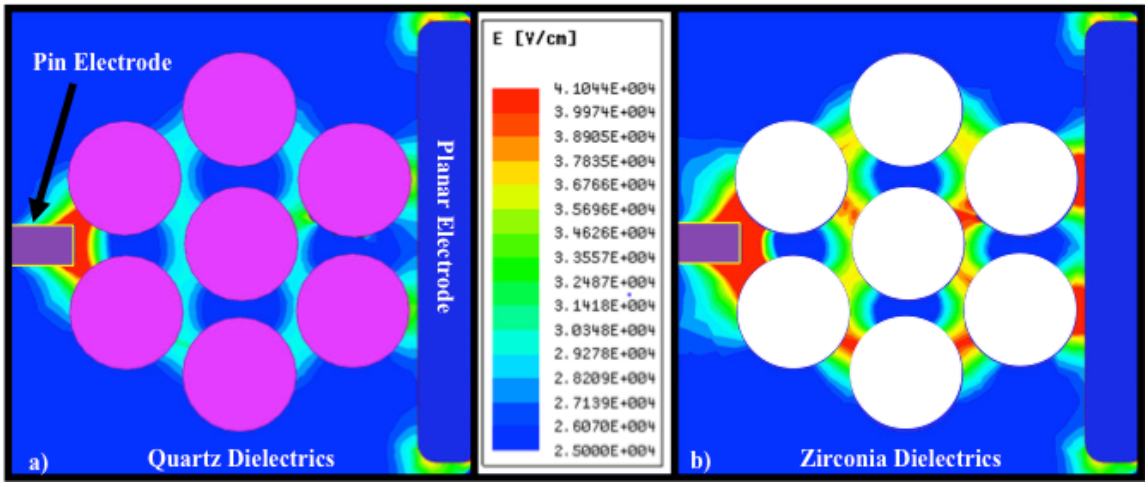

Figure 3-4: ANSYS:Maxwell simulations of the 2d cell geometry with quartz and zirconia being modeled as a changing dielectric constant value. The results are with identical sized of the disks although the experiment holds slightly differing sizes. The simulation utilized a 20 kV potential.

Two additional cases were also simulated with titanium dioxide ($\varepsilon/\varepsilon_0 = 80$) and barium titanate ($\varepsilon/\varepsilon_0 = 1000$) with $\varepsilon/\varepsilon_0$ being set as this value as the barium titanate material dielectric constant value may vary greatly depending on purity and manufacturing processes. The case with the titanium dioxide continued to increase the localized field enhancement with 4 kV/cm being satisfied throughout the aggregate at each interstitial location and had a maximum of 8 kV/cm near the electrodes. The final case involving barium titanate had shown further increase with more volume satisfying the 4 kV/cm breakdown condition. The maximum localized field enhancement with the barium titanate was found to be only slightly above that of the titanium dioxide with a value approximately being 8.5 kV/cm. These results when comparing the higher dielectric constant values (80 and 1000) suggests that there is a saturation limit to the localized field enhancement effects which is most likely geometry and material dependent. The increase in localized field with the higher dielectrics more easily promote plasma breakdown in these interstitial regions as well as the electrodes. Thus, it

is not unreasonable that the zirconia dielectric disks allow FM formation within the interstitial spaces at a lower voltage value as well as provide more optically intense emissions than the images involving quartz as the dielectric.

The simulation results and the experimental findings of the 2d cell provide insight into the manipulation of plasma formation and propagation using dielectric materials. Although the system is only 2d here, it allowed for direct optical imaging without the interference of overlaying media that would increase the difficulty of image analysis. Results from the *ANSYS:Maxwell* simulation provided insight to the electric field enhancement effects due to the dielectric media. Future interesting work may involve a greater range of dielectric constant values in order to try and generate a 'guided plasma' through the media. For instance, two planar electrodes separated by some distance that has been filled with a low value dielectric material. Then a strong dielectric material "path" may be placed throughout the aggregate media in order to promote a higher localized field enhancement and therefore "guide" the plasma on a preferred path throughout the discharge region.

3.2.2 The 3-dimensional packed bed reactor

The first proof-of-concept model that was implemented for the 3d PBR is that of a dielectric barrier discharge reactor without any dielectric aggregate medium. The first simulation was with a 3.175 mm rod electrode that went the length of 25.4 mm diameter reactor. A 10 kV potential was applied to the center rod with the grounded electrode being placed on the wall of the reactor. The first case with an empty reactor had shown an electric field maximum near 2.1 x 10^4 [V/cm]. This value does not meet the electric field breakdown requirement of 4 x 10^4 [V/cm] in atmospheric air conditions. The second case implemented 6.35 mm silica glass sphere with a dielectric constant of 3.78,

provided by the Maxwell software, placed between the central rod electrode and the outer electrode. Figure 3-5 is a side-by-side comparison of the solver solution data set with the electric field strength plotted as a function of the color gradient. One can see that with the dielectric spheres implemented, greater electric field strength is seen throughout the volume. Additionally, utilizing the same scale, one can see the vast increase in the volume in which the electric field strength exceeds the breakdown criterion.

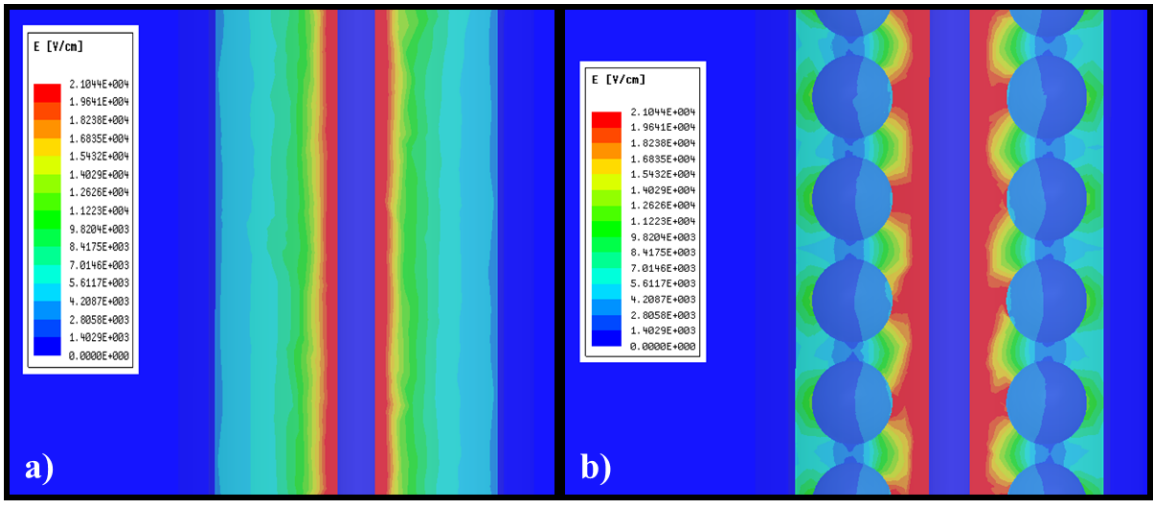

Figure 3-5: ANSYS:Maxwell simulations showing the electric field strength in the reactor without aggregate(a) and with silica glass sphere aggregate(b).

Therefore, a distinct influence of dielectric material and its localized electric field enhancement is shown. Although there is electric field strength 'voids' in-between the dielectric spheres in relation to each other, the much higher field strength near the rod electrode allows for breakdown followed by propagation as seen in the preceding experimental sections. Moving forward with the simulations, another model was generated with the same 3.175 mm rod electrode but with smaller spheres of 1.58 mm and a diameter of 19.9 mm on the reactor. The reason for decreasing the sphere size as well as the diameter of the tube is to represent a high packing fraction with a structured porous media (the repeating silica glass sphere structures). Figure 3-6 shows a completed simulation of this reactor setup with the enhanced electric field at each of the lateral

closest points of contact between the rod electrode and the outer 'mesh' simulated electrode. Comparing the visual E-field strength to the scale, each "red" region between the points of contact has sufficient field strength greater than 4 [kV/cm] and therefore allows for the FM initialization that we see with the macro lens in the 2-dimensional experimental setup.

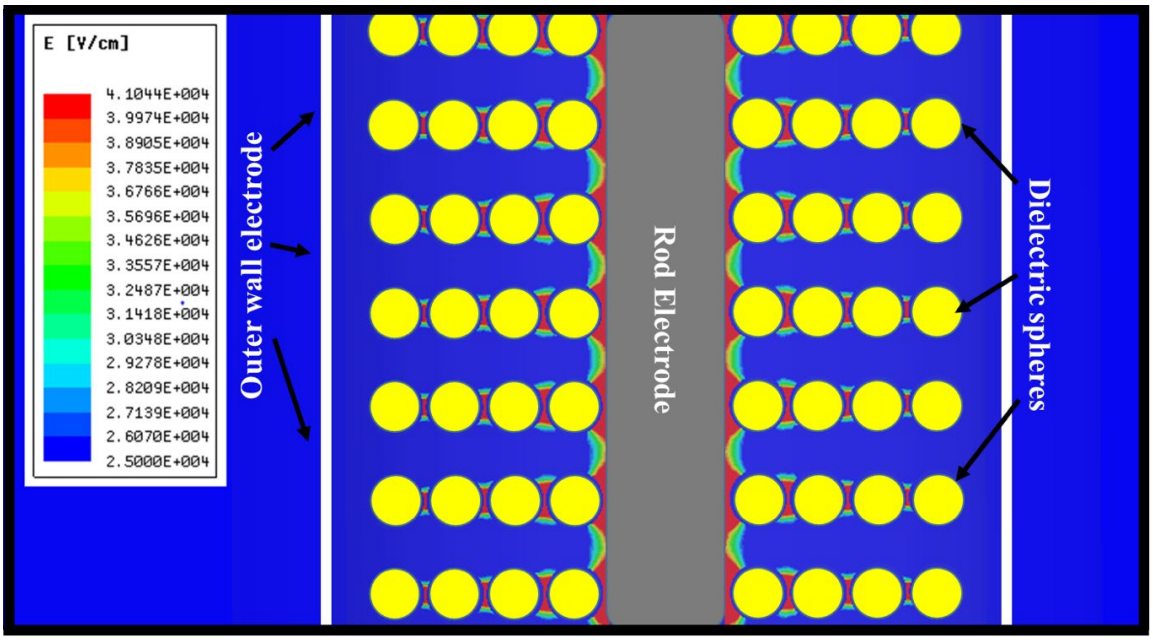

Figure 3-6: ANSYS:Maxwell simulation resulting in the electric field strength effected by inserting a repeating structure of dielectric spheres into the reactor. Any value greater than 4 kV/cm results in satisfaction of the electric field strength required for breakdown.

3.3 Description of the *nonPDPSIM* Model

Modeling was performed using the 2-dimensional plasma multi-fluid simulator *nonPDPSIM*.[47] Poisson's equation is implicitly integrated simultaneously with the continuity equations for charged species and surface charge density over an unstructured mesh using an implicit Newton's method. The electron temperature is calculated by solving the electron energy equation, while the reaction rate coefficients and transport coefficient are derived from local solutions to the Boltzmann's equation for the electron energy distribution. Each computational timestep implements a time-slicing technique. Radiation transport is included by applying a Green's function that describes

the emission and absorption of ionizing radiation from each node to other nodes within the line-of-sight. All ions were assumed to neutralize on surfaces, and secondary electron emission from dielectric surfaces was accounted for with the emission coefficient of γ_{SE}=0.1. All ions incident on the surfaces were assumed to recombine, and were returned to the gas-phase. This results in charging of the surface of dielectric materials, which is then included in the solution of the Poisson's equation. The simulation is operated at 1 atmospheric conditions and lower. For the 1 atm, charged particle transport is represented by drift-diffusion provided by the Sharfetter-Gummel fluxes. Local solutions to the Boltzmann equation are then used to derive the rate and transport coefficients as a function of T_e.

The following series of equations represent the work behind solving the charged particle transport. The electric potential is from Poisson's equation

$$\nabla \cdot (\varepsilon \nabla \Phi) = -(\sum_j q_j N_j + \rho_M)$$

where ε is the permittivity, Φ is the electrical potential, q_j is the elementary charge, N_j is the species number density and ρ_M is the charge on surfaces and materials. In parallel with this, the calculations are also performed for the density of the materials charges and charged particles. The equation for charged particle densities is as follows

$$\frac{\partial_{N_j}}{\partial t} = -\nabla \cdot \vec{\Gamma}_j + S_j + [\sum_m -\nabla \cdot \vec{\Gamma}_m \gamma_m + \sum_k -\nabla \cdot \phi_k \gamma_k]_b$$

where the charge particle flux $\vec{\Gamma}$ is formulated using the method of Scharfetter and Gummel. The source (S_j) in this equation is due to collisions. The sums in brackets apply only to plasma boundary electrons for secondary electron emission by ions. The

first sum is excited species and photon flux ϕ with a secondary emission coefficient γ. The charge density on and in the materials is solved using

$$\frac{\partial \rho_M}{\partial t} = \left[\sum_j q_j \left(-\nabla \cdot \vec{\Gamma}_j\left(1+\gamma_j\right)\right) + \sum_k \phi_k \gamma_k\right] - \nabla \cdot (\sigma(-\nabla\Phi))$$

where sigma is conductivity of solid materials. The sums in brackets apply only to points on the surface of the material. Following the update of the electric potential and charged particle densities, the electron temperature is updated using

$$\frac{\partial}{\partial t}\left(\frac{3}{2} n_e k_B T_e\right) = S_P(T_e) - L_P(T_e) - \nabla \cdot (\frac{5}{2}\Gamma_e k_B T_e - \kappa(T_e) \cdot \nabla T_e)$$

where T_e is the electron temperature, n_e is the electron density, k_B is Boltzmann's constant, κ is the thermal conductivity, S_p is the sources of power, in this case Joule heating from the electric field, and the collisional losses or gains in energy is represented by L_p.

The reaction mechanism is of humid air and includes 33 species and 143 reactions and is a subset of the mechanism first described by Dorai et al.[48] Thirty nine electron-impact reactions were included. These reactions depended on cross-sections based on local electron temperature. Remainder of the mechanism was between heavy particles, and included neutralization, charge exchange, quenching, recombination, as well as formation of N_xO_y species, hydrogen peroxide, ozone, and water-cluster ions. Species incident on surfaces were allowed to deposit charge, de-excite and recombine. The radiation transfer model includes emission of VUV photons from nitrogen singlets [($N_2(b^1\Pi)$ and $N_2(b^1\Sigma)$]. The cross-sections used for radiation transport were 1×10^{-18} cm^2 for non-ionizing absorption by O_2 and N_2, 3×10^{-17} cm^2 for non-ionizing absorption by H_2O, and 1×10^{-19} cm^2 for photo-ionization of O_2.

3.4 Discharge Evolution at Atm. Pressure

The evolution of the discharge in the 2-D PBR after each initiating voltage pulse was imaged in 5 ns increments by adjusting the delay in the trigger pulse to the camera. The minimum exposure time required to capture sufficient light over the background noise with low plasma optical emission intensity was also 5 ns. For a given delay, images were re-acquired 50 times and averaged to account for shot to shot variability in the discharge. The time between physical acquisitions of actual images was 20 s, which is long compared to the characteristic charge relaxation time (ms). If there is not a delay implemented between pulses, charge build-up on the surface of the dielectrics was seen to affect breakdown initiation. Typical current and voltage waveforms for the study are shown in Figure 3-7.

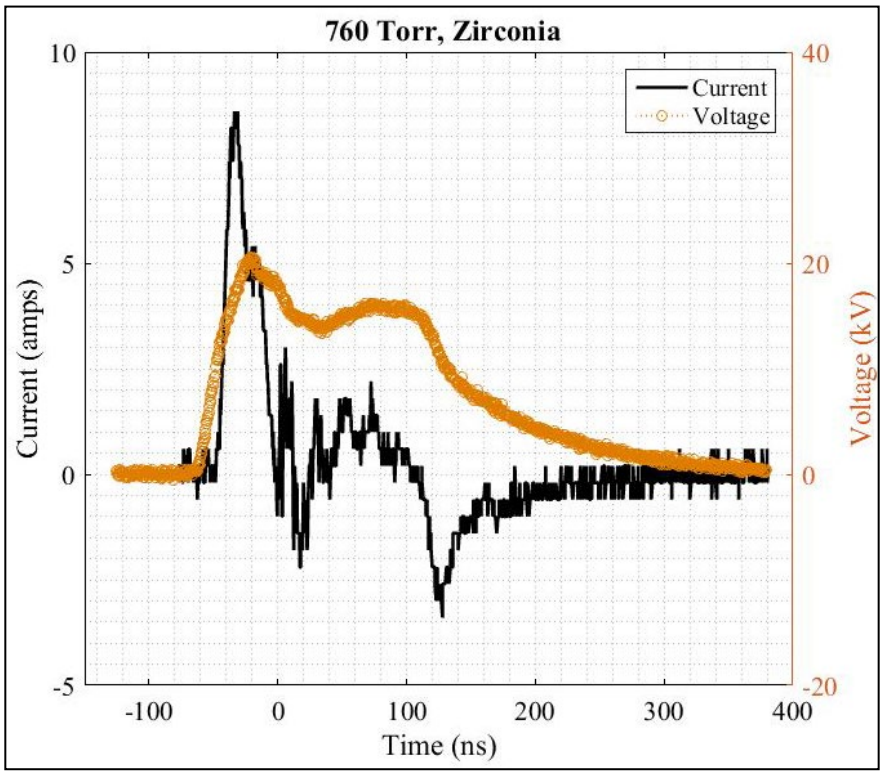

Figure 3-7: Electrical waveforms with zirconia disks for a discharge at 760 Torr. (Black) Current (Orange) Voltage.

Discharge evolution over a 40 ns interval at atmospheric pressure with quartz media is shown in Figure 3-8 for a 20 kV voltage pulse. The voltage pulse was applied

between the anode (pin electrode) on the left-hand side of the image and the planar cathode electrode on the right side. The discharge initiates at the pin anode electrode, where electric field enhancement is high (see Figure 3-3). The discharge tended to occur at regions of locally enhanced electric field, corresponding to regions where the dielectric disks are most closely spaced. At t = 0 (Figure 3-8 (a)), the discharge predominantly forms between the pin electrode and disks 1 and 7. The discharge in this region transitions from a FM to a SIW by 15 ns. The propagation of the surface wave leads to discharge formation around disk 6 by 20 ns. The surface wave formation and subsequent propagation is associated with FM charge deposition. The deposited surface charge generates an electric component parallel to the surface that supports this propagation mode.[49] In this manner the discharge travels through the media reaching disk 4, 25 ns later and finally reaching the cathode electrode by 30 ns. Beyond 30 ns, the discharge re-intensifies in the form a return stroke, which terminates at the pin electrode after 40-45 ns, as indicated by the localized, intense glow there.

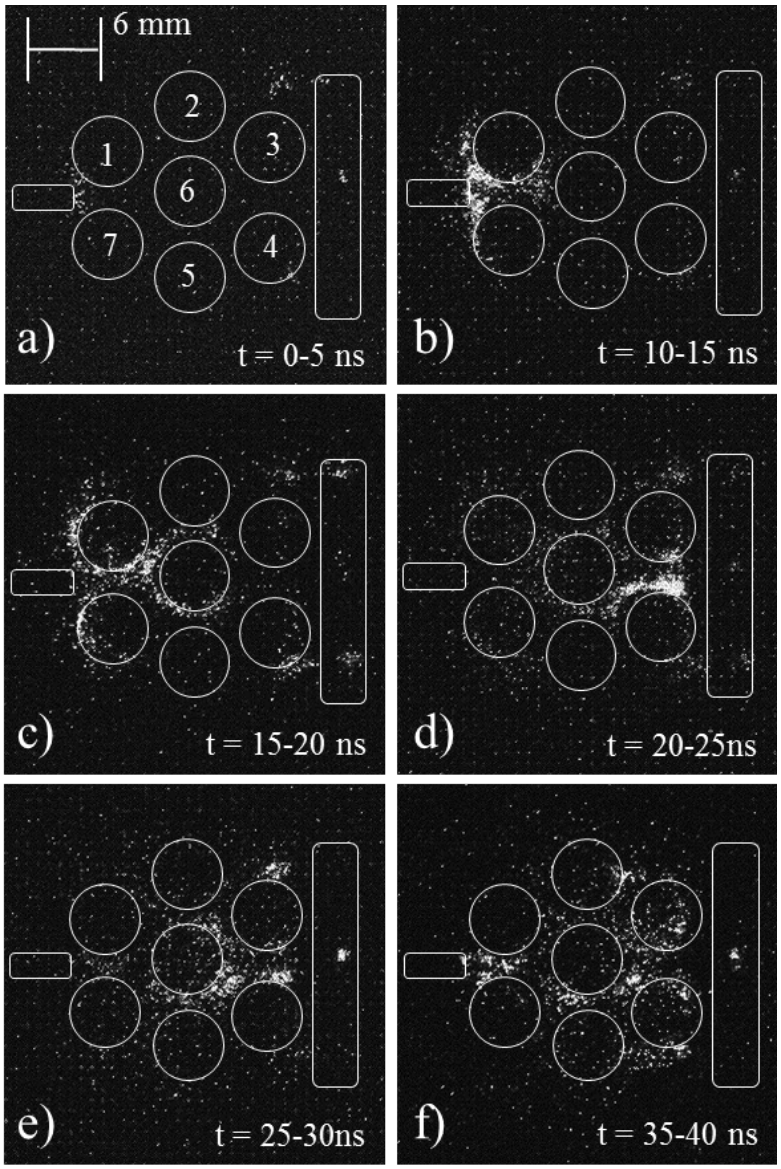

Figure 3-8: Time-resolved imaging of the 2D-PBR discharge through quartz disks at 1 atm integrated over 5 ns. (a) 0-5 ns, (b), 10-15 ns, (c) 15-20 ns, (d), 20-25 ns. (e) 25-30 ns and (f) 35-40 ns.

To gain insight into the propagation mechanism, a small region between disks including portions of disks 3, 4, and 6 was individually imaged with higher resolution. These time resolved images are shown in Figure 3-9. The discharge enters the field of view as a SIW at disk 6 in Figure 3-9 (a). As this SIW propagates around disk 6, it enters into the region of high electric field between disks 4 and 6, leading to the formation of a microdischarge between the two disks (Figure 3-9 (a)). This microdischarge and associated charge deposition leads to the formation of a propagating

SIW along disk 4 (Figure 3-9 (b,c)). Again, as this surface wave enters the region of enhanced electric field between disks 4 and 3 (see Figure 3-3), a FM forms between the disks (Figure 3-9 (c,d)). The surface discharges tend to translate along the surface of the disks in the general direction of the applied electric field.

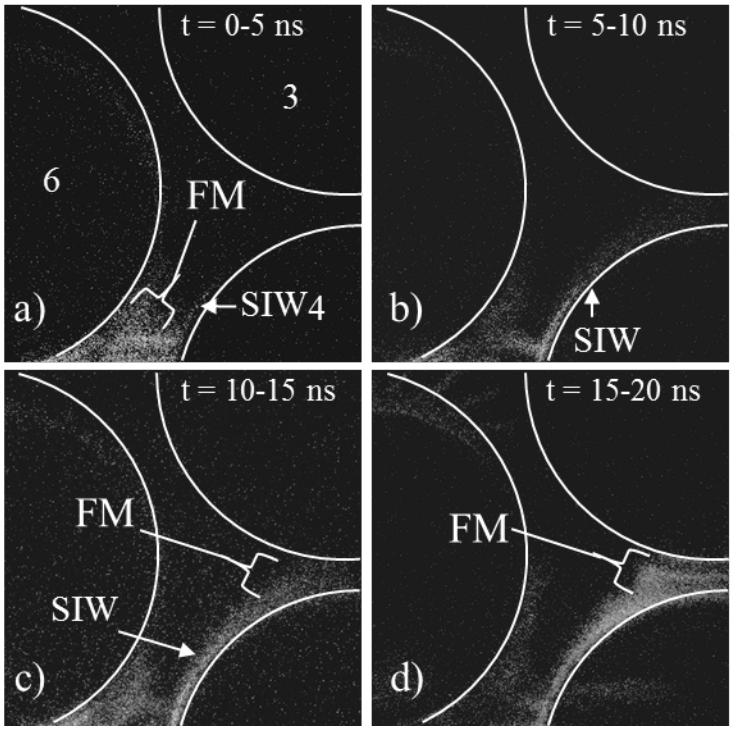

Figure 3-9: Time-resolved microscopic imaging of the 2D-PBR discharge in the vicinity of quartz disks 3, 4 and 6 at 1 atm integrated over 5 ns. (a) 0-5 ns, (b), 5-10 ns, (c) 10-15 ns, and (d), 15-20 ns.

Time resolved imaging of discharges through zirconia disks ($\varepsilon/\varepsilon_0 = 26.6$) was also conducted. Imaging of the entire array is shown in Figure 3-10, and the mode of propagation, at first, appears to be quite different utilizing a macro lens when compared to that through the quartz disks. In quartz, the discharge tended to propagate through the media as an ionization wave where a FM led to formation and propagation of a SIW propagation, which then seeded a FM when the SIW reached the high electric field region in the next gap. With zirconia disks, it was more difficult to discern a clear discharge propagation pattern using the macroscopic lens. Instead with the wide viewpoint, the

discharges appeared to be highly localized, occurring largely in regions of high electric field, which is typically largest between adjacent disks.

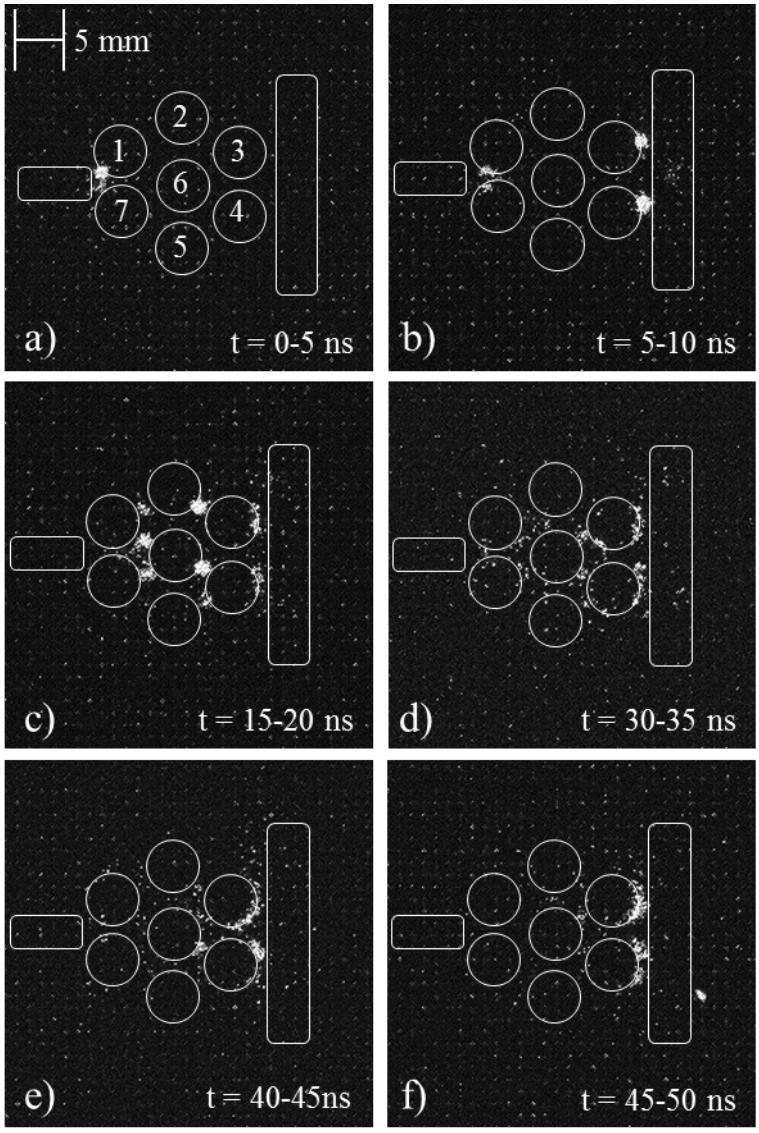

Figure 3-10: Time-resolved imaging of the 2D-PBR discharge through zirconia disks at 1 atm integrated over 5 ns. (a) 0-5 ns, (b), 10-15 ns, (c) 15-20 ns, (d), 30-35 ns. (e) 40-45 ns and (f) 45-50 ns.

At early times in the zirconia array, a localized discharge occurs between the pin electrode and disks 1 and 7 (0-5 ns, Figure 3-10 (a)), followed by localized discharges near the ground electrodes (5-10 ns, Figure 3-10 (b,c)). These discharges are intense, and concentrated at the poles of the disks where the electric field is the largest. These microdischarges last for 15-20 ns before charging of the dielectrics reduce the electric

field in the gap – akin to a DBD. At later times, FMs appear throughout the media aligned with regions of intense electric field (Figure 3-10 (c-f)). These discharges decay over 10s ns, again likely due to charge deposition on the adjacent surfaces, which locally reduces the electric field. Indeed, by 35 ns, all discharges decay away only to reappear near the cathode around 40 ns (Figure 3-10 (e,f)). The voltage pulse width of the supply during these experiments is 120 ns. Once the plasma was seen to travel through the system at 40 ns, some residual plasma is present throughout the system, which effects the next pulse at high frequencies. The optical emission intensity of this plasma after the passage of 40 ns is very low compared to the FM to SIW propagation.

The volume bounded by the surface of three disks (3, 4 and 6) was imaged with higher resolution, as shown in Figure 3-11. At early times, 0-10 ns shown in Figure 3-11 (a,b), intense localized FM develop in the gaps between adjacent dielectric surfaces. The microdischarges that bridge the gap between dielectrics gives rise to the formation of weak emission attributed to surface discharges on disks 4 and 3 at t ≈ 15-25 ns (Figure 3-11 (c,d)) in the general direction of the applied electric field. Therefore, the propagation modes of the zirconia were similar to that of the quartz with FMs forming SIWs that eventually lead back to FMs to repeat until the electrode is reached. The contrast of the FMs with the SIWs when utilizing the macroscopic lens in Figure 3-10 led to only image capturing of the FMs until the microscopic lens was implemented due to light emission intensity differences.

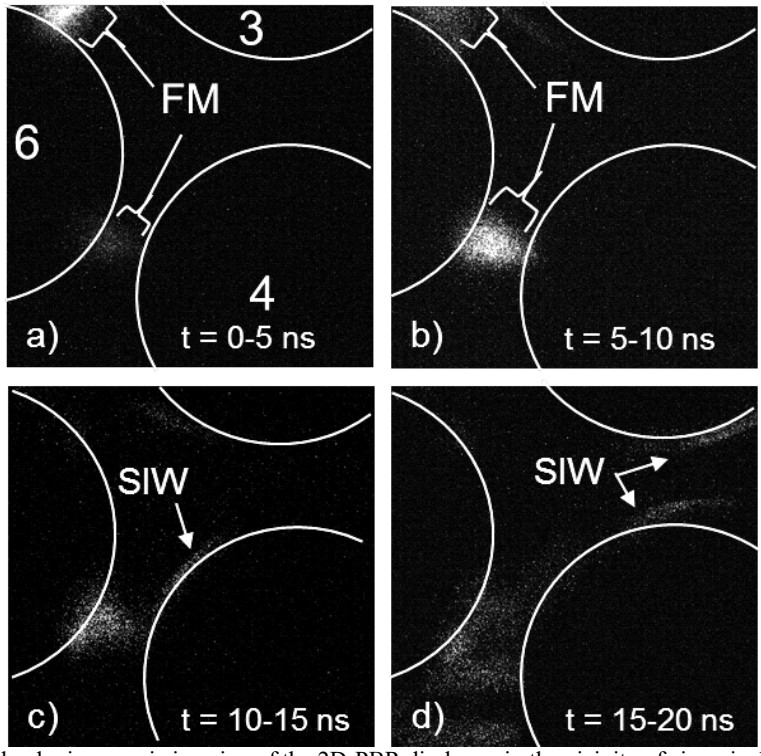

Figure 3-11: Time-resolved microscopic imaging of the 2D-PBR discharge in the vicinity of zirconia disks 3, 4 and 6 at 1 atm integrated over 5 ns. (a) 0-5 ns, (b), 5-10 ns, (c) 10-15 ns, and (d), 15-20 ns.

Based on ICCD light intensity counts associated with the observed discharges (zirconia was nearly an order of magnitude higher than quartz), image contrast, and the magnitude of the current spikes (4 times greater for zirconia), the microdischarges imaged for the higher dielectric-constant material were more intense. Once the discharge develops, charging of the adjacent surfaces will eventually extinguish the microdischarge across the gap due to the reduction in electric field enhancement. It is not clear why the more intense microdischarges do not seed equally intense surface discharges. It is possible that the intense FM collapses the applied electric field locally owing to higher charge deposition, and that this lower electric field is below the threshold to support intense SIWs.

The propagation speeds of the SIWs were calculated using image analysis software to determine the displacement of the SIW over the 5 ns time step. The propagation speed of the SIWs along the surface of the quartz disks was $\approx 3 \times 10^7$ cm/s

and $\approx 4 \times 10^7$ cm/s for the zirconia disks. These values correspond well with those reported in the literature. For example, Petrischev et al. investigated formation of SIWs on a quartz plate using a high voltage, nanosecond pulse and measured propagation speeds of 5×10^7 cm/s.[50] These speeds are commensurate with gas phase streamer propagation speeds. It is not surprising that the zirconia speed is slightly larger, owing to higher current and thus space charge. The streamer speed tends to increase with increasing space charge derived electric field at the streamer head.[49]

A comparison of experimental and modeling results is shown in Figure 3-12. The top row of frames is experimental ICCD images of optical emission between zirconia disks (3, 4 and 6) with an exposure time of 5 ns. The exposures of the images were digitally enhanced to show the features of interest so intensity cannot be directly compared frame-to-frame. The row of frames images produced from the results of the model. The computed results are the densities of the main photo-emissive species in the model ([($N_2(b^1\Pi)$ and $N_2(b^1\Sigma)$]).

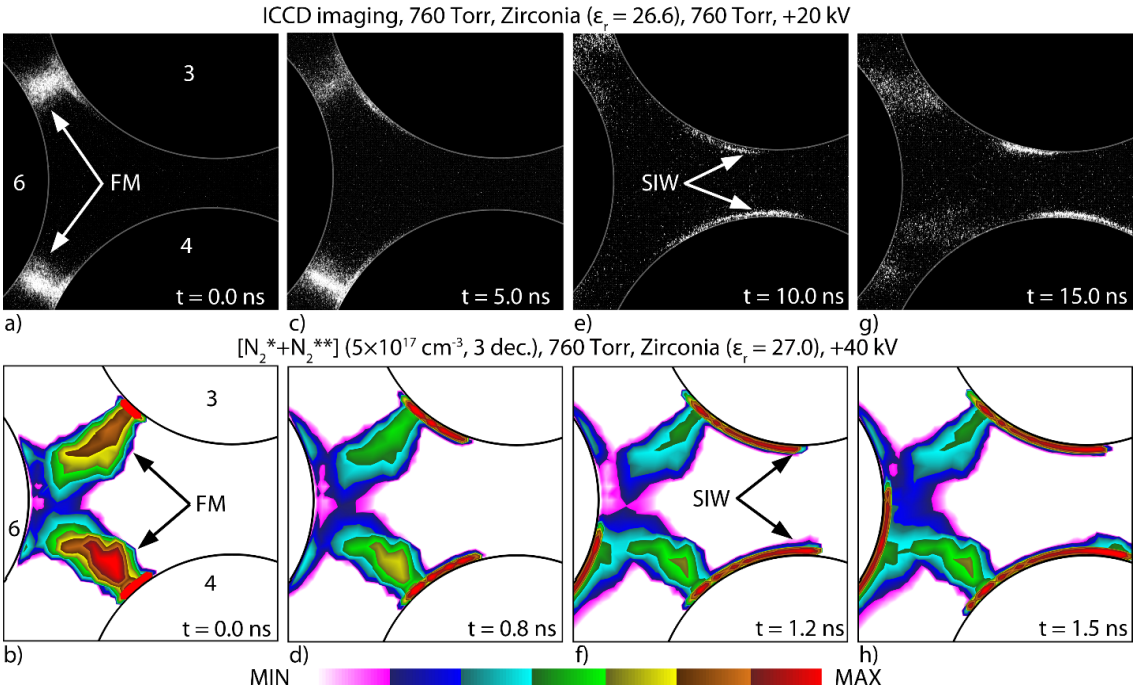

Figure 3-12: Experimental ICCD imaging (top) and densities of light-emitting species from the model (bottom) between disks number 3, 4, and 6 and at various times. The disparity in time between the model and the experiment arises from the different voltages being applied.

The choice of frames was made to show correlating phenomena. Intense filamentary microdischarge structures initially form between disks 6 and 3, and disks 6 and 4, as shown in Figure 3-12 (a,b) (experiment and model). The electrons incident onto disks 3 and 4 charge the surfaces of the dielectrics and SIWs begin forming in Figure 3-12 (c) and (d). As the potential between the disks drops due surface charging, the intensity of the FMs decreases, and the propagating SIWs become the brightest regions in the images, as shown in Figure 3-12 (e) through 12h. The surface ionization waves are cathode-seeking discharges – regardless of the polarity of the applied voltage, as demonstrated in our previous work.[49] This is because electrons impact the dielectric surfaces leave behind a region of positive space charge in the gas-phase. Through a process similar to that of the propagation of positive streamers, the positive SIWs then propagate down the potential gradient.

An example of the *nonPDPSIM* model as a function of changing the intrinsic dielectric value of the aggregate is shown in Figure 3-13 (a-f). In (a), a value of 1 is chosen to represent atmospheric air and then increased to 4 (similar to quartz) and further after that. As the value is increased, the electron density populations at breakdown transition to more localized filamentary micro-discharges and surface ionizations waves. At dielectric constant values greater than 100, the discharge modes within the model shift less and therefore show that the discharge is more sensitive to $\varepsilon/\varepsilon_0$ changes at low values. The peak electron temperature is also seen to increase from ≈ 7 eV to ≈ 11 eV with these modifications to the model. The shift in T_e suggests that kinetic reaction mechanisms may be manipulated with the dielectric aggregate as suggested with the experimental results as well. Further studies involving laser induced fluorescence would provide information for the electron temperatures in the experimental study.

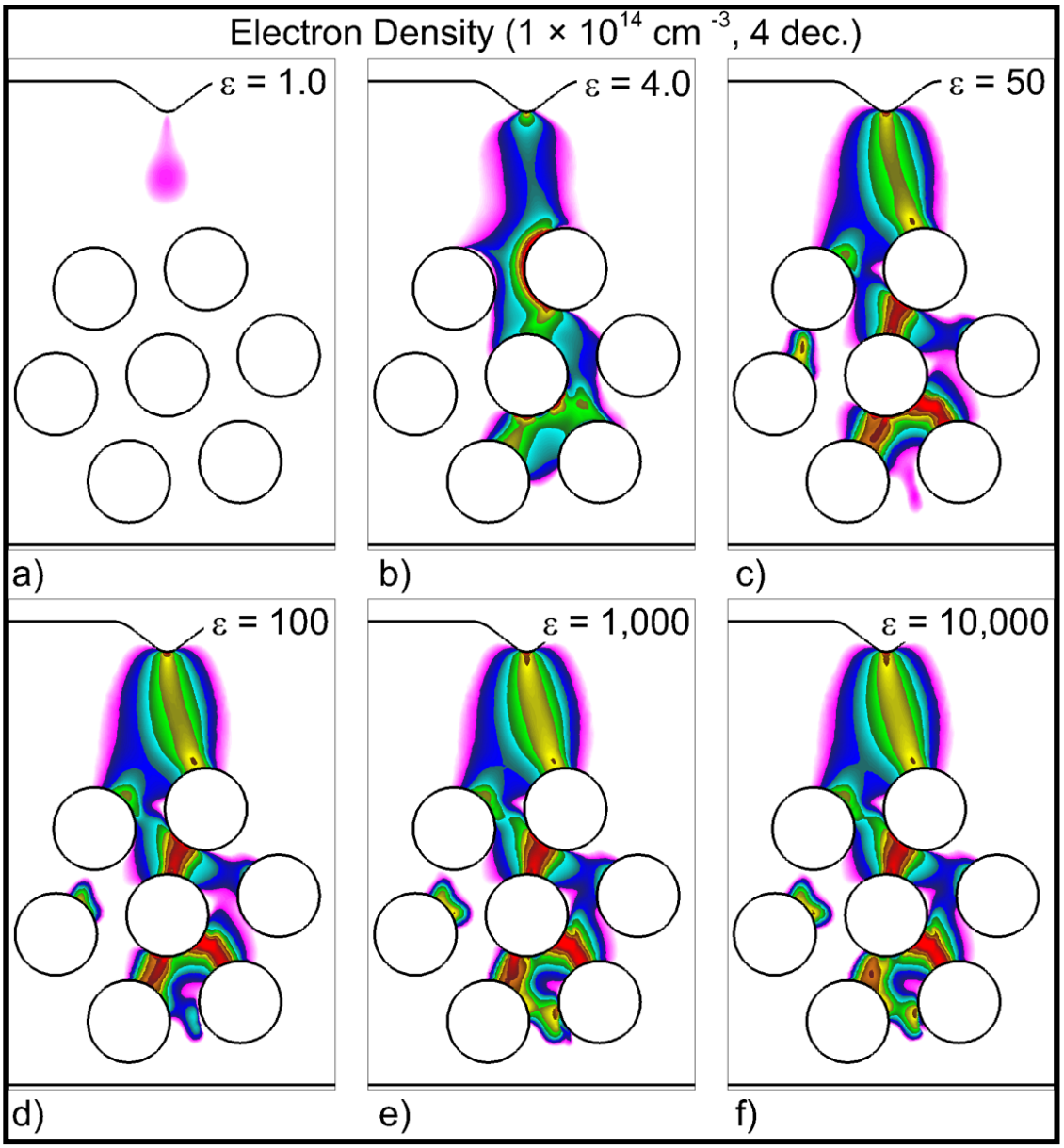

Figure 3-13: Electron density as a function of changing the intrinsic dielectric constant value of the aggregate. The color map is representative of the locations of highest electron density within the 2-d cell.

The experimental discharges discussed were sustained with voltage pulse amplitude of 20 kV. Investigations were also performed for discharges through zirconia disks aggregate for voltage amplitudes of 16, 17, 19, and 20 kV at atmospheric pressure, as shown in Figure 3-14. The trends for discharge formation and propagation were basically the same as a function of voltage over this range, with only the intensity and speed of discharge formation increasing with increasing voltage. The contrast of the

images for 19 kV and 20 kV (Figure 3-14 (a,b)) shows more intense FMs whereas at the lower voltages of 16 kV and 17 kV (Figure 3-14 (c,d)) the plasma appears to be more diffuse.

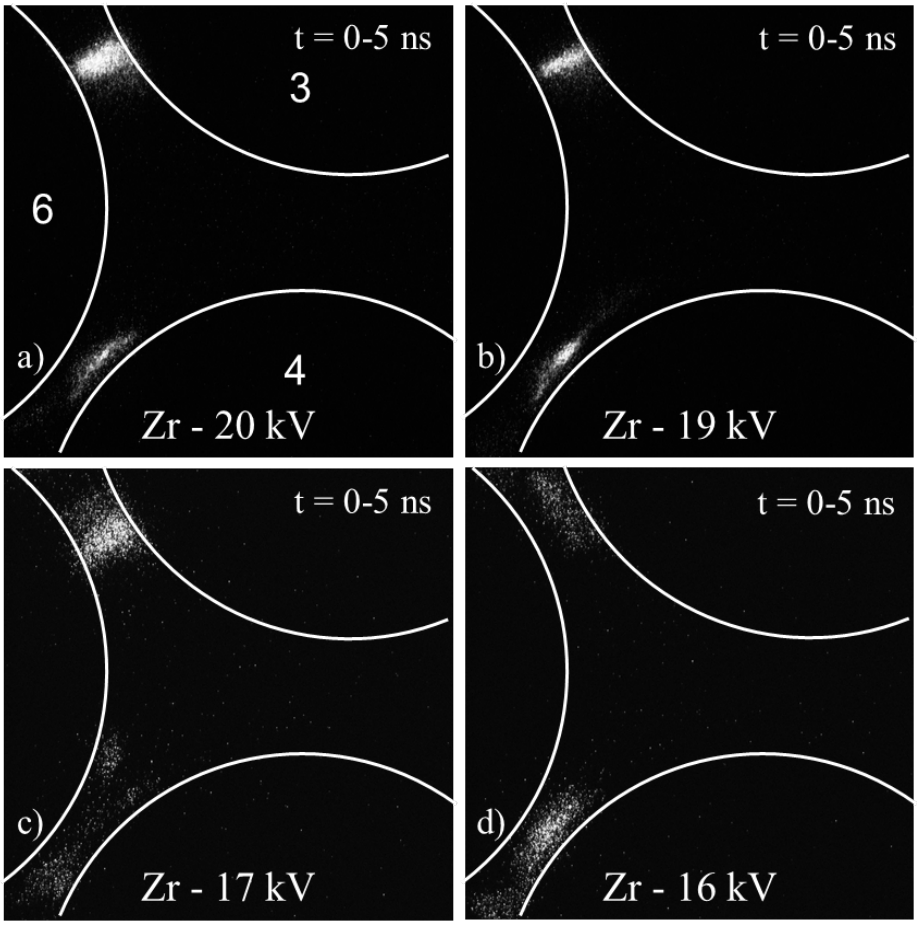

Figure 3-14: Imaging of emission of discharges through zirconia disks (5 ns exposure) at atmospheric pressure. (a) 20 kV, (b) 19 kV, (c) 17 kV and, (d) 16 kV.

3.5 Discharge Evolution as a Function of Pressure in the 2-D PBR

Discharge formation in PBRs at 1 atm is typically highly localized, propagating through the medium essentially as a sequence of ionization waves within gaps (FM) or along surfaces (SIW). The dominance of these structures is in part due to the high pressure for which electron energy transport is dominated by local phenomena. As pressure decreases and electron energy transport becomes less local, we expect systematic differences from discharge propagation at 1 atm. To investigate these trends,

imaging of discharges in the 2-D PBR was performed at reduced pressure. Pressure in the system was reduced via the connected vacuum lines and roughing pump that was previously shown in Figure 3-1 of this chapter. Beyond understanding propagation mechanisms, there may be a practical basis for operating at reduced pressure as well. Although most chemical processing using PBRs is performed at atmospheric pressure to minimize the costs of managing pumping and vacuum, it is not clear that atmospheric pressure is optimum in terms of discharge propagation, filling the volume of the PBR and utilizing all of the catalyst. As the pressure is reduced for a given applied voltage, E/N will increase which would produce higher rates of electron impact dissociation and ionization. Reduced pressure would tend to also increase the volume of the reactor filled by the discharge, which may provide greater selectivity in regards to gas phase reactions.

During sub-atmospheric pressure experiments, the peak voltage was kept constant at 12 kV with a 120 ns pulse width. Experiments were performed at 200, 100, 50 and 10 Torr. A subsequent set of data was also taken at 1 Torr and 500 mTorr but the discharge no longer seemed to be affected by the dielectric material as the entire volume had been filled with plasma. Also, parasitic discharges to the vacuum lines and pressure gauge was seen at such a low pressure and therefore could not be included within the study. Discharge images could not be captured above a few hundred Torr due to the inability to initiate a breakdown through the quartz disks at 12 kV. Changing the applied voltage of the system at the higher pressures would excuse a direct comparison of the images and waveforms acquired.

Images of the time evolution of the discharge with quartz disks in the entire array at 100 and 50 Torr are in Figure 3-15 and Figure 3-16, respectively. In general, when

reducing pressure, local emission intensity decreases. In both lower pressure cases, the discharge appears to translate through the array as a SIW with the thickness of plasma extending well into the gap between disks. Some of this extension into the voids might possibly be due to sheath expansion at the lower pressures.

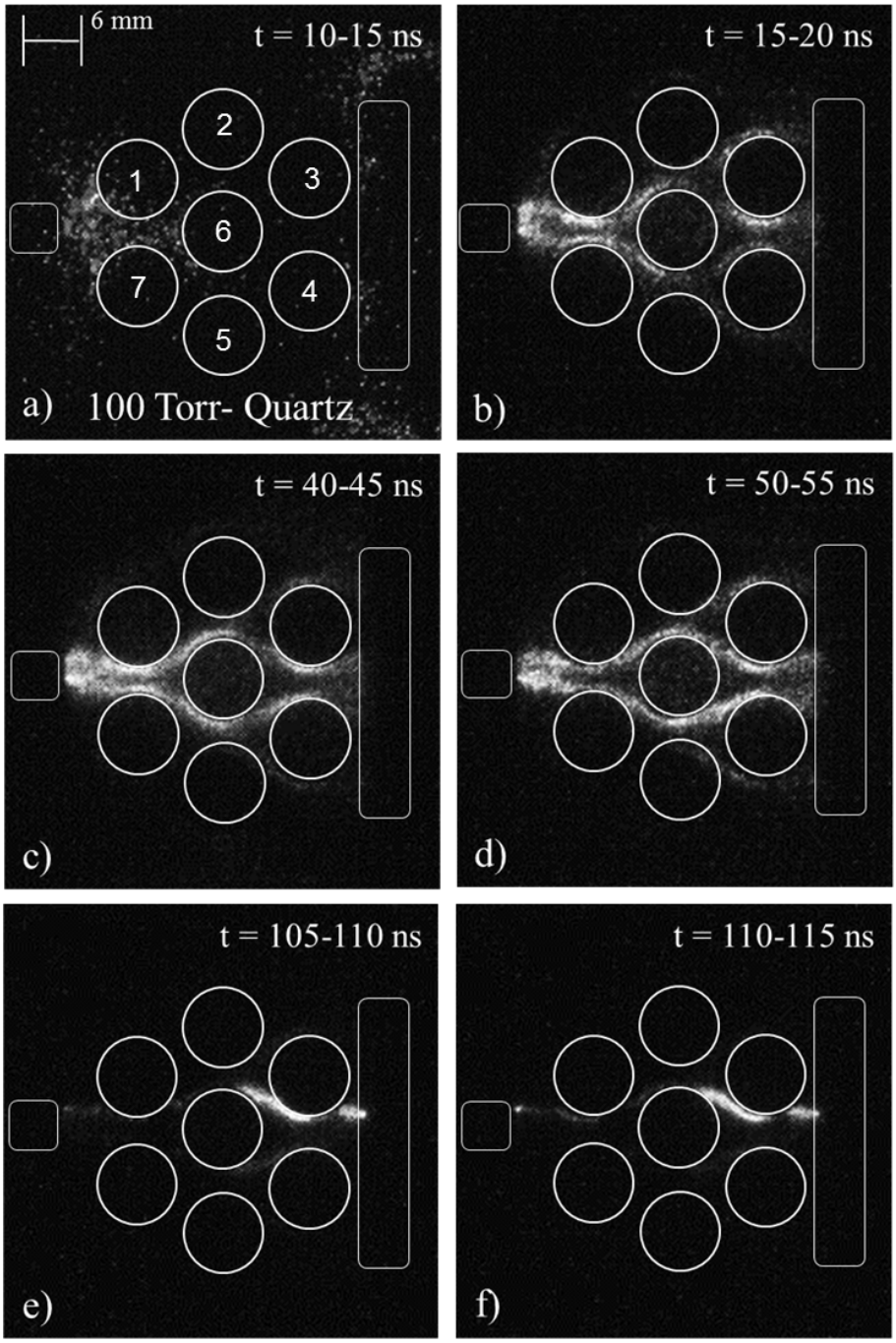

Figure 3-15: Time-resolved imaging of the 2D-PBR discharge through quartz disks at 100 Torr integrated over 5 ns. (a) 10-15 ns, (b), 15-20 ns, (c) 40-45 ns, (d), 50-55 ns. (e) 105-110 ns and (f) 110-115 ns.

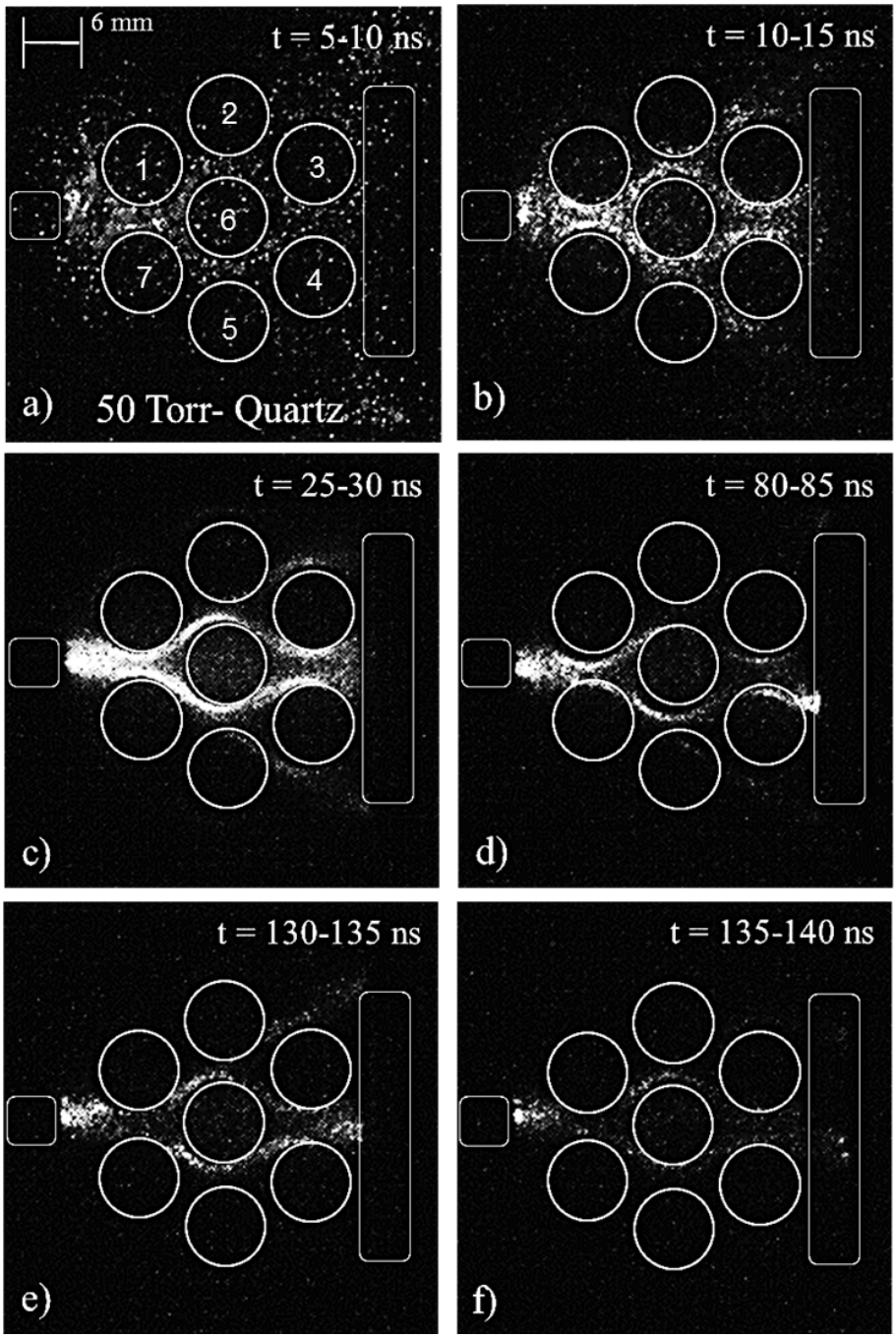

Figure 3-16: Time-resolved imaging of the 2D-PBR discharge through quartz disks at 50 Torr integrated over 5 ns. (a) 5-10 ns, (b), 10-15 ns, (c) 25-30 ns, (d), 80-85 ns. (e) 130-135 ns and (f) 135-140 ns.

The discharge becomes less surface-hugging and bends away from the surface, likely due to the higher mobility of charges being able to more rapidly charge the surface at lower pressures. As the pressure is further reduced to 10 Torr, shown in Figure 3-17, SIWs propagating on adjacent surfaces merge in the volume between the dielectric disks.

In spite of operating at higher values of E/N than the discharges at 1 atm, the images do not indicate that FM form in the gaps between disks where the E/N is largest. This is likely due to the intensity of the SIWs saturating the response of the ICCD.

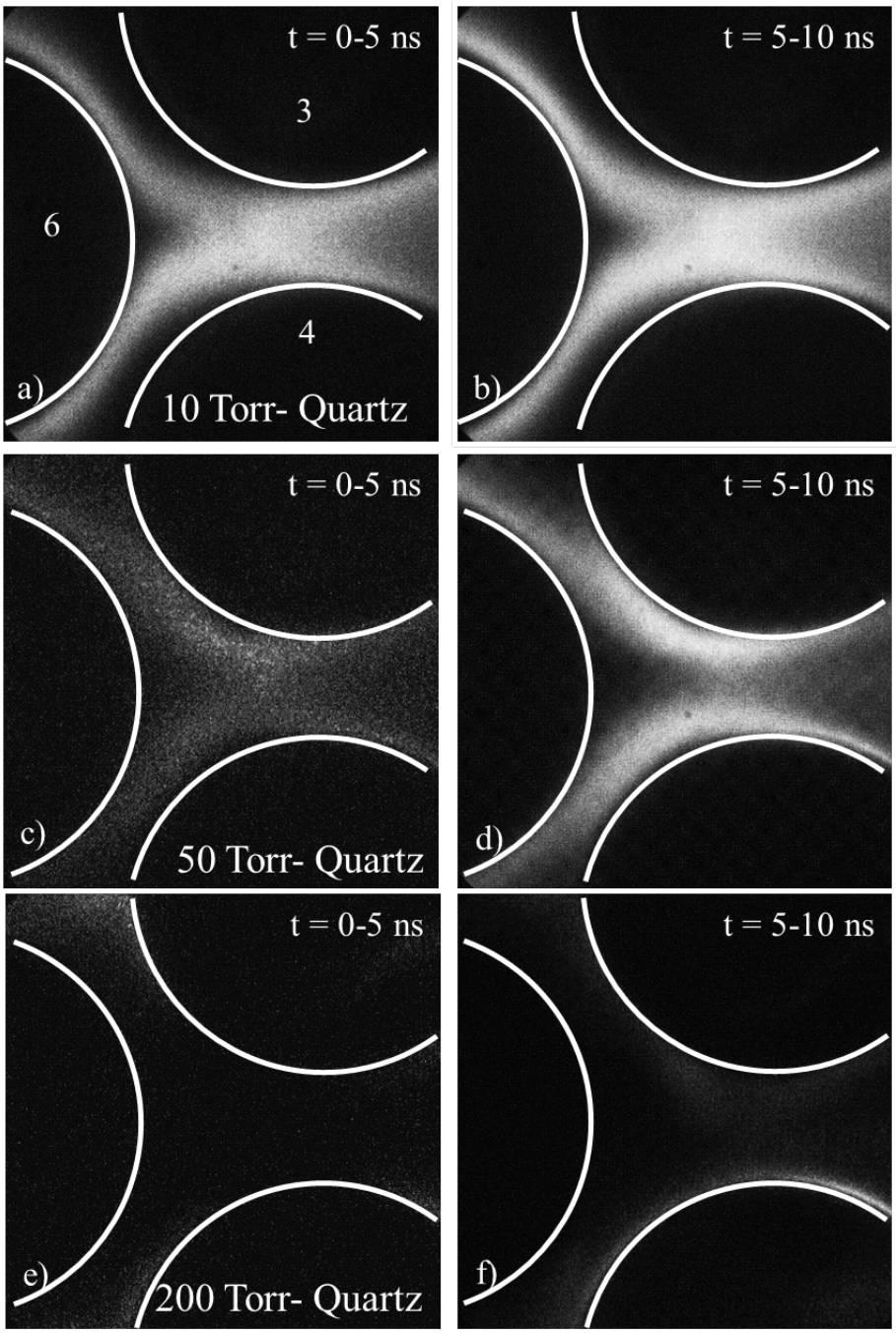

Figure 3-17: Time-resolved imaging of the 2D-PBR discharge through quartz disks for 10, 50, and 200 Torr integrated over 5 ns. (a) 10 Torr, 0-5 ns; (b), 10 Torr, 5-10 ns; (c) 50 Torr, 0-5 ns; (d), 50 Torr, 5-10 ns; (e) 200 Torr, 0-5 ns; (f) 200 Torr, 5-10 ns.

To more closely investigate the formation of FMs at low pressure, a mask was placed over the 2D cell. The mask restricted the ICCD to collecting light from the region between disk 6 and 4 where FMs were expected to form. The resulting images are in Figure 3-18. The right side of the figure has images taken with the mask in place. The left side of the figure has images taken at the same voltage and exposure time but without the mask. Even at a pressure of 50 Torr, FMs form in the high E/N gaps, and transition to an SIW on the adjacent disk. The angle of the FM, however, is not strictly perpendicular to the surfaces at low pressure.

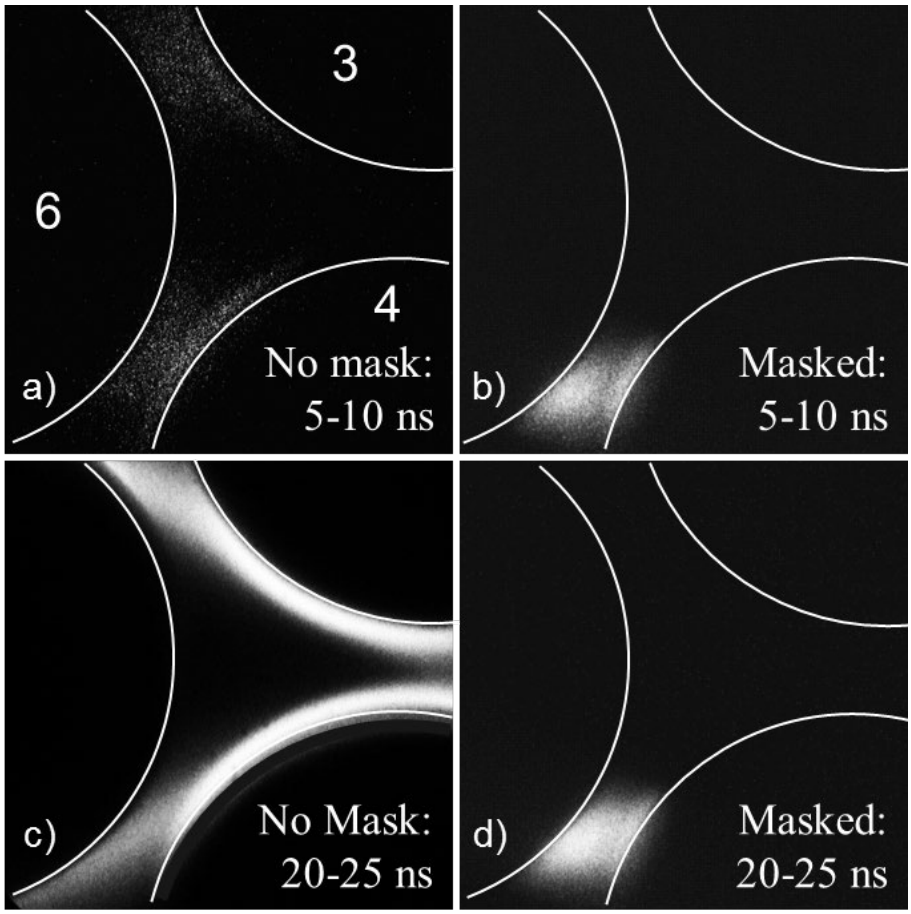

Figure 3-18: Imaging of discharges through zirconia disks at 50 Torr (5 ns exposure) with and without masking. The masking blocked emission from the surface ionization waves. (a) Without mas, 5-10 ns, (b) with mask, 5-10 ns, (c) without mask, 20-25 ns and (d) with mask 20-25 ns.

This is due to the higher E/N throughout the cell at low pressure. For example, at 1 atm the vacuum value of E/N at the center of the void between disks 1, 7 and 6 is 25

Td, which not high enough to self-sustain a discharge in air. (1 Td = 10^{-17} V-cm^2.) At 50 Torr, the E/N in the void is 220 Td, which exceeds the threshold for sustaining a discharge in air. At lower pressure, propagation appears to be more influenced by the applied axial electric field than the electric field enhancement that occurs in the gaps between disks (or due to the polarization of the disks at their poles).

In the gaps between disks 6 and 3, and between 6 and 4, locations where FM occur perpendicular to the surfaces at 1 atm, the discharge propagates parallel to the surfaces at low pressure. In fact, the merging of SIW-like structures from the top and bottom of disk 6 leaves a void where natural electric field enhancement occurs by polarization of the disks. To investigate this region, a mask was applied which largely blocked emission from the higher intensity FMs and SIWs. The resulting images showed diffuse, volumetric plasma emission throughout the *void* at low pressures (50-300 Torr).

The same procedure was performed at 1 atm and little, if any, plasma emission was observed in the void. Values for α (ionization coefficient), and η (attachment coefficient) were computed from the results of *nonPDPSIM* in the void between the disks 3, 4, and 6. As the pressure increases, α decreases from 9.74 cm^{-1} at 50 Torr to 0.21 cm^{-1} at 200 Torr whereas η increases from 0.82 cm^{-1} to 2.53 cm^{-1}. There results indicate that the net rate of ionization, $\alpha - \eta$, transitions from being positive (net ionization) in the void to negative (net attaching) between 100 and 200 Torr. The trends in net ionization predicted by the model correlate well with the experimentally observed change in the mode of propagation. With higher α, plasma propagation occurs in the void, however as the system becomes net attaching, plasma production in the void diminishes.

Time resolved images of discharge development with zirconia disks at 50 Torr are shown in Figure 3-19. Discharge development is similar to that in the quartz array, albeit with higher emission intensity. The discharge slowly develops between 5 and 10 ns, after which the array quickly fills with a highly developed discharge. Here again, a surface wave like discharge propagates through the array with the interstitial spaces being filled with higher density plasma than the seemingly empty voids. The discharge appears to cover the zirconia disks more extensively than the quartz disks.

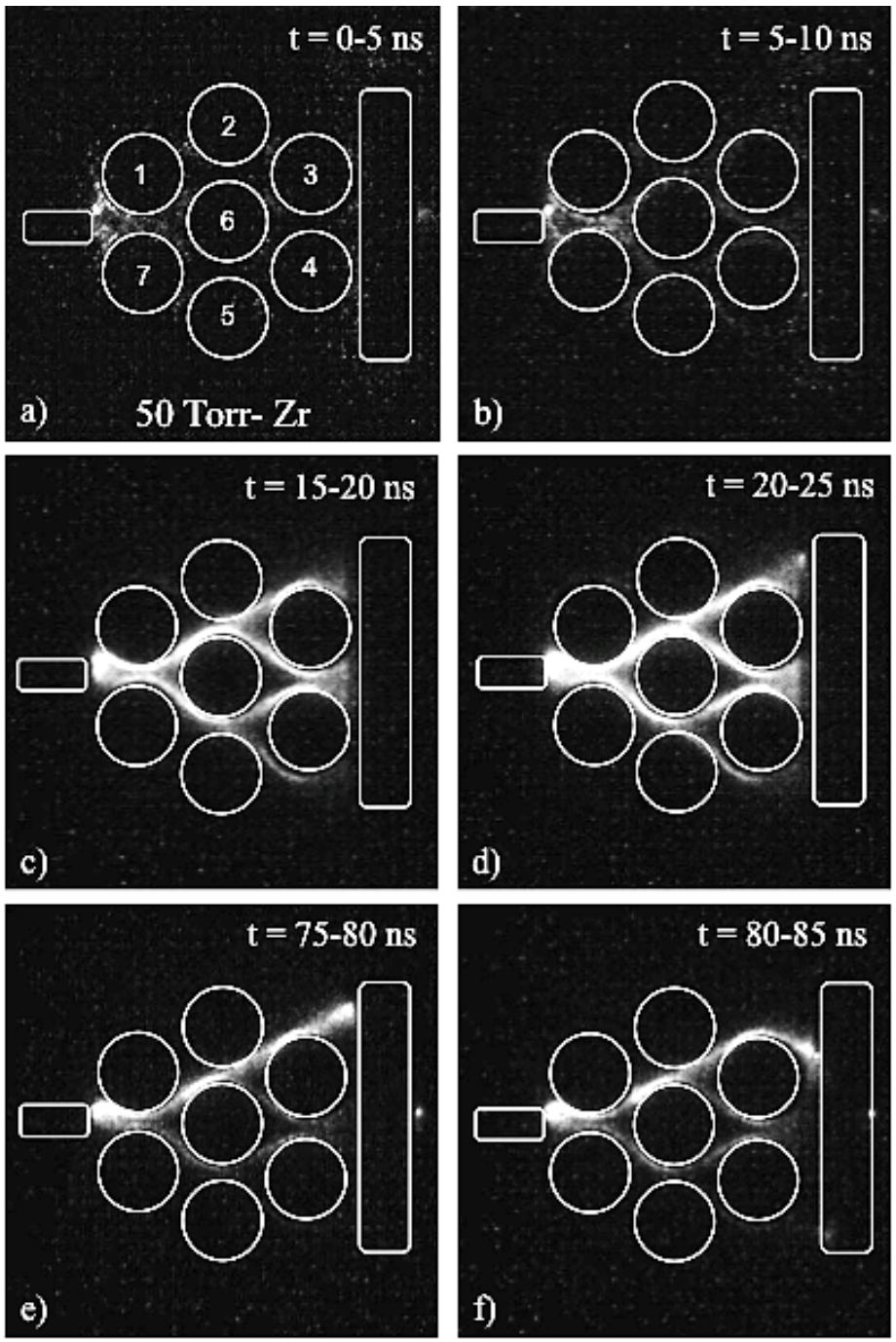

Figure 3-19: Time-resolved imaging of the 2D-PBR discharge through zirconia disks at 50 Torr integrated over 5 ns. (a) 0-5 ns, (b), 5-10 ns, (c) 15-20 ns, (d), 20-25 ns. (e) 75-80 ns and (f) 80-85 ns.

The time resolved images of discharge propagation through zirconia disks in the vicinity of disks 3, 4 and 6 are shown in Figure 3-20 for pressures of 10 Torr through 200 Torr. With the larger permittivity of zirconia, the discharge behavior that occurs at 1

atm is recovered by 200 Torr. At 10 Torr, the discharge is dominated by SIWs. At 200 Torr, FMs are produced in the gaps, followed by the launch of SIWs, as at 1 atm.

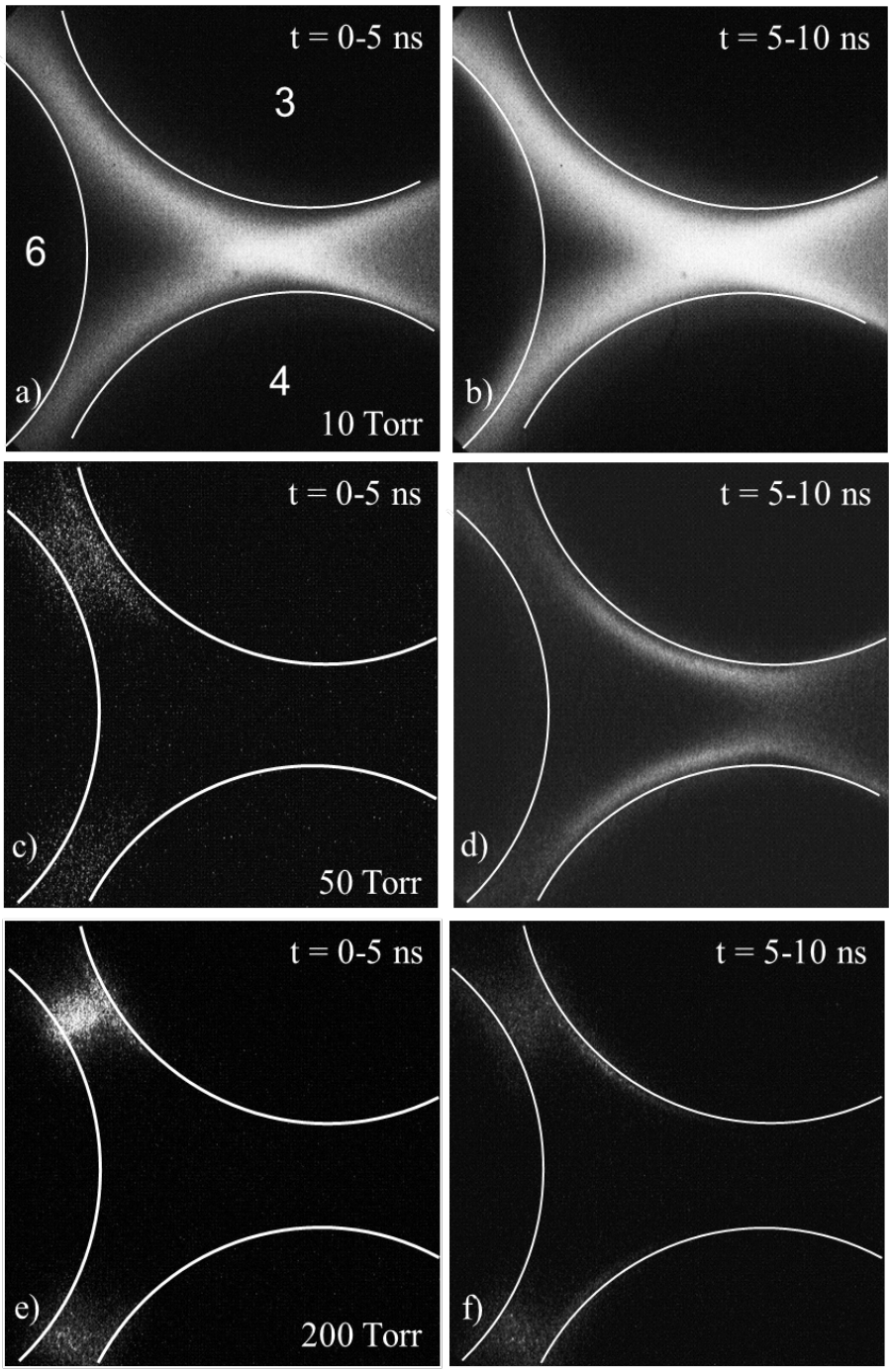

Figure 3-20: Images of the 2D-PBR discharge through zirconia disks for 10, 50, and 200 Torr integrated over 5 ns. (a) 10 Torr, 0-5 ns, (b) 10 Torr, 5-10 ns, (c) 50 Torr, 0-5ns, (d) 50 Torr, 5-10 ns, (e) 200 Torr, 0-5 ns, (f) 200 Torr, 5-10 ns.

The transition between SIW to FM discharges in the zirconia array occurs near 200 Torr. This transition is shown by the images in Figure 3-21 for pressures between

180 and 210 Torr. At 180 Torr, the applied E/N is large enough that the discharge occurs in regions outside the field-intensified gaps. As the pressure increases from 190 Torr to 200 Torr, the E/N outside the gaps decreases below self-sustaining, leaving the gaps having large enough E/N to initiate the discharge in the form of FM.

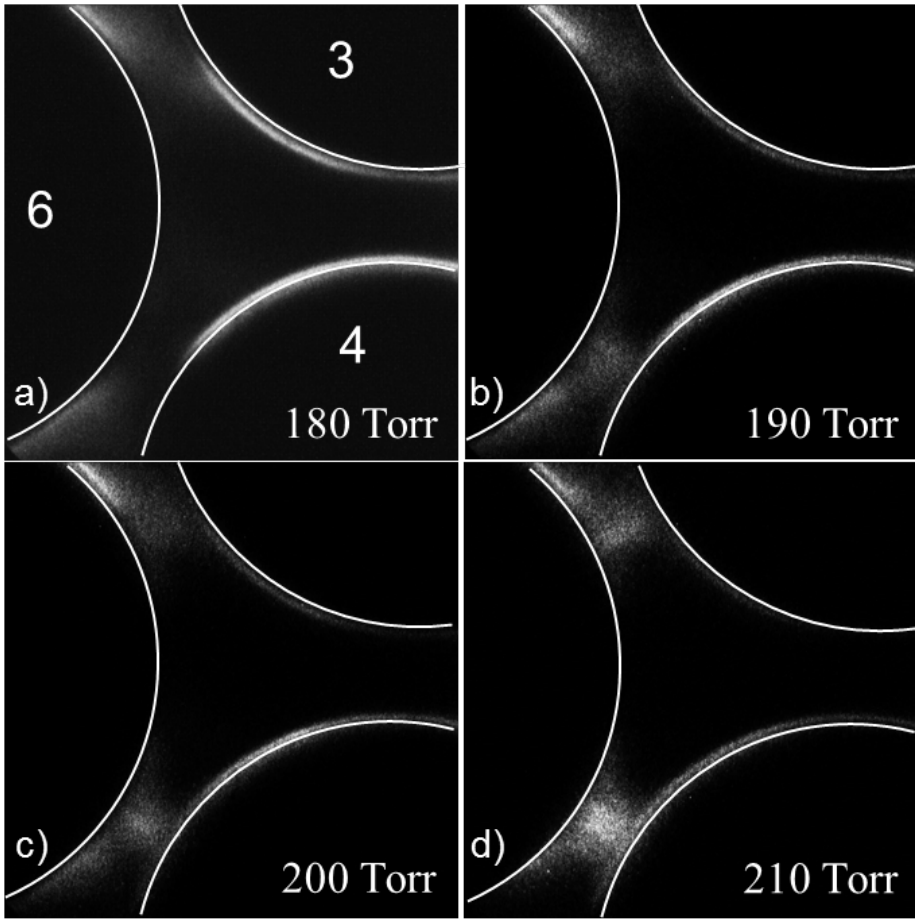

Figure 3-21: Images (10 ns exposure) capturing the transition from SIW, volumetric discharges to micro-discharges with increasing pressure. (a) 180 Torr, (b) 190 Torr, (c) 200 Torr and (d) 210 Torr.

The thickness of the SIW was measured from the ICCD images and is shown in Figure 3-22. The measurement was made from the surface of the disk to the edge of the luminous region and did not consider possible sheath effects that may elevate the luminous region above the disk. The SIW thickness varied inversely with the pressure, suggesting that the thickness is limited by the electron-neutral mean free path. The surface wave thickness varied linearly with mean free path regardless of type of material,

though SIW thickness tended to be greater for the quartz disks. This trend is consistent with the ICCD images being more intense for the zirconia, implying higher plasma density, smaller Debye length and so thinner SIW thickness.

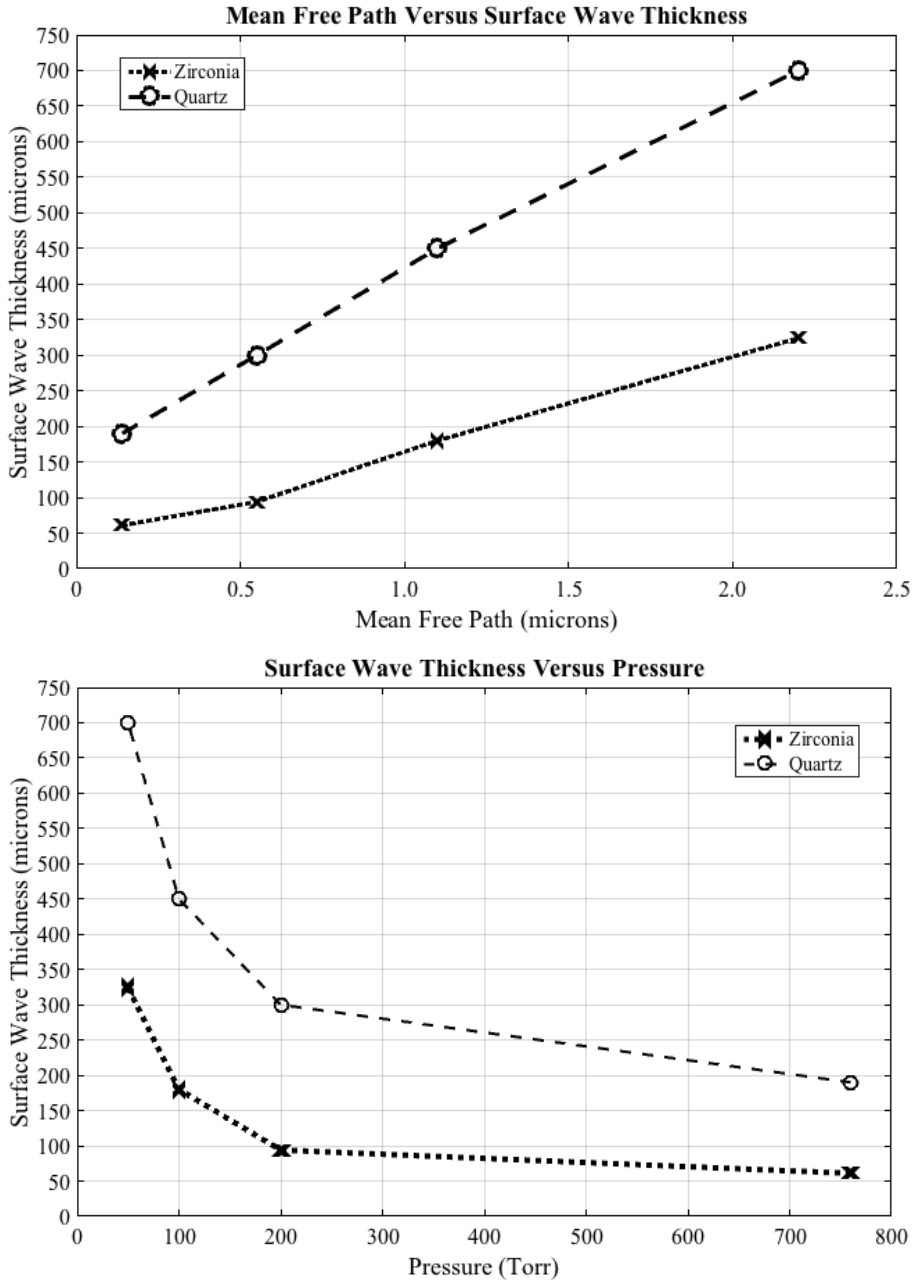

Figure 3-22: Surface wave properties for zirconia and quartz disks. (a) Surface wave thickness as a function of electron mean free path and (b) surface wave thickness as a function of pressure.

Time integrated images over 1 ms were recorded for pressures of 10-200 Torr, and are shown in Figure 3-23 for the zirconia disks. These images demonstrate that in general, the discharge volume increases with decreasing pressure.

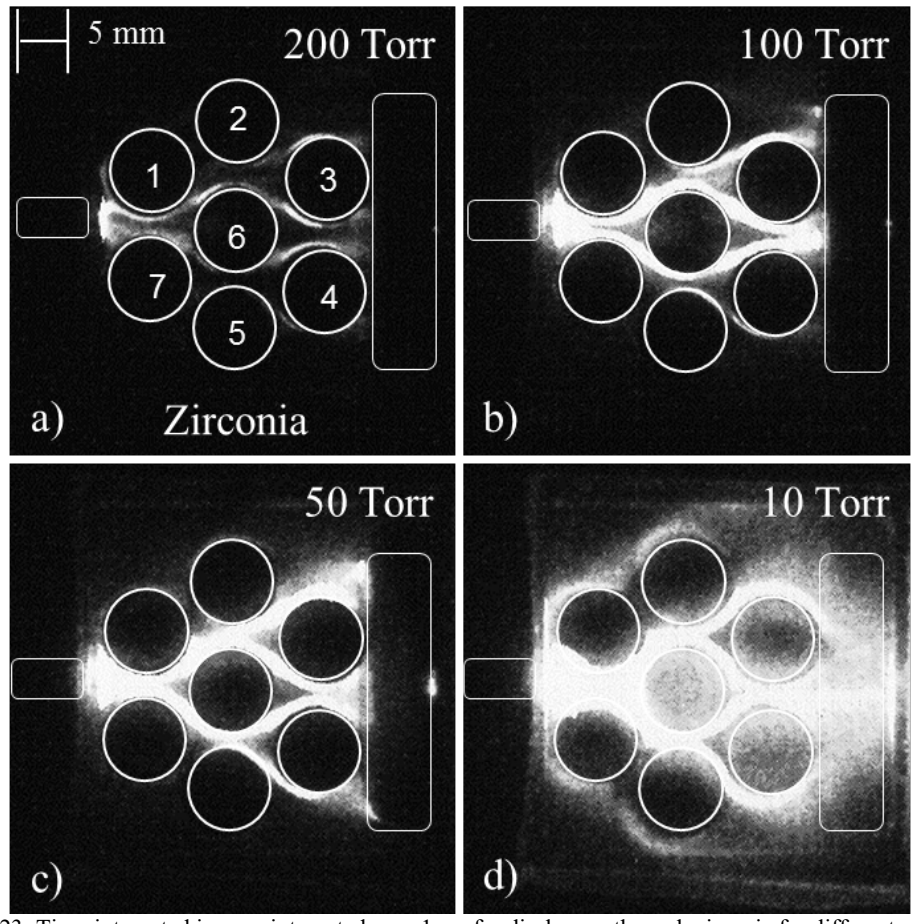

Figure 3-23: Time-integrated images integrated over 1 ms for discharges through zirconia for different a pressure using the macro lens. (a) 200 Torr, (b) 100 Torr, (c), 50 Torr and (d) 10 Torr.

3.6 Modeling of Micro-Discharges: Zirconia and Quartz within *nonPDPSIM*

The modeling effort for the packed bed reactor nanosecond pulsed discharges were first performed under atmospheric conditions utilizing the *nonPDPSIM* computational code developed by Mark Kushner's group as referenced earlier. The solver utilized humid air ($N_2/O_2/H_2O$ = 78/21/1) at atmospheric pressure with the starting temperature at room temperature of 300 K. A more detailed report of the solver initial parameters may be found in the published report.[13] A physical representation of the

experimental setup was generated with a static, unstructured, triangular mesh from the SkyMesh2 application by SkyBlue Systems. Reflective boundary conditions were set on the left-and-right sides of the simulation domain. A depth of 1 cm was assumed for volumetric calculations and the voltage was specified on the top and bottom to represent the electrodes. The electrodes were spaced 1 cm apart with the dielectric disk interstitial spacing set to 700 μm for the base case as seen in Figure 0-24(a). The solver was ran for a set of computations that included changing the interstitial spacing from the base case to 430 μm as well as a 22.5 degree rotation of the outer dielectric disks about the central disk shown in Figure 0-24 (c,d). Figure 0-24 is taken from the publication and is reproduced here. The dielectric constant of the discs is set to that of the quartz material used in the experiment with $\varepsilon/\varepsilon_0 = 4.0$.

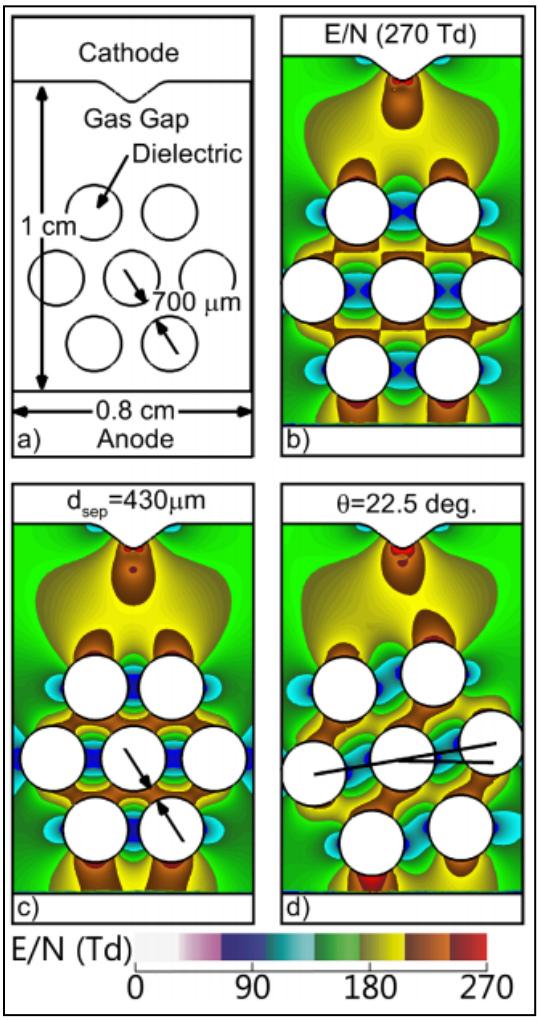

Figure 0-24: Initial conditions for simulations: (a) base case geometry and (b) base case initial reduced electric field, *E/N*. (c) Initial *E/N* for smaller separation between the discs and for (d) rotated lattice. *E/N* is plotted on a linear scale, 22.7-270 Td for total voltage drop of – 30kV in humid air.

When the voltage is applied to the system, an external electric field causes a polarization of the electric field inside the dielectrics, which in turn creates an additional enhancement in the gas electric field at the poles of the solid. This enhancement was shown in the ANSYS: Maxwell simulations previously discussed as well as Figure 3-4 (b). This localized enhancement affects the localized electron densities throughout the aggregate media. The electron density for the base case were found to be varying from 5 x 10^{13} cm^{-3} to 1 x 10^{14} cm^{-3} as a function of time as the plasma forms and propagates through the media and is shown in Figure 3-25 (a-f). The highest electron density is

seen where the modeling shows the highest electric field enhancement and is represented in Figure 0-24 (b) and Figure 3-3. This high electric field enhancement produces the regions of high ionization and in the modeling case presented by colleagues[13], also produces positive restrikes.

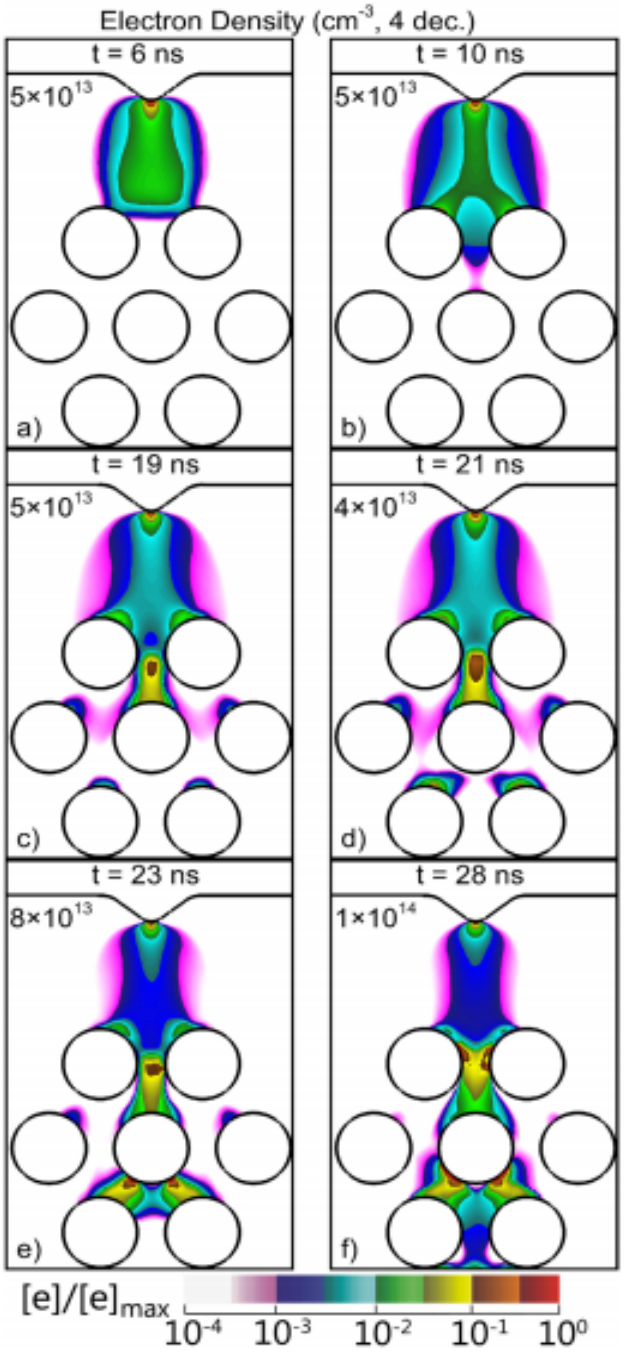

Figure 3-25: Electron density at different times during propagation of the discharge through the PBR for the base case (-30kV, humid air, 700 µm disc separation). Densities are plotted on a 4-decade log scale with maximum value (cm^{-3}) indicated in each frame.

The modeling corresponds well with the experimental data such that the plasma forms and charges up the surface, producing the surface ionization waves from the created tangential components of the electric field. As a result of these actions, the electric field strength between the discs are shown to be a minima that is below the ≈ 30

kV $cm^{-`}$ or 130 Townsend (Td) for the breakdown electric field of air. The speed of streamer propagation was also determined to be on the order of ≈ 2.3-5 x 10^7 cm s^{-1}. The propagation speed of the SIWs along the surface of the quartz disks was ≈ 3 × 10^7 cm/s and ≈ 4 × 10^7 cm/s for the zirconia disks.

The next case that was simulated within *nonPDPSIM* was decreasing the interstitial disc spacing from 700 μm to 430 μm. The reason for decreasing the spacing of the discs is to have a higher packing fraction and therefore simulate more aggregate in the same volume. The results of this change led to the electric field shown in Figure 0-24 (c). The closer spacing and higher fraction led to a higher enhanced electric field within these regions of interest. At first, the discharge propagates in the same fashion with interaction first occurring with the top two discs. Moving forward, the electric field was nearly 20 Td lower at the middle point of the aggregate and therefore lowers the electron temperature and electron impact ionization events. Therefore, the electron collisions from the region are dominated by attachment. Here a difference seen between the base case and the higher packing fraction case is that the positive restrike is not observed in this region. The electron densities at the closest point of contact amongst discs did however see nearly a two times larger density than in the base case but is not a significant change. The main difference between the base case and this of closer spacing is that the closer spacing promotes formation of FMs while delaying the onset of SIWs.

Following the work involving a more closely packed base case, a model was performed with a 22.5-degree rotation about the central disc. The reason for this is that the localized enhancement of the electric fields is due to the dielectric discs and their positions relative to the electrodes. A 22.5-degree rotation sets the one of the discs closer

to the pin electrode and therefore modifies the localized electric fields represented in Figure 0-24 (d). The closer proximity and better alignment with the electric field leads to a more intense FM discharging from the pin electrode to the now closest disc. The recorded electron impact ionization peaks at nearly 1 x 10^{21} cm^{-3} s^{-1}. The asymmetry produces a difference in location and magnitude of the E/N minima and allows for propagation from the 'closest' disc to the pin electrode to the now slightly offset one. The plasma then discharges along the right side as shown in Figure 3-26 (a-f).

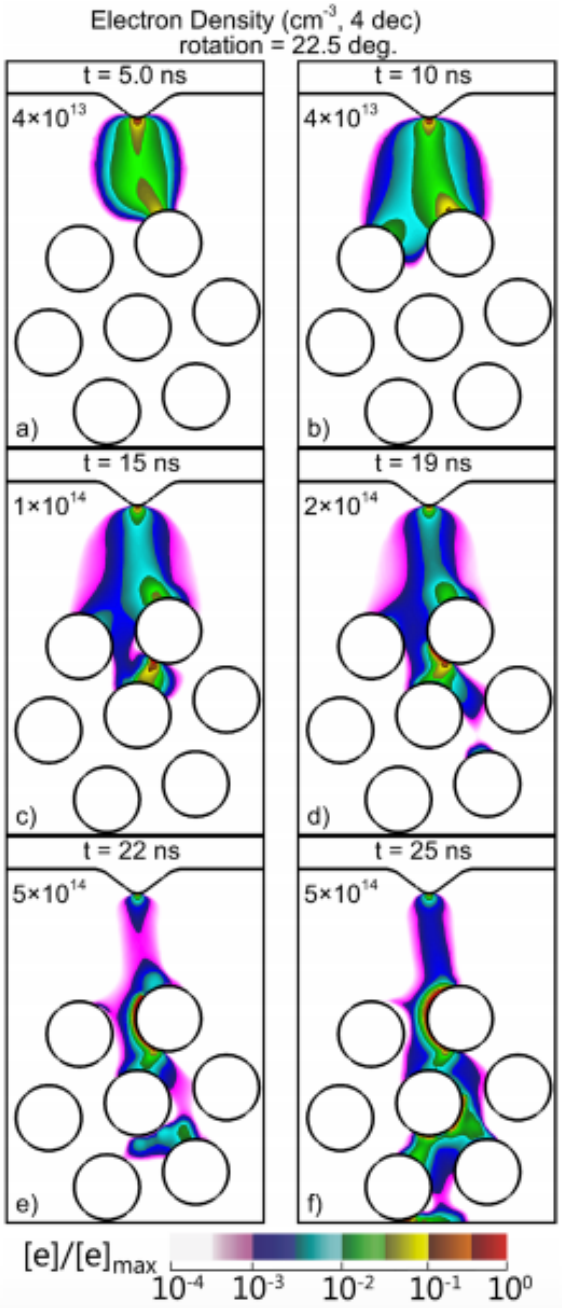

Figure 3-26: Electron density at different times during propagation of the discharge through the PBR for the rotated lattice (-30kV, humid air, 700 μm disc separation, 22.5° rotation). Densities are plotted on a 4-decade log scale with maximum value (cm^{-3} s^{-1}) indicated in each frame.

The discharge follows the discs that have become physically closer to the pin electrode due to the better alignment with the background electric field of the electrodes. A favoritism of the closest disc to the planar electrode is seen in Figure 3-26 (f) as shown by

the electron density map showing a shift in the more favorable path after reaching the central disc.

A key component of the *nonPDPSIM* modeling that provides excellent insight into the system is the ability to determine densities of the various species produced by the plasma. The results of the model show that the dissociative attachment reactions of O_2 into O and O^- begin to dominate the gap between the top two discs as they move towards the central disc in direction of the electric field. The electron temperatures determined by the model in the ionization front suggests around 9 eV with E/N of ≈ 600 Td (150 kV cm^{-1}). The resulting feature of such high field strength and temperatures lead to surface-hugging electron and ion densities and small volume discharges, high density discharges. The SIW propagation also led to an increase in OH densities with numbers exceeding values as high as 1 x 10^{13} cm^{-3}.

The variations in packing led to differences in the streamer propagation and formation as previously discussed and these were then correlated to species production. Over the course of the first two nanoseconds of the simulation, the densities of discharge species were pretty similar with O on the order of 2.5 x 10^{11} cm^{-3}, N recorded as 1 x 10^{11} cm^{-3}, and the initial electron density of 5 x 10^{10} cm^{-3}. Each of the aforementioned species stays similar until nearly 12 ns, about the time the discharge propagates towards the central disc. At 12 ns, a significant difference in N production, n_e density gain or loss, and then slight contrast in the generated OH and H_2 species. Figure 3-27 (a-c) visualizes the species population trends as a function of time. The total species is defined as the volume integral of the density of that species. Looking particularly at Figure 3-27 (b),

spikes are seen in the densities of various species and may be attributed to either the restrikes or SIWs.

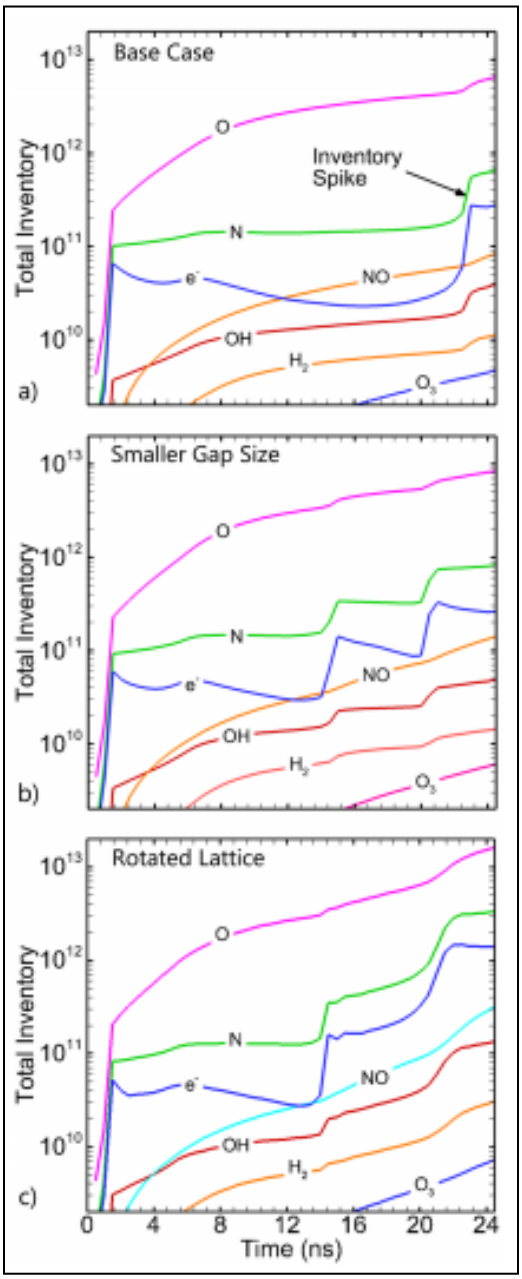

Figure 3-27: Time evolution of the total inventories of reactive species: (a) base case, (b) smaller separation between discs, and (c) rotated lattice. Total inventory is the unitless total number of atoms or molecules representing the volume-integrated density of the species throughout the reactor.

For the rotated lattice, a lack of geometrical symmetry promotes more development of SIWs and provides insight as to how symmetry may affect reaction kinetics. The spikes seen with N, O, and OH correspond to the sharp increase in electron

densities as the reaction mechanisms for the neutral reactant species depend on high electron densities with high energies. The sensitivities of their species populations may be further investigated in the work of a colleague.[49]

The modeling effort presented here was an excellent comparison to the experimental results observed in the proceeding sections. The plasma discharge through the dielectric aggregate was driven by the physical geometry of the discs and their localized field enhancement. The streamers started as FMs from the pin electrode to the nearest disc, instigating morphology of the electric field that transitioned these FMs to SIWs. As the SIWs reach the next interstitial spacing gap, they transitioned back to FMs as the process repeated itself as it progressed through the media. Decreasing the distance between the disks resulted in increased peak and average electric fields but did not change the breakdown mechanisms. A rotation of the lattice did however result in more intense surface ionization waves from asymmetry. The largest changes in species densities were seen at the short transient stages of the system such as restrikes or the development of SIWs. Overall, the physics seen in the model and the experiment provided an excellent comparison and shed light onto the expected parameters of the plasma as more measurements are continued to be made.

3.7 Discharge propagation in the presence of catalytic particles

A key interest in the focus of plasma formation in packed bed reactors or porous media is that of the effects of catalytic particles. Implementing materials such as silver, platinum, gold on the surfaces of dielectric modify the plasma formation and propagation. These developments are not well understood and therefore presented are some preliminary results into the effects of catalytic particles implemented on a dielectric disk within the aforementioned 2d cell apparatus. A question of interest to the field that is

highlighted in this thesis is: *How does the presence of metallic particles affect DBD discharges in PBRs?* Other questions that reside for future work include: *What catalyst depositing manufacturing processes produce additional plasma structures within various media? What are the plasma characteristics on the surface and near the catalytic structures? What species are generated within these catalytic plasma regions? How is energy transferred to the catalyst? Does plasma negatively impact the lifetime of the catalyst material?* The answers to these questions may be found in experiments with optical emission spectroscopy diagnostics, thermal imaging, as well as additional time-resolved high speed imaging.

Zirconia dielectric disks were chosen as the dielectric aggregate for this experimental investigation. An identical placement to Figure 3-2(b) was chosen with dielectric disk 1 having three lines of conductive silver epoxy painted on the radial surface. The three positions where the catalysts were placed are at the interstitial region between disks 1 and 7, the FM location between disks 1 and 6, and the interstitial region amongst the three disks.

Figure 3-28 shows time-resolved imaging of the disk in which the catalytic epoxy was placed. The initialization of plasma formation within the first 5 ns (Figure 3-28 (a)) is identical to what was seen earlier with FM formation from the pin electrode to the first set of disks as well as FM development at the interstitial positions between disks. After the first 5 ns, however, we begin to see differences in plasma propagation along the surface yet still producing the more intense filamentary micro-discharges as seen before. In Figure 3-28 (b), we see FM formation as well as SIW propagation but the volume of the SIW near the catalyst is much larger than observed with the unmodified ceramic.

Continuing to images (c) and (d), one can clearly see how the volume of the SIW propagation is much larger than the neighboring dielectric with a surface hugging SIW. The plasma then continues to reside near the catalytic particles positions after the wave has already progressed to the next dielectric disk. Image (d) is an excellent example of where the catalytic particles are located after the plasma front has moved beyond this location. Each 'bright' spot is a location of the catalyst. The residual plasma here grants insight into the potential manipulation of the remaining plasma near catalytic particles in packed bed reactors or porous media.

The longer residence time of the plasma at these locations may be taken advantage of in order to enhance kinetic reactivity or selectivity of the application. Plasma-catalytic synergy has been observed by Neyts et al. in their study regarding synergistic effects at the nanoscale level[51], as well as in other works.[52,53,54,55] Therefore a dual interest is produced where the locally residual plasma increase potentially desired reactions with the catalytic material and the residence time of the plasma in this location is greatly enhanced. For instance, images taken with dielectric aggregate without catalytic particles show localized emission with the microscope lens for around 25 ns before any residual plasma is difficult to observe.

Figure 3-28 subsections (e,f) are evidence that the plasma resides in the region much longer than with the non-catalyst dielectric.

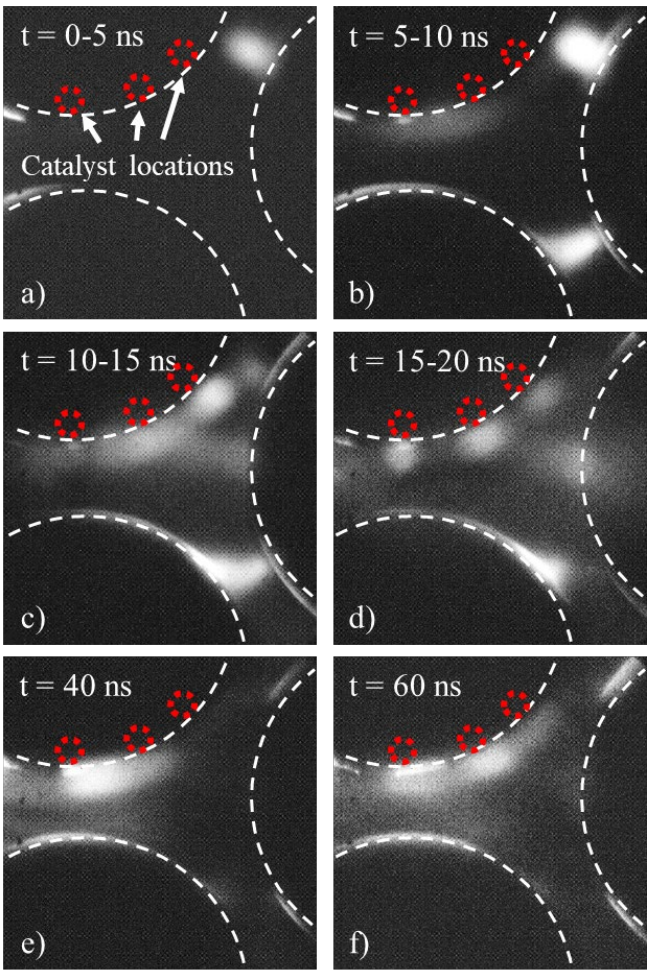

Figure 3-28: Time-resolved images of plasma formation and propagation of disks 1, 6, and 7 with conductive epoxy acting as a catalyst. Catalyst locations have been highlighted with small dashed circles. The images show that the intensity of the residual plasma remains relatively high near the catalyst after time in which the intensity would be low without the catalysts.

Although only 60 ns after pulse initiation is shown in the figure, residual plasma was seen up to 200 ns after the first image is taken, albeit at a much lower intensity. Such a large increase in residence time of the plasma may greatly increase the efficiency or reactivity of the system.

To further gain a better understanding of the plasma interactions with the same catalytic particles, the polarity of the electrodes was reversed such that the pin electrode now held a –10 kV whereas before it was a +10 kV setting. The same polarity and voltage switch also occurred at the planar electrode, leaving the system with a 20 kV potential difference from the pin to planar electrode. Figure 3-29(a-f) shows the time-

resolved imaging of the plasma formation and propagation under such a polarity switch. Since the plasma formation begins near the planar electrode and propagates from right-to-left of the dielectric disks with catalytic particles, a noticeable difference was seen in the plasma production.

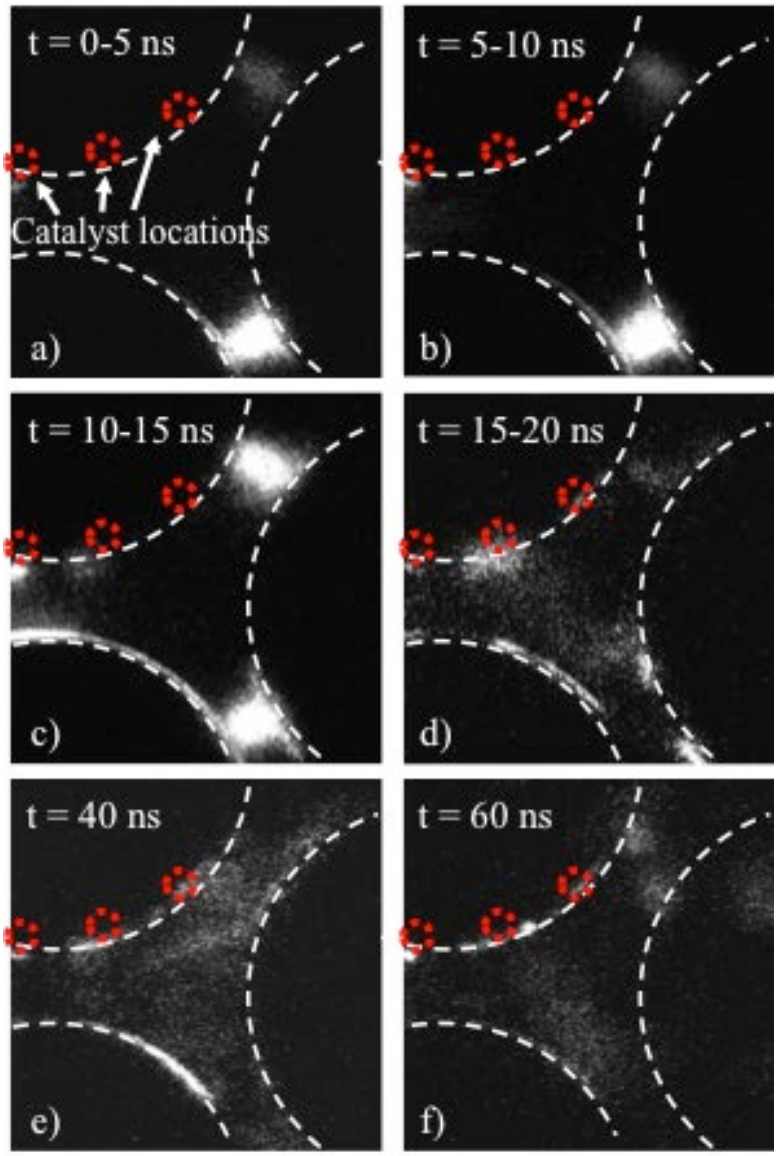

Figure 3-29: Time-resolved images of negative polarity pin electrode to positive polarity planar electrode configuration utilizing catalytic particles on a dielectric disk. Images (a-f) show a time progression of the plasma formation and propagation through a select region of the 2-dimensional cell setup.

For the positive polarity pin electrode system, plasma first forms on the dielectric disk with the catalytic particles and its lower neighbor (disks 1 and 7). The plasma then remains near the catalyst locations as the time-step was moved forward with an easily

observable intensity at the pre-set iCCD gain and exposure. Utilizing the same setup for the negative polarity pin electrode resulted in a much lower intensity image capture at the same time delay step that was recorded in

Figure 3-28(f). A possible explanation for the disparity in localized optical emission spectroscopy intensity may be due to the plasma propagation through the medium varying. Before with the positive polarity, FMs formed and transitioned to SIWs in a left-to-right fashion in regards to the camera orientation. Implementing a polarity reversal forces the plasma to have to propagate further in order to reach the location of the catalysts. This increased distance allows for more plasma dissipation to occur and therefore less-intense plasma was witnessed. In agreement with the original polarity of the system, residual plasma does occur and remain near the catalytic particles for an increased duration versus ceramic only material. The volume and intensity of the inverted polarity was more diminished.

Modeling of catalytic particles in the 2-dimensional cell setup was performed by Juliusz Kruszelnicki within *nonPDPSIM.* The catalysts were modeled as dielectrics with $\varepsilon_r = 10$ and with metal-like conductivity with sigma = 100 Ohm^{-1}-cm^{-1}. In this case study, the nominal properties of silver were chosen to reflect the silver epoxy in the experiment. The work function of silver is 5 eV. Thermal conductivity was set to 4.06 W-cm^{-1}-K^{-1}. Thermal capacity was 0.023 J-cm^{-3}-K^{-1} and reflectance was set to 0.4. Surface reactions implemented for the catalytic modeling include recombination, de-excitation, recombination, and secondary electron emission. Surface heating of the material was calculated by extending heat conduction term of the temperature equation of plasma into the solid materials. These were the fluxes of plasma produced species onto

the surface that include ion potential energy, ion kinetic energy, neutral enthalpy changes, electron kinetic energies, electron emissions, and ultraviolet heating. The computational workings of the model were the same as specified in section 3 of this chapter.

The electric field near the catalysts is greatly enhanced, more so than with the dielectric alone. This is due to electrons seeding the catalysts and more easily producing micro-streamers at the edges of the catalyst. The electric fields at the catalyst locations were recorded of having strengths in the 1000s of kV/cm within *nonPDPSIM* and were able to overcome the work function of the material and field emit. The local enhancement due to the catalytic material is also geometry dependent and would be further enhance if the catalysts were modeled with points instead of the smooth surfaces matching the modeled discs.

Thus far, the preliminary experimental remarks with the silver epoxy catalyst show that they do have an effect on plasma formation and propagation through the media. The field strengths are high enough to induce electric field emissions within the catalytic region. The additional emitted electrons increase plasma conductivity near the catalyst and therefore decrease electron temperature and fluences. Juliusz's modeling work has shown that the geometry of the catalysts play a big role in the field emissions as well as suggesting that ions are main contributors to the surface heating of the catalyst. The implementation of synergy particles allows the plasma to bring the catalyst temperature above the "light-off" conditions for chemical conversion processes.

Figure 3-30 shows the electron density due to the implementation of the catalytic particles in the 22.5 degree rotated lattice structure. As is shown in the figure, the electron density from the disc with the catalytic particles to the central disk has a

significantly higher density remaining near the catalysts after the propagation front has already passed through the region. The higher density of electrons lingering in this region was seen in the experimental imaging of

Figure 3-28 (f) and Figure 3-29 (f). The effects of catalysts on pulse-to-pulse variations and material degradation are left to future work.

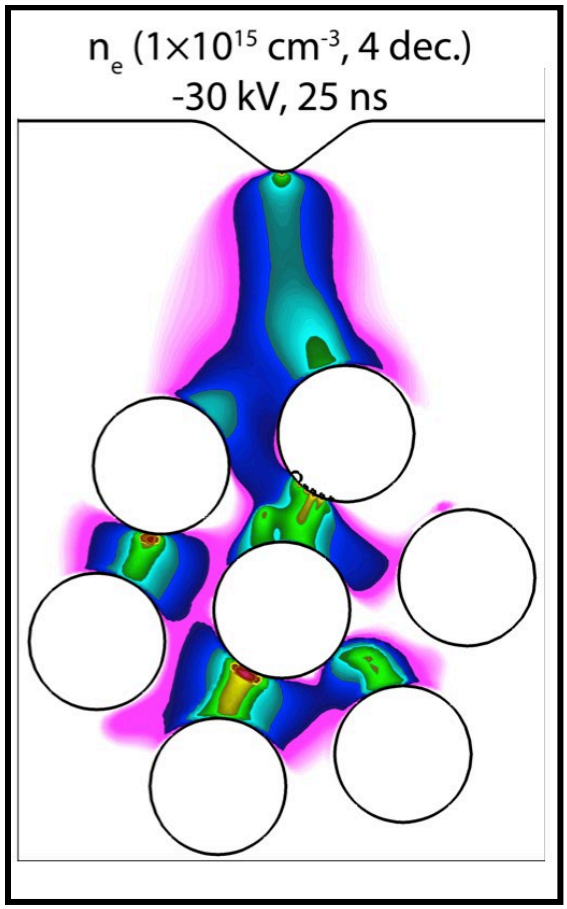

Figure 3-30: Electron density mapped out over the 22.5 degree rotated lattice structure of dielectric disks within *nonPDPSIM.*

Further work with catalytic particles should be investigated with the 2d cell setup as well as moving to catalytic implementation within 3-dimensional PBRs. For instance, the location of the catalytic particles with reference to the electrodes should change with time-resolved images being captured to further glean insight into the plasma propagation with catalytic particles in larger. Utilization of a 3d PBR and catalytic particles would

show how the plasma propagation outward in three dimensions would be effected. Some questions that still remain are ones as follows: Would the plasma now prefer the catalytic particle path and no longer propagate throughout the aggregate? Or would the plasma intensity and volume increase as more catalytic particles are added? Is there a saturation limit to the amount of catalytic material?

3.8 Validation of 2-D results using 3-Dimensional Sub-scale PBR

Construction of a sub-scale packed bed reactor was completed in order to validate the results of the 2-dimensional cell. The dimensions of the sub-scale reactor was chosen such that there was a layer of dielectric spheres that were in contact with identical dielectric spheres. Physical interaction with other dielectric spheres is therefore representative of a true packed bed reactor or porous media with interstitial spaces in each dimension. Figure 3-31 shows a quartz tube of 19 mm outer diameter with a 17 mm length allowed for six silicon nitride (Si_3N_4) spheres to become the packing aggregate with a dielectric constant of 8.

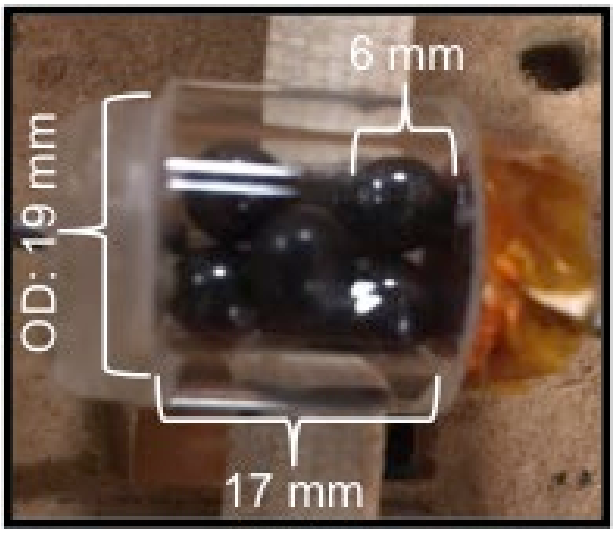

Figure 3-31: Image of the sub-scale, 3-D packed bed reactor utilizing Si_3N_4 as the dielectric aggregate. The sub-scale reactor was designed and built to validate the results of the 2-D experiment.

The sub-scale reactor dimensions allowed for optical, time-resolved imaging of the plasma as it travelled through the system without interference of overlapping layers in

a larger volume system with similar aggregate size. The sub-scale reactor implements a pin-to-planar electrode configuration with the pin electrode of stainless steel and the planar electrode remaining copper as seen before with the 2-D cell experiments. The pin electrode was mounted via a hole drilled through a copper cylindrical cap and set in location via epoxy.

Images taken were then compared to discharges seen with the zirconia disks of the 2-D cell results. Figure 3-32 shows the time-resolved images captured in similar fashion to that mentioned for the 2-D cell. As one can see in Figure 3-32 (a), the plasma first forms the FMs from the electrode to the first set of dielectric spheres and transition to SIWs. Proceeding to the next 5 nanosecond exposure in (b), the SIWs transition to more intense FMs near the points of contact for the middle dielectric spheres before continuing along the surface of the middle spheres towards the planar electrode. These images of the sub-scale reactor show similar behavior to the time-resolved images of the zirconia disks as seen in Figure 3-11 of this chapter. An interesting observation that should also be commented on is that a faint SIW along the inner diameter of the quartz tube was produced.

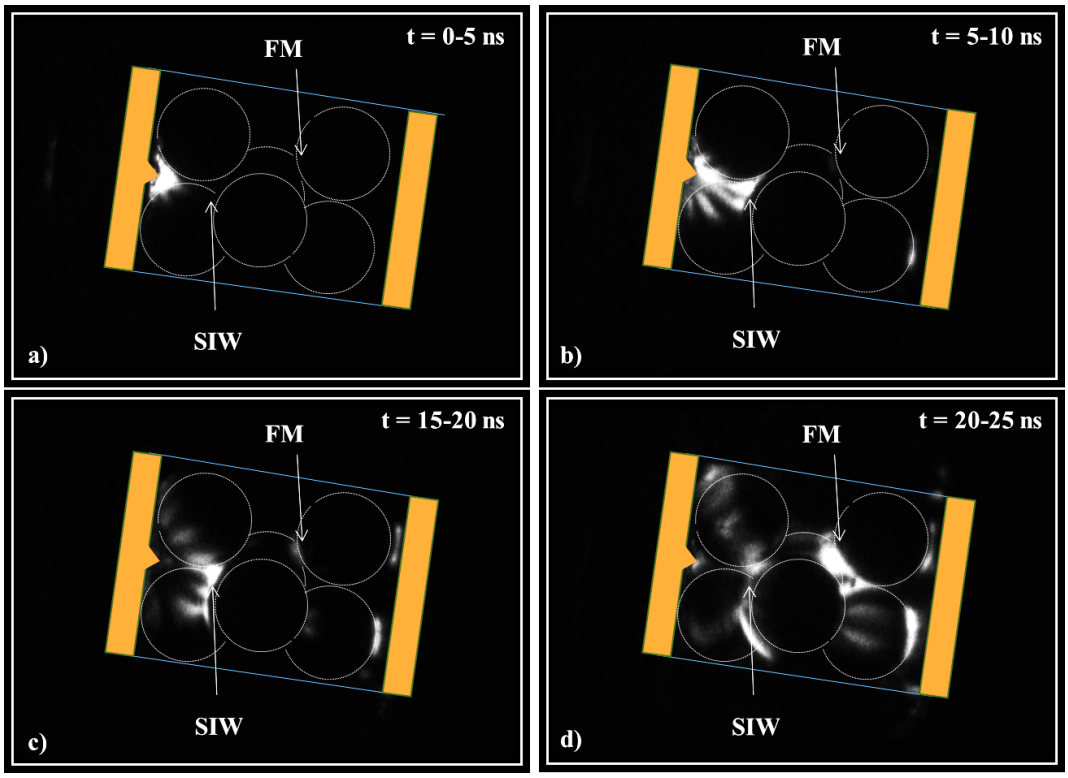

Figure 3-32: Time-resolved images of plasma formation and propagation within the sub-scale 3-D reactor. (a) Shows plasma formation as a FM with (b-d) showing FMs and SIWs.

This SIW is very difficult to spot without using significant image enhancement that was not done in Figure 3-32. Although lacking in intensity, this SIW arrives at the planar electrode approximately 5-10 ns before the FMs and SIWs propagating throughout the aggregate. This may also be a geometric factor in which the distance along the inner diameter of the quartz tube is similar to traversing the volume across the dielectric aggregate. A study for this geometric factor would involve a packed bed reactor with a quartz tube inner diameter significantly larger than the distance between electrodes with a similar pin-to-planar electrode configuration. Further investigations should be performed to determine the properties of the wave and its influence on the system.

Chapter IV

A Spectroscopic Study of Plasma Emissions from the 2-Dimensional Discharge

The species produced in the non-thermal packed bed discharge are essential for applications such as agriculture, medicine, fuel reforming and chemical processing. In order to understand the species that are being produced during the discharge, optical emission spectroscopy is utilized. Time resolved spectra were acquired using a Princeton Instruments Pi-MAX3 camera coupled to the Acton SP2300 spectrometer. The spectrum was analyzed via the Winspec software. SpecAir was used to obtain the gas temperatures from rotational structure.[56] Gas temperature is found by fitting synthetic spectra to the measured emission. The electronic excitation temperature was determined via Boltzmann line plots as described in Chapter 2. While not the actual electron temperature, the Boltzmann plot is a qualitative measure of how close the electrons are to LTE and yields the trends in average electron energy.

4.1 Species evolutions as Inferred through 2-D emission map

In order determine the species distribution within the 2-dimensional packed bed reactor, images were taken with wavelength filters placed over the lens of a Nikon camera. Although the images are qualitative in nature, they provided insight as to the relative abundance of species generated. Here filters were chosen to coincide with emission bands of various species such as nitrogen, oxygen, and NO_x. Figure 4-1

illustrates the spectral band-pass of a filter used in this work. The band-pass filters were employed to visualize the location and intensity of light emitting species within the discharge for OES observation. The band-pass width of the filters was approximately 20 nm. Figure 4-2 shows images taken with a Nikon D40 camera with the band pass filters placed in the view of the discharge. It is a visual representation of the observable emissions through the selected filters. The highlighted region is the placement of the filter with the rest of the discharge remaining covered.

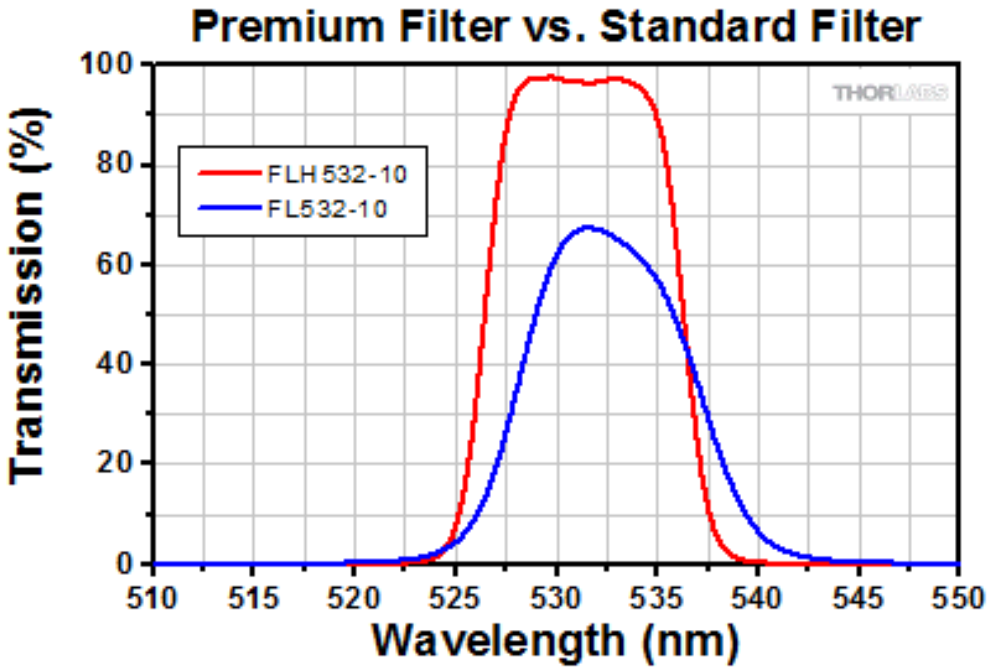

Figure 4-1: Example of the band-pass filter transmission spectrum taken from ThorLabs website. The red line is representative of the filters used in the qualitative diagnosis discussed herein.

The center wavelengths of the filters used in this work are listed in Table 4-1 along with species with prominent emission lines in range of the filter that are of interest.

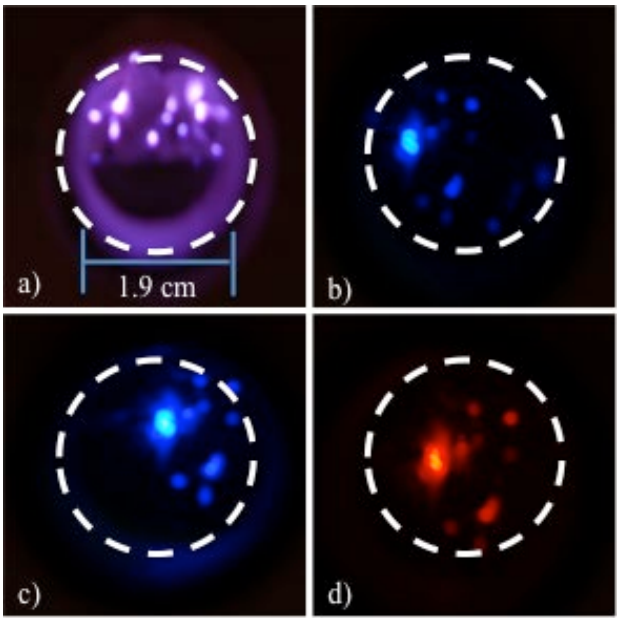

Figure 4-2: Exposure images of the Nikon D40 camera using the (a) no band-pass filter, (b) 400 nm filter, (c) 420 nm filter, (d) 600 nm filter.

Table 4-1: Table of the utilized band-pass filters for the qualitative optical emission spectroscopy.

Wavelength Center-Lines of band-pass filters used for qualitative OES Analysis				
307 nm O	421 nm O_2	450 nm NO, NO_2	500 nm	550 nm
600 nm O_2^+	650 nm N_2	700 nm	750 nm	777 nm O

The filtered images were also taken with the Andor iStar camera. The Andor camera allowed for higher sensitivity. The band-pass filters that were used in the previous images were also employed here with addition to a 250 nm, 221 nm, and 232 nm center-line filters. The images were taken as a qualitative comparison of the species produced with the quartz aggregate verses the zirconia aggregate, which have very different dielectric constants. Images were taken at 40 ns into the pulse and were accumulated for a total of 500 images to increase the contrast and are shown in Figure 4-3.

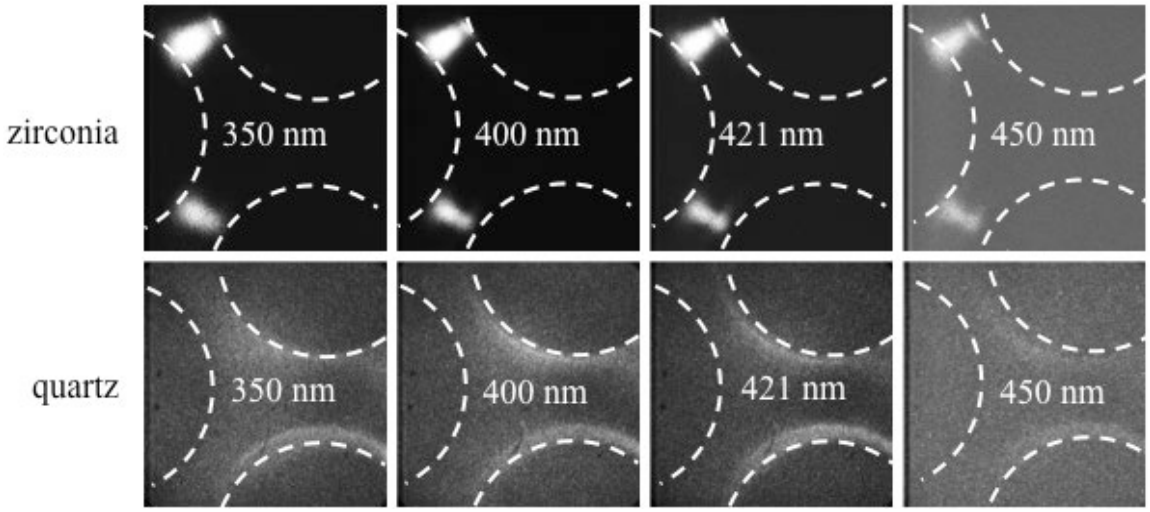

Figure 4-3: Accumulations of the discharge shown through a band pass filter at the same time step for each of the dielectric aggregate. The centerline of the filter is on the 2.4x magnified image.

For the zirconia aggregate, the filamentary microdischarge is the dominant mode observed at the time delay with the surface ionization wave dominating the discharge mode at same time step with the quartz aggregate. The contrast in visual observations shows the intensity of the plasma, corresponding to the higher emission intensity of the species within the filtered wavelengths.

4.2 Collected OES Spectra for Inorganic Material

Time resolved emission spectra were also obtained at select locations of the 2D array. The objective here is go gain insight into the time variation in species excitation as the ionization wave passes through select locations in the array. This measurement also allowed for the measurement of emission signatures of surface and filamentary discharges. The experimental setup with the labeled positions of interrogation for the optical fiber is shown in Figure 4-5. The first position to be investigated was between dielectric discs 1 and 2. The second position was between discs 2 and 3. The last position to be investigated was between the dielectric discs and the copper planar electrode.

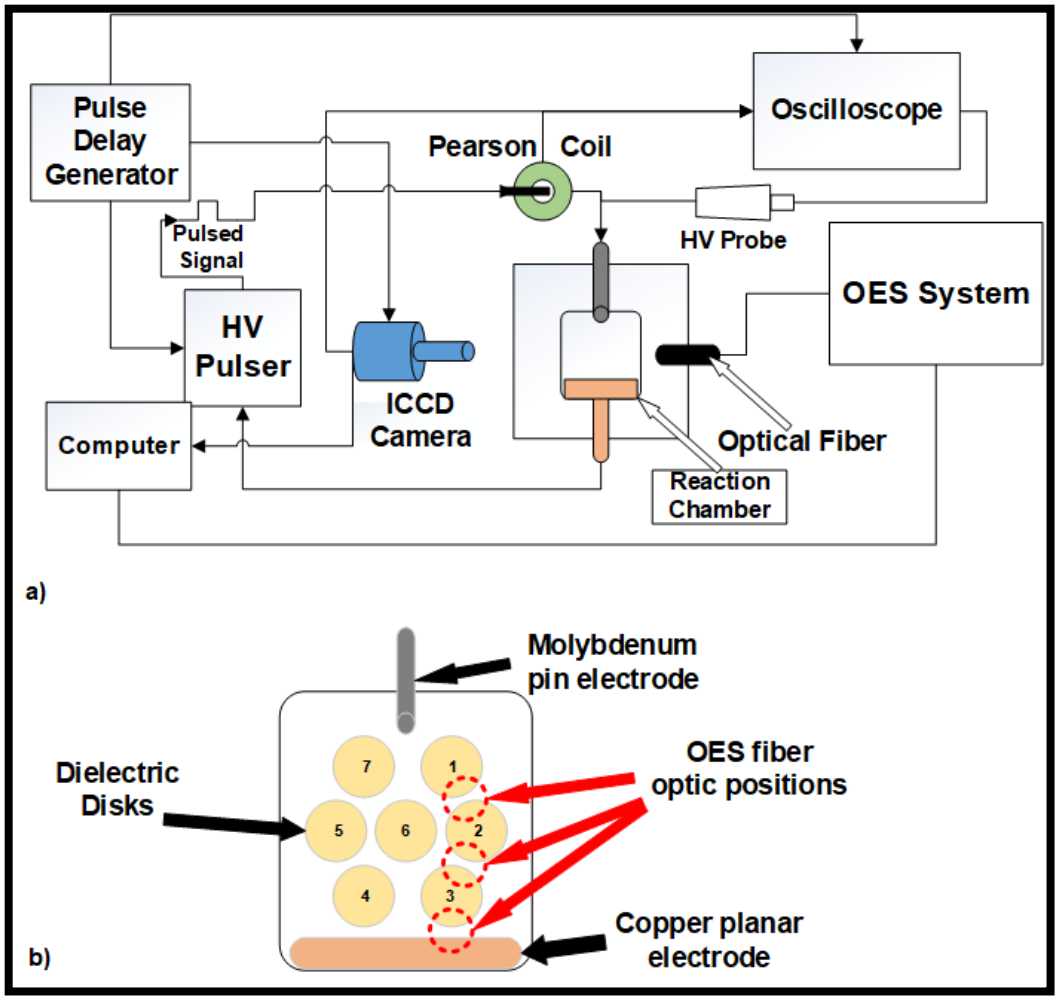

Figure 4-4: The experimental setup for the time-resolved optical emission spectroscopy results is shown in (a) with the region of interests shown in (b).

Images were taken over the duration of the pulse as well as the afterglow at a 10 ns exposure. The typical emission spectrum is at one snapshot in time of the highest recorded intensity is shown in Figure 4-5. The full spectrum shows mainly nitrogen band emission along with peaks from copper and molybdenum (electrode material). The arrow underneath the Cu I and Mo I show the range over which emission spectra from the electrodes were seen. A broad range is shown here as the peaks are too numerous to label.

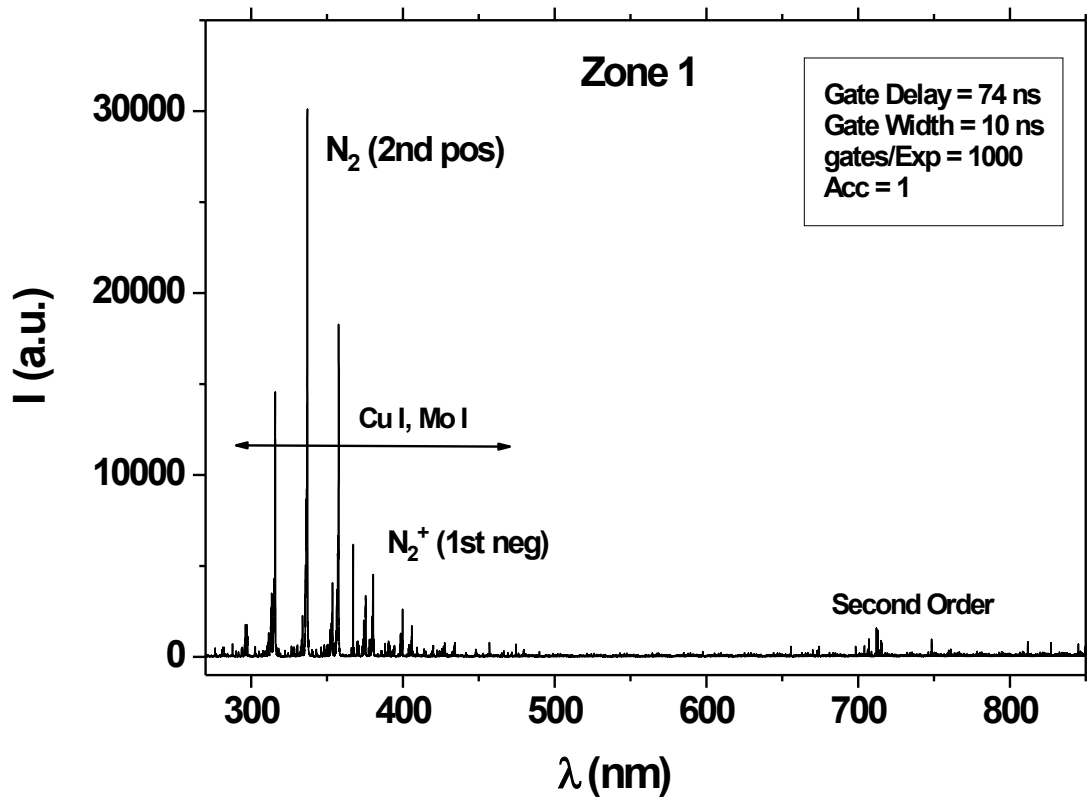

Figure 4-5: The full spectrum obtained at location 1 before the time-resolved results was focused on the nitrogen 337 nm line.

The time evolution of emission at 337.1 nm was selected to monitor plasma induced emission as the ionization wave passed through the array. This nitrogen bandhead emission associated with the second positive nitrogen band was strong for all measurements. The emission was time resolved as a function of not only position but also pulse frequency (10 and 100 Hz). The first location scrutinized, as a function of time was position one, which is between the zirconia dielectric, discs 1 and 2. The time averaged gas temperature at this location was 345 K. The time average was performed over the course of the plasma discharge. The intensity of the 337 nm band peaks near 50 ns into the pulse as shown in Figure 4-6.

Interestingly there are two peaks present in the time resolved emission. The second peak appears around 20 ns after the initial peak. The actual origin of the second

peak is somewhat puzzling. It is possible that it is a restrike (assuming 10^8 cm/s streamer speed, then restrike would take ~10-20 ns to reach the location). However, it is most likely the peak could be due to sheath collapse. After the pulse the density increases and the sheath collapse due to shielding and so regions near the surface go dark as there is no longer much electric field. But once the pulse magnitude is subcritical, the sheath expands again and in this case one would observe a rise in emission following decay due to diffusion. This phenomenon is observed in electric field measurements in nanosecond point to point discharges.[57] The actual mechanism is left to future work.

Figure 4-6 also shows how the intensity profile varies as a function of frequency. It should be pointed out that at higher frequency (greater than 2 kHz), the energy per pulse may be decreasing owing to the limits of the power supply. Another possible mechanism is simple charge. The lower frequency gives deposited charge more time to dissipate between pulses. Note it is the accumulation of the charge on the surface that quenches the discharge. And here essentially unipolar pulses are featured.

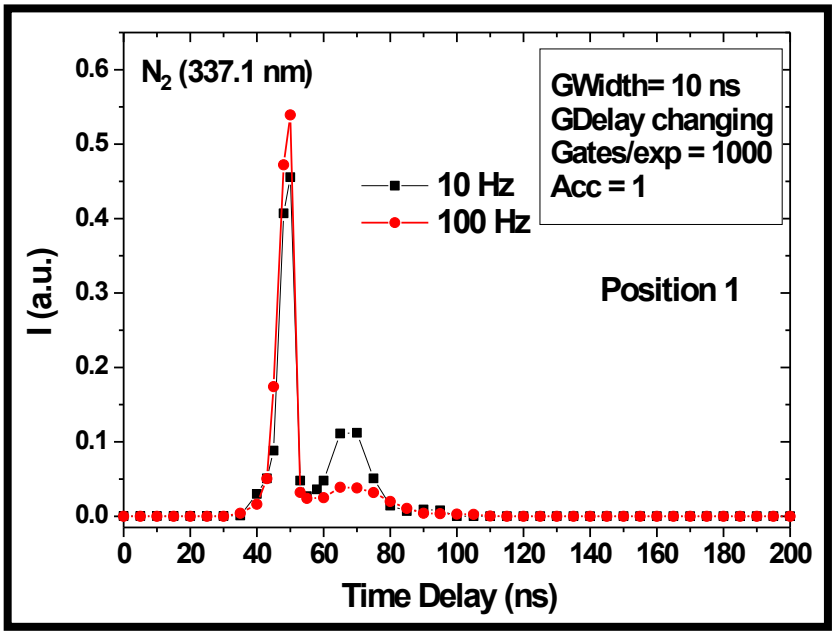

Figure 4-6: Time-resolved emission spectra of the 337.1 nm second positive nitrogen band as a function of frequency at position 1.

The temporal variation in the peaks as shown in Figure 4-6 correlated well with time resolved images of plasma propagating through the array. The filamentary microdischarge is clear seen after 40 ns of delay and is seen to dissipate as the delay for the image capture is increased before increasing again during the possible restrike or sheath collapse time. The images presented in Figure 4-7 show the 337.1 nm line correlation with discharge morphology at 10 Hz.

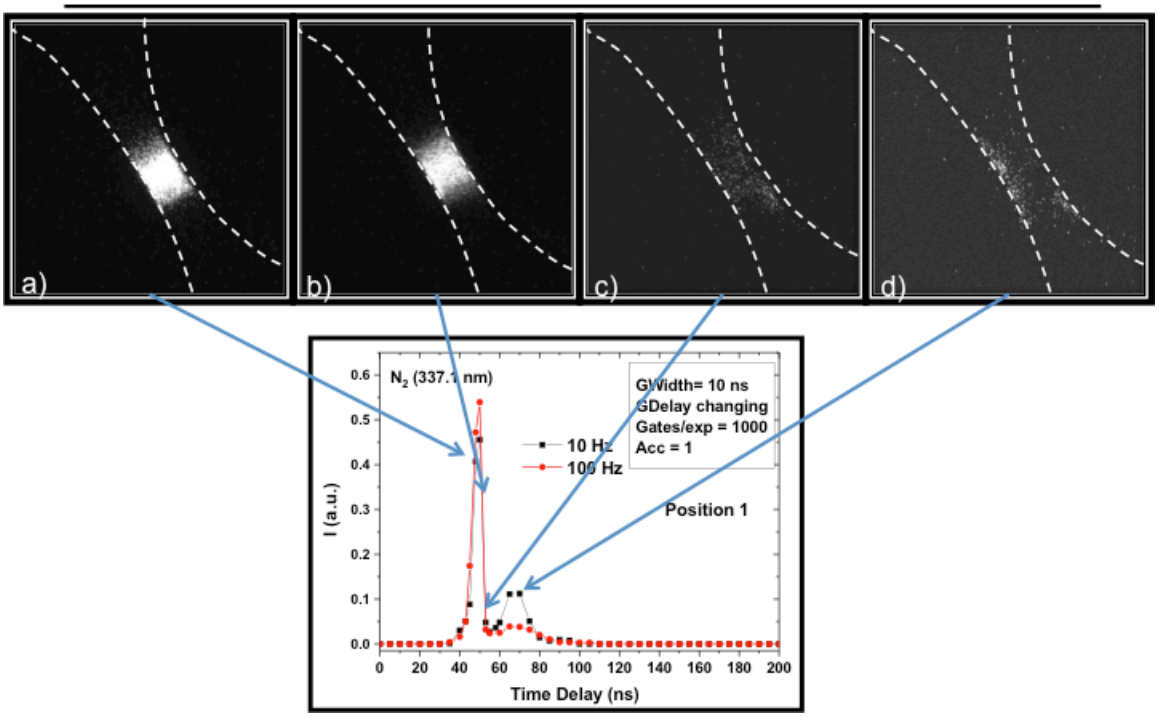

Figure 4-7: Time-resolved images during the optical emission spectroscopy measurements. The images are correlated to the intensity measured at each of the labeled time-steps for the 10 Hz pulse.

The results for the 100 Hz case are shown in Figure 4-8. A similar trend is observed with the exception that intensity of the forward strike for the 100 Hz data had a higher count, suggesting a possible frequency effect—which may have implications for optimizing packed bed reactors.

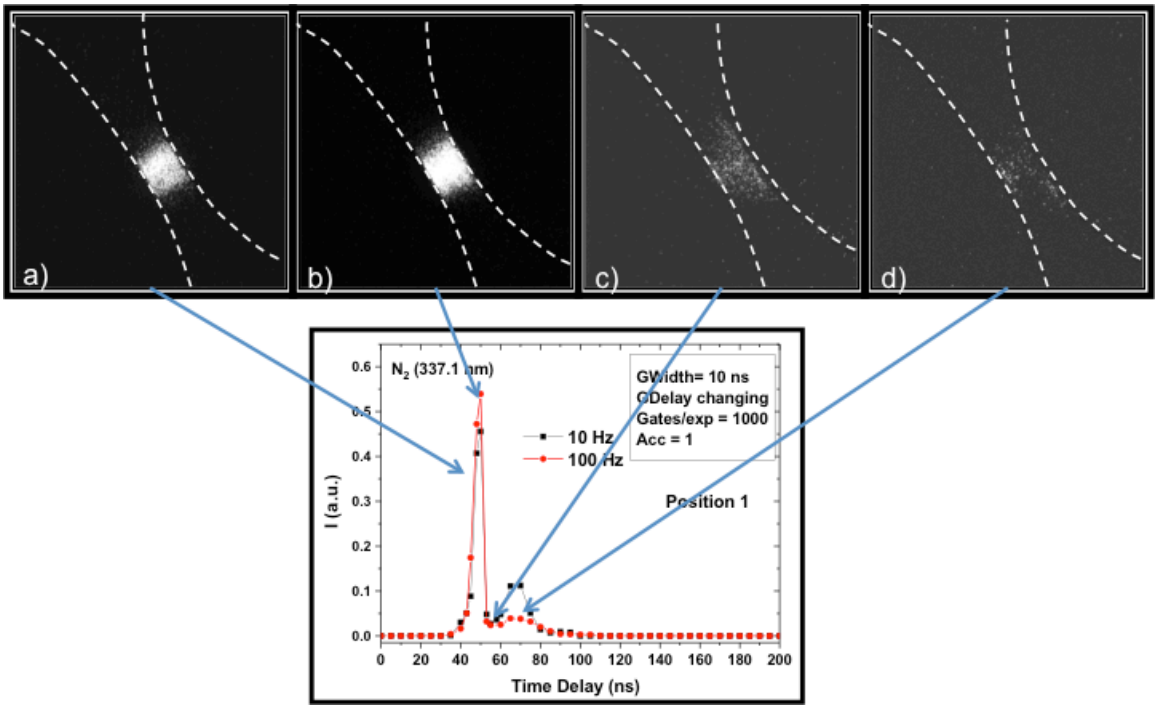

Figure 4-8: Time-resolved imaging of position one at 100 Hz pulse frequency that is correlated to the intensity of the 337.1 nm second positive nitrogen band emission.

Similar data was collected at 10 Hz for position two located between discs 2 and 3 as shown below in Figure 4-9. The normalized intensity at position two was only a fifth of the intensity discharge for 10 Hz that was seen with position 1. The difference in intensity is due to the relation of position to the positive electrode as well as overall position with the applied electric field. Since the positions of dielectrics 2 and 3 do not provide the most direct path from the pin-to-planar electrode for plasma propagation and formation; therefore, a less intense discharge is observed.

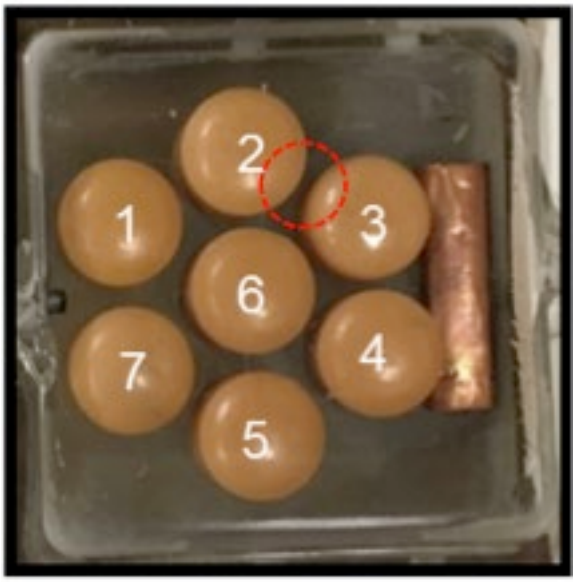

Figure 4-9: Image representing the second location of investigation between dielectric aggregate labeled 2 and 3.

The emission intensity at position two is presented in Figure 4-10. A slight shoulder rather than a distinct second peak was observed at this location. Evolution of the discharge correlates well with images here as well as shown in Figure 4-11.

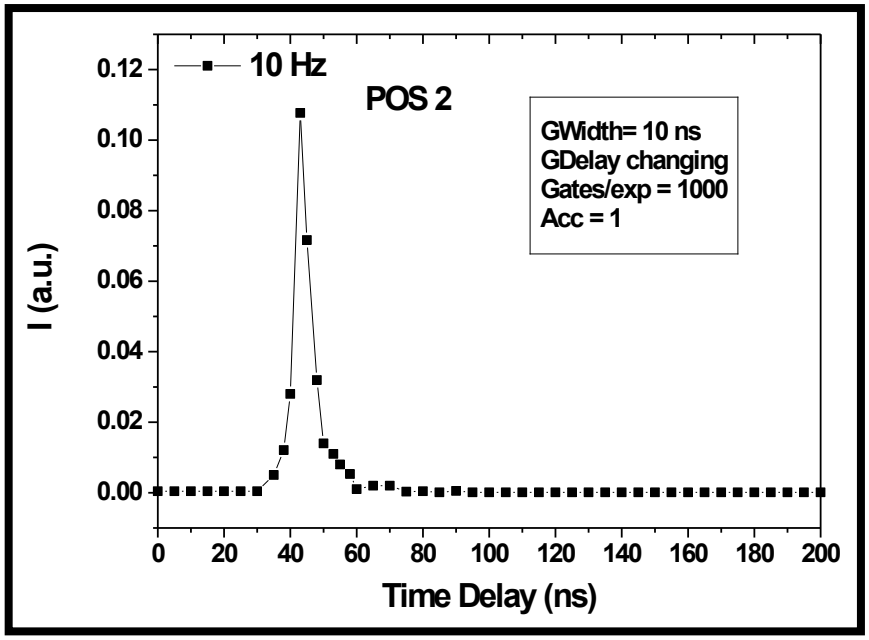

Figure 4-10: Time-resolved emission spectrum at position 2 as a function of time and a 10 Hz frequency.

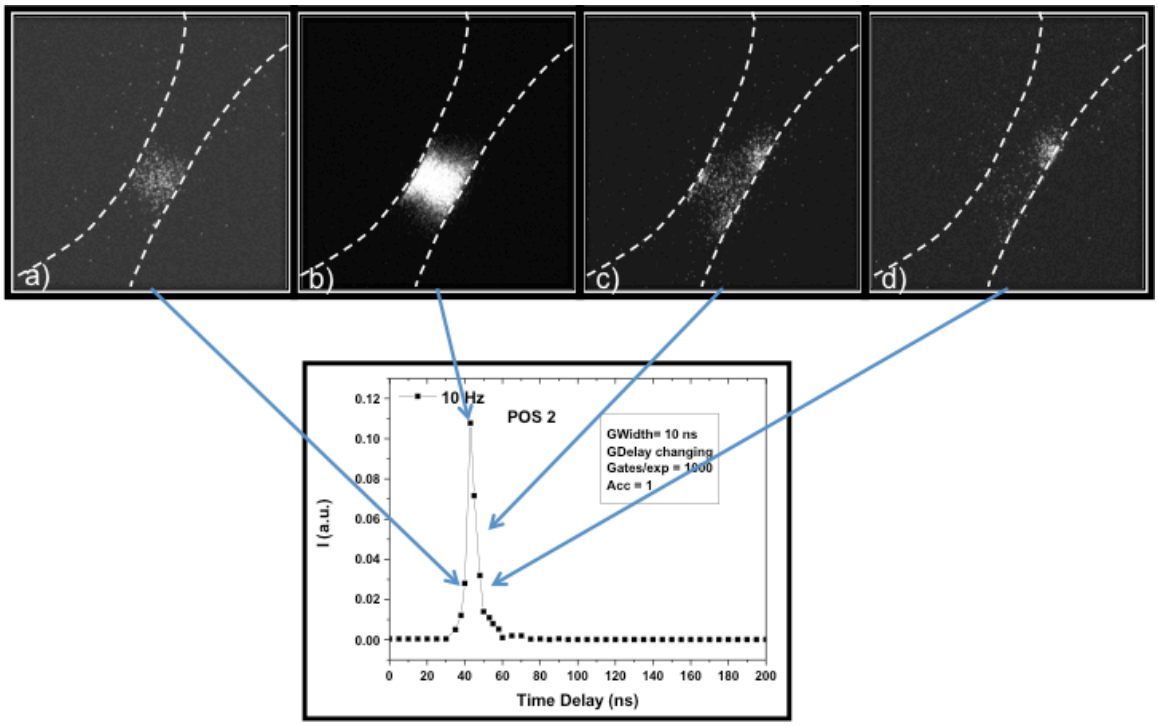

Figure 4-11: Time-resolved emission spectroscopy of 337.1 nm band at position 2 with a 10 Hz frequency.

The final position of interest was that of position 3. This region is important because the discharge forms and propagates here almost simultaneously with the breakdown at the pin electrode due to the local spacing causing a very high, localized electric field enhancement. This high field enhancement also leads to a very intense 337.1 nm emission as shown in Figure 4-12. Also attributed to the high electric field enhancement is the time of emission of the spectrum as it occurs at approximately the same time in which the discharge at position one is observed. The intensity here is seen to be nearly 2x as high as at position one and this is due to the location near the electrode whereas at location 1 it is between the first pair of dielectrics.

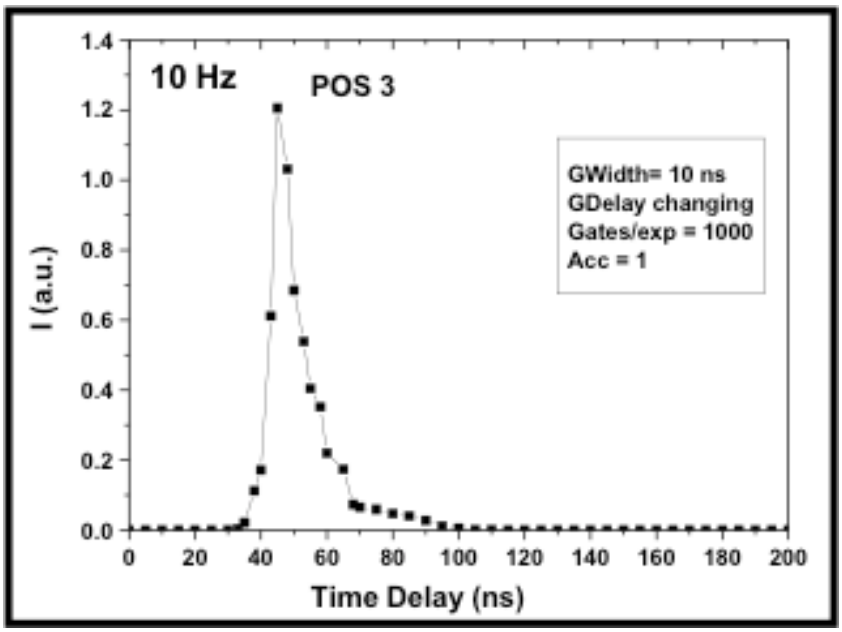

Figure 4-12: Emission spectrum as a function of time at position 3 for a 10 Hz discharge.

The tail end of the spectrum in the 337 nm emission is distorted at later times, giving rise to an extended shoulder at later times. Again, this may likely be due to sheath collapse processes. This data is also compared to the fast camera as shown in Figure 4-13. Multiple microdischarges are apparent at this electrode. Again, the image correlates very well as expected with the time resolved emission spectra. In this case, the emission appears to be associated with the formation of surface discharges.

The observation of plasma formation at location 3 in early time steps may be correlated to a process known as the triple point multiplication. The triple point is known as the region of high electric field enhancement between a dielectric material and an electrode.[58] In this setup, the triple point region is located between the planar electrode and the two dielectrics nearest it. This localized enhancement when reaching such a high magnitude can lead to electron field emissions. This field emission has the potential to generate an avalanche and may be attributed to the extended shoulder of optical emission seen within this region as well as intense filamentary microdischarges in early time steps of Chapter III.

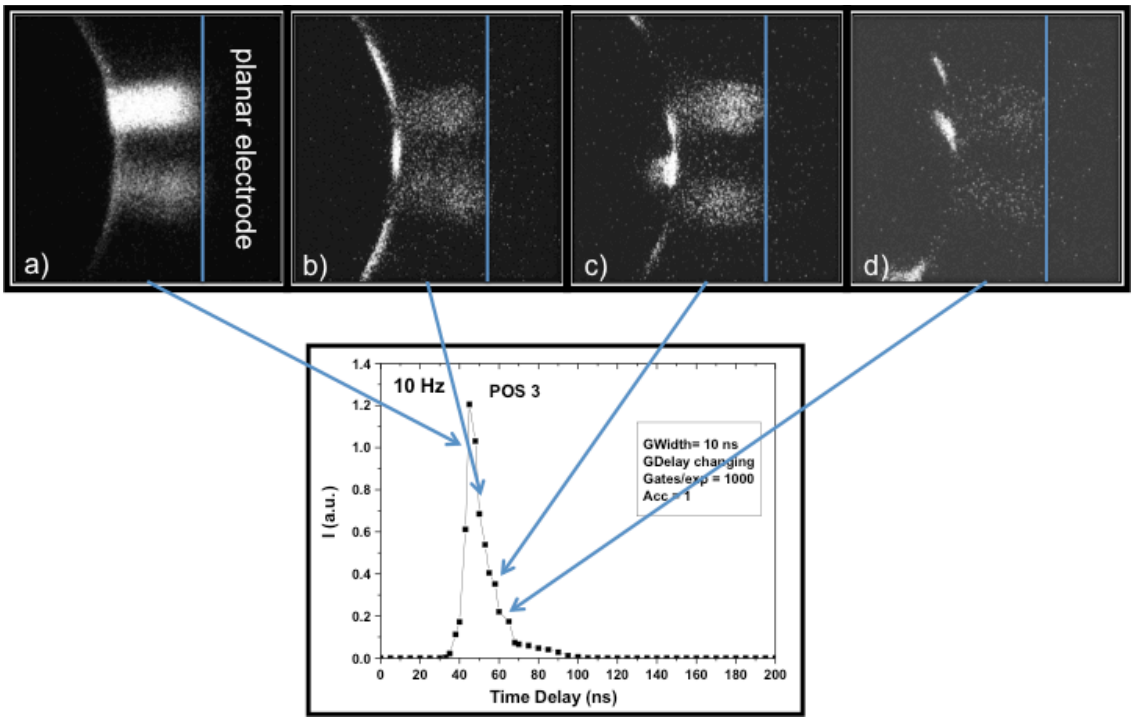

Figure 4-13: Time-resolved emission images correlated to the obtained emission spectra for position 3 within the 2-dimensional, zirconia packed bed reactor.

The results collected from this study have shown the generation of the second positive band nitrogen species as a function of position, frequency, and a function of time for the duration of the pulse width. Figure 4-14 is a representation of each of the various positions with a normalized intensity (b) and an un-normalized intensity (a). One can see that the higher localized electric field at position 3 has a much greater effect on the second nitrogen intensity when looking at the intensities in (a). This suggests that a higher packing fraction would result in a higher second positive nitrogen band population and therefore would allow greater control of the reactive species within the packed bed reactor. The results presented here show how the excitation and species production differs depending on relative location within the packed bed. Therefore it is important to take into consideration the residence time of the gas entering such a system to ensure the desired plasma interaction. Additionally the results show that frequency is an important consideration. The size of the reactor, frequency of the discharge, and residence time of

the gas need to be considered for optimization of an applied packed bed dielectric barrier discharge reactor.

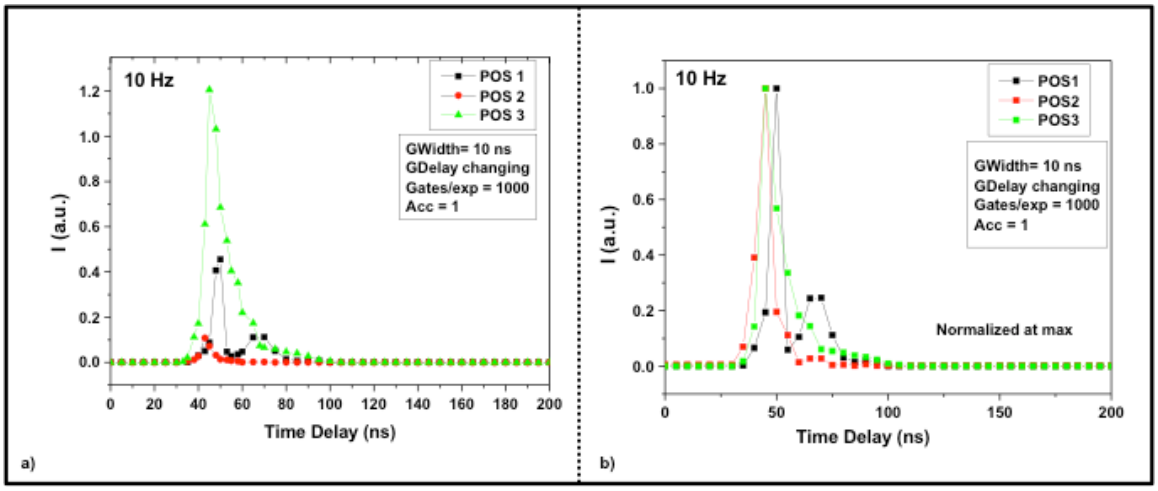

Figure 4-14: Total emission spectrum at each of the positions in (a) vs. the normalized intensity positions and time-resolved densities in (b).

4.3 A Spectroscopic Study of the organic discharge

It was of particular interest to determine the nature of plasma induced emission from organic aggregate. In particular, it was of interest to see if the plasma interaction induced desorption of the evolution of volatile species in the gas phase. The presence of such species gives insight into the nature of the plasma organic aggregate interaction and possible damage effects. In this study soybean seeds were placed at the same locations as the inorganic material with the same pulse width, voltage, and frequency of the power supply.

First investigation into the seed aggregate was at location 1 as shown in Figure 4-15. Upon inspection of the spectra when compared to Figure 4-5, one can see that the average intensity of spectra captured was much lower for the seed aggregate. This is most likely due to the field enhancement of the zirconia discs owing to its higher dielectric constant relative to the seeds. Typical seed dielectric constant is approximately 12. Reduced intensity may also be due to moisture and the formation of attaching gases

associated with plasma surface interactions such as heating. An example of the spectrum taken at location one is shown in Figure 0-17 with peaks showing at the 337.1 nm N_2 band, and some N_2^+ emission lines as well.

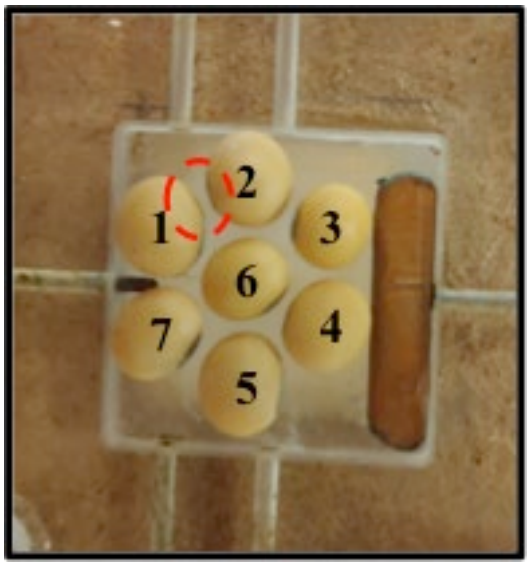

Figure 4-15: Top-down view of the seed aggregate in the 2-d cell with location 1 for optical emission spectroscopy encircled.

When investigating the time of plasma formation and propagation at location 1 with the time resolved spectroscopy, the first appearance of a signal is on the same order of time as the inorganic material of ≈ 50 ns after the pulse initiation and is shown in Figure 4-16. The variation in time of the 337.1 nm emission line is also very similar to that of the inorganic material with a sharp increase and decrease in emission intensity. One thing of note that was not observed at location 1 with the organic media is the absence of the second emission peak.

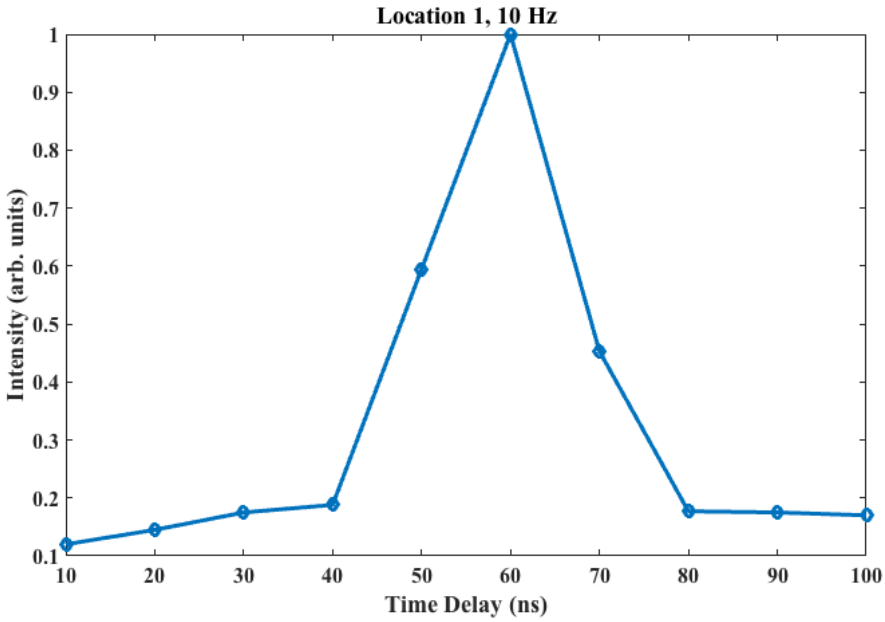

Figure 4-16: Time-resolved emission spectrum for the 337 nm band at location one for the seed material with a pulse rate of 10 Hz.

One reason for this is that the emission intensity of the second peak is a tenth of the initial peak and therefore may not be distinguishable from background with the utilized setup. Another reason is likely electron sequestering by the substrate. The surface may be sufficiently lossy that after collapse, charge is removed by surfaces or electronegative gases or moisture evolved from the seeds. This would also tend to arrest any restrike processes. The fully observed emission spectrum is shown in Figure 0-17.

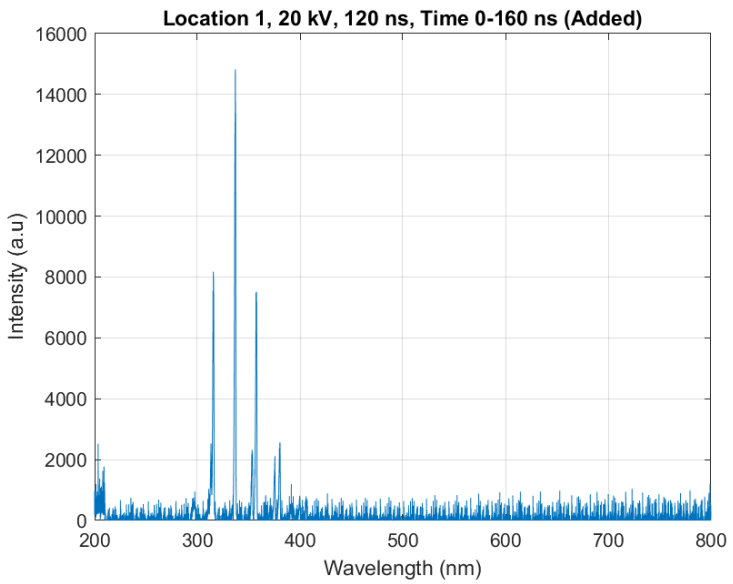

Figure 0-17: Optical emission spectrum of the soybean seed taken at location one.

In order to glean additional insight into the mechanisms occurring with the organic material, location 3 was selected for observation. Location 3 is shown in Figure 4-18. A region near the planar electrode is important as it hold different electric field enhancement effects than a seed surrounded by additional dielectric aggregate.

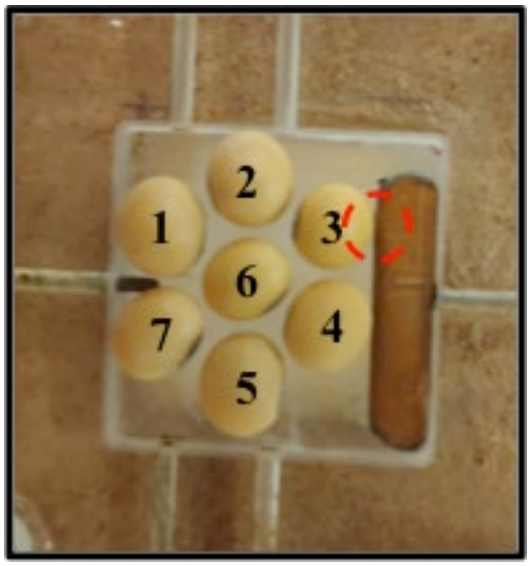

Figure 4-18: Image with Location 3 of the OES investigations for the organic aggregate.

Additionally, the plasma at this location tended to form intense filamentary micro-discharge with the nearest seed and therefore lead to additional observed species from outgassing or destructive surface morphology. The intensities recorded at location 3 when compared to location 1 were an order of magnitude larger for an identical setup. This is due to the proximity of the planar electrode with the organic aggregate. Unlike the inorganic material, a double peak is not observed here either from the lower dielectric resulting in a lower intensity discharge or electron sequestering by the substrate. The observed spectrum is shown in Figure 4-19 with the intensity normalized.

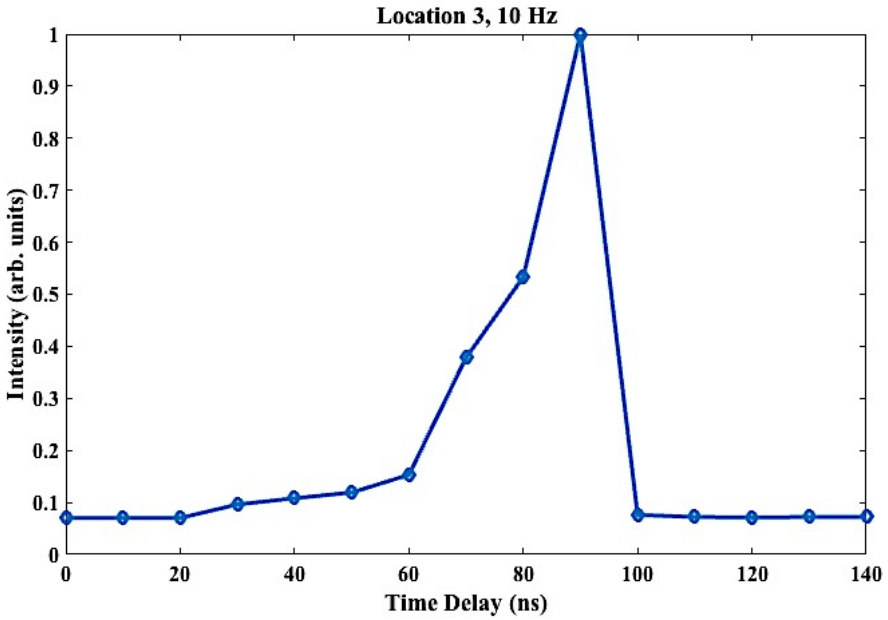

Figure 4-19: Time resolved OES spectrum of the 337 nm nitrogen band emission at location 3 for the organic soybean at a pulse repetition rate of 10 Hz.

4.4 Future Investigations Using Optical Emission Spectroscopy

Optical emission spectroscopy of the 2-dimensional system allowed for an understanding of the plasma produced species as a function of time and location. It was shown that the emission intensity increases and then decreases as the plasma propagates through the aggregate. For the inorganic aggregate, a double peak was observed from the sheath collapse and reforming. The same phenomenon was not observed with the organic

material. The unobservable second peak with the seed aggregate may be due to a lower intensity discharge and electron sequestering from plasma material interactions. The work presented here only touches the surface on the understanding of the species emitted within packed bed reactor systems. Similar studies may be performed looking at the effects of the packing fraction and higher dielectric constant material to name a few. Further work may be performed to understand the double peak observed in the inorganic material and why this is not observed in the organic discharge. This would include a higher power discharge or modifications to the spectrometer system.

Chapter V

Atmospheric Nanosecond Pulsed Discharge Effects on Soybeans: Propagation Methods and Water Uptake

5.1 Introduction to previous work with contact angle and water absorption

Dielectric barrier discharge packed bed reactors are currently being investigated for applications ranging from ozone generation and dry reforming of methane, to volatile organic chemical (VOC) composition.[59,60,61,62,63,64] The packing dielectric is a physical obstruction to the development of a spark or arc. Rather under the application of a time varying voltage, the discharge manifests itself as a combination of surface and micro-discharges. The surface area presented by the packing dielectric along with the presence of the plasma and high electric field in interstitial spacing makes the geometry ideal for non-equilibrium chemical processing.

As the world population continues to grow, food production will need to be resilient and sustainable particularly against pressures such as climate change and crop pathogens. The ability to provide nutrients to plants for deep space travel is also important for eventual human settlements off world. In order to attain enough nourishment for future generations and deep space, novel approaches will need to be investigated.[65] Therefore, the focus of this work is to investigate the effect of the plasma interaction with edible, organic material such as *Glycine max*, commonly known as the

soybean. Here in this case, the packing dielectric is the soybean itself. Research from various groups around the world have shown that plasma treatment of seeds before planting may influence germination rates, secondary root development, shoot growth, and even yield.[66,67,68,69,70,71] In some studies, evidence has been presented which shows that these traits can be related to a mechanical effect on the seed coat such as surface scarification allowing for increased rates of imbibition or plasma-induced changes in plant metabolism.[72] Understanding and utilizing the biological response of soybeans to plasma exposure may pave the way for engineering benefits such as increased yield, elongated growing season, more resistant crops, or for less use of additional fertilizers.

Plasma discharges in air generate reactive species that can chemically react with organic media and thus affect physiological processes in living systems. Such interactions can effect both the thickness and porosity of seed coats. Generally, a thicker seed coat leads to less permeability and therefore less water absorption. Soybeans normally have a relatively thin, permeable coat.[14, 73] Nooden et al., has shown that mechanical modification to seed surfaces such as sanding can lead to higher water uptake and increased germination rates. Not only are surface modifications of the seed coat important, but the induced biological response of the seed to reactive oxygen species (ROS) should also be investigated. It is known that ROS are formed in aerobic species including both plant cells and animal's cells as a result of cellular metabolism, with mitochondrial activity being a major contributing source.[74] ROS can an act as intracellular and extracellular signaling molecules and play a role in a number of cellular signaling events that include apoptosis, gene expression, and activation of signaling cascades.[74] Such ROS may also influence plant growth and development.[75] The

presence of hydrogen peroxide (H_2O_2), and O_2^-, act as signaling molecules, which regulate cell death[76,77] root gravitropism[78], somatic embryogenesis[79], and plant defense.[80] For instance, when applying cold plasma treatment on soybeans, Ling et al. saw an increase in germination, vigor, growth, shoot length, and root dry weight.[66] In their experiment, the seeds were treated at 1 Torr pressure with an RF source operating between two plate electrodes. The power was varied from 0-120 W and treated for a duration of 15 seconds. Another group utilized various dielectric barrier discharge (DBD) reactors excited with sub-microsecond high voltage pulses (40 kV and 1 kHz).[67] They investigated the effect of direct treatment of seeds with plasma and the effect of plasma activated water (PAW) on seed metabolism of radish, tomato, and sweet pepper plants. It was found that, direct seed treatment and PAW as well as treatment using these processes in tandem had beneficial results. These findings suggested a treatment time dependence in which too short or too long exposure was observed to have negative effects relative to the control sample.

Another application of the plasma treatment of seeds is surface decontamination. The benefits of conventional antimicrobial treatments are well established.[68,69,81] Such methods include the use of calcium hypochlorite washing, heat treatment, hot water, ammonia gas, dry heat, and acetic acid. Previous work has shown that many microorganisms can also be inactivated by plasma.[82,83] Sintani, Sakudo, Burke, and McDonnel reported that the reactive species generated in plasma contribute to the antimicrobial effects of gas plasma.[84] Pradeep and colleagues had shown that microorganisms such as aerobic bacteria, molds and yeasts, Bacillus cereus, E. Coli, and Salmonella were reduced in the range of 1.2-2.2 log CFU/g upon a corona discharge

plasma jet treatment for 3 minutes.[68] Filatova et al., investigated germination and suppression of fungal and bacterial pathogens using a 5.28 MHz capacitively-coupled radio frequency discharge at 0.3-0.7 Torr.[69] Not only did the study conclude that plasma treatment increases the quality, speed, and energy of germination but it also illustrated the reduction in microorganisms such as E. coli, S. aureus, and B. subtilis as a function of rf plasma treatment versus time. The population of microorganisms surviving tended to decline by over 50% for E. coli and B. subtilis within the first 5 minutes of treatment with all populations exhibiting a near 0% survivability for 10 minutes of treatment.

5.2 Description of the experiment

In this work, seeds were plasma treated using two different reactors. A 2-dimensional array of seeds was treated in a 2-D reactor shown in Figure 5-1. The apparatus utilized an in-plane pin-to-planar electrode configuration that was sandwiched between two quartz plates. The seeds were placed in the inter-electrode gap. This apparatus allowed for visual time resolution of discharge propagation through the array of seed aggregate. A pulse delay generator was employed for timing of the fast camera with the high voltage pulser such that images may be captured at various time-steps during the pulse duration. Time-resolved imaging of discharge evolution featuring inorganic material in the same apparatus has been described in detail elsewhere and excluded for brevity.[85] The reader is referred to this text for the detailed process and equipment utilized.

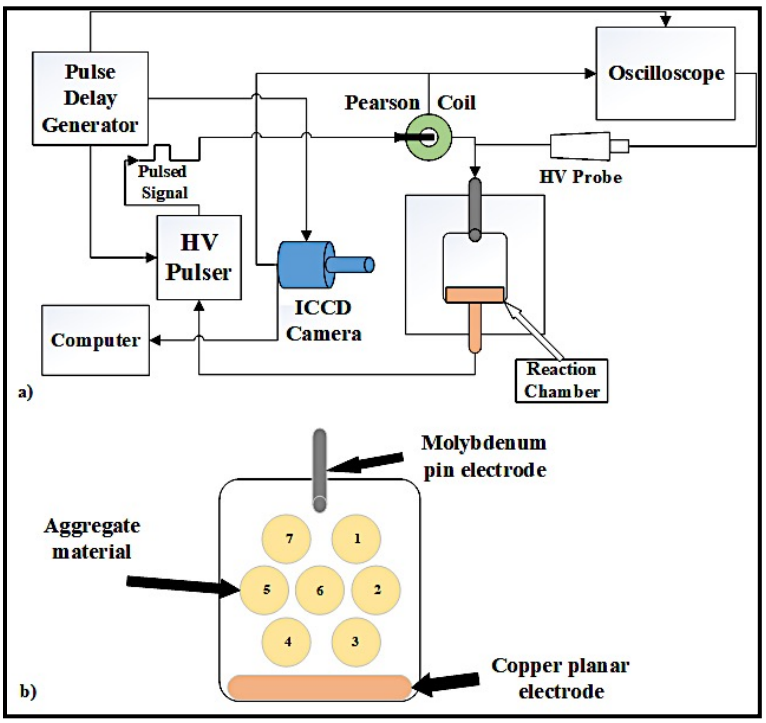

Figure 5-1: The two-dimensional experimental setup that allows for time-resolved imaging of the micro-discharge between the inorganic and organic material.

The same methodology used in that work is implemented here in order to study micro-discharge interactions with organic material. A nanosecond voltage pulse was used in this experiment so that electroporation effects can be ignored. Electroporation occurs over long voltage pulse durations of microseconds and milliseconds for micro- and macro-molecules, respectively.[86] Electroporation opens the membranes of the seed coat in a multi-step process. First, charging and polarization of the cell membrane occur followed by temporal destabilization and pore creation. Then expansion of the pore radii occurs followed by the resealing of the pores and possible memory effects.[86]

A schematic of the three-dimensional experimental apparatus used in this work is shown in Figure 5-2. The plasma is sustained between two electrodes in a coaxial electrode arrangement with a central, stainless steel rod electrode and an outer copper mesh electrode. The copper mesh was placed on the outside of the quartz tube, which had a 1.7 cm inner diameter with a wall thickness of 2 mm and was 12 cm in length.

The ends of the quartz tube were terminated with a end port plug which allowed for electrical isolation of the electrodes and gas flow. Packing fraction of the seeds within the reactor was taken to be nearly constant owing to the presence of the 3D printed end plugs that ensured full utilization of the treatment volume without dead spaces on either end of the organic aggregate. One end of the apparatus was connected to a mass flow controller, which regulated the flow of input argon gas. The soybeans used in this experiment were Asgrow 3-4 roundup dicamba.

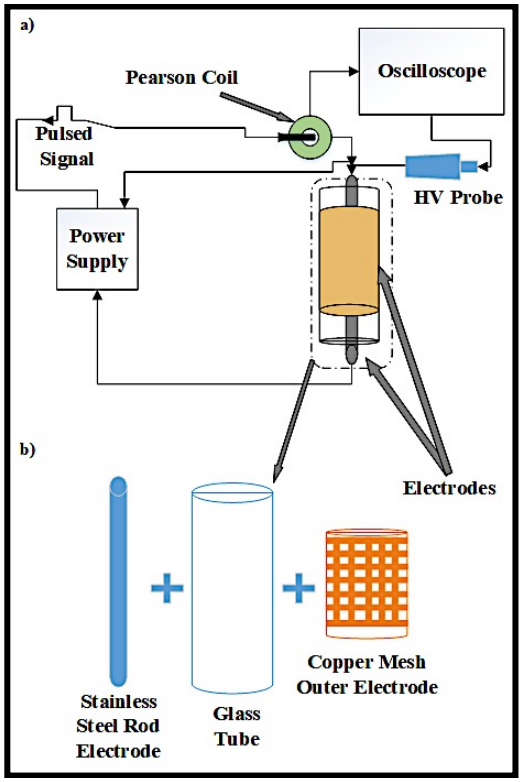

Figure 5-2: 3-dimensional setup showing the coaxial dielectric barrier discharge reactor without the packing aggregate.

The experiment utilized Eagle Harbor Technologies Nanosecond Pulser-120 (EHT NSP-120) for plasma generation with two Tektronix P6015A high voltage probes for voltage measurements, a Model 6585 Pearson Coil to measure current, and a Tekronix 3024 oscilloscope to collect waveforms. The effect of gas type on the plasma treatments was assessed by metering flow into the apparatus using a MKS Mass Flow Controller which had a maximum flow rate of 500 standard cubic centimeters per minute

(sccm). Contact angle images were collected using an Edmund Optics EO-5012M monochrome USB camera with an AmScope FMA050 adapter for a 4x magnification. Water absorption was assessed using mass measurements (before and after seed soaking using a Mettler H80 scale.

The rod electrode of the packed bed reactor was biased to a positive (+) voltage with the copper mesh acting as the negative (-) electrode of the floating supply. The voltage, frequency, pulse width, and duration of the various trials were tabulated in Table 5-1. Trials were based on the total mass of the seeds in order to eliminate the differences that arise from the variation or spread in mass of the seed. The mass of each trial group was recorded pre- and post-treatment to determine any mass loss during the treatment. The numerical average mass lost was different for each trial set as shown in Table 5-1.

Table 5-1: Organized seed treatment parameters such as voltage, frequency, duration, and pulse width as well as the average mass loss per treatment.

Treatment	Voltage (kV)	Frequency (kHz)	Duration	Pulse Width	Total Mass Loss (g)
T1	18	3	30 s	60 ns	Air – 0.02 Argon – 0.07
T2	14	2	3 min.	60 ns	Air – 0.1 Argon – 1.03
T3	12	2	10 min.	60 ns	Air – 0.36 Argon – 1.05

The mass chosen for the all treatments and measurements was 53 ± 0.15 grams, which consisted of approximately 300 seeds. Experiments were based upon total mass of the soybeans in order to prevent any geometrical effects seen by choosing a set number of seeds. Therefore, each treatment study involved a set mass, which is based on the density of soybeans, ignoring the various size and textures of the seed. Seeds chosen for the control group had a single recorded mass number as opposed to a pre- and post-treatment mass. In the instances of longer treatment times, condensation was observed on the inner

surface of the reactor walls. The moisture is believed to be associated with thermal desorption associated with localized plasma heating. A simple test was performed to determine the temperature of the reactor during longer treatment times (i.e. greater than 3 minutes) in which the reactor operated for the duration of an hour. At the end of this period, the reactor could be handled without any protective equipment and was found to have a temperature of 32 degrees Celsius using a HH12A Omega thermocouple. The reason for not observing moderate heating is due to the short duration of nanosecond pulsed discharges that prevent significant heating effects.

For plasma activation of the tap water, an underwater atmospheric pressure plasma jet was utilized.[87,88] Compressed air passed through the jet at a rate of 30 SLM. The plasma jet was submerged in 350 mL of tap water and allowed to operate for 5 minutes at various voltages, frequencies, and pulse widths. No macroscopic heating of the water was observed during the treatment. pH and conductivity measurements of the treated water were made using a ThermoScientific Orion Star A Series portable meter. Nitrate/Nitrite measurements were made using an ion chromatograph and the peroxide levels were made with WaterWorks peroxide check strips.

Contact angle measurements are based upon the procedure put forth by Yuan and Lee.[89] A 2.5 μL droplet of water was placed upon the seed coat and the angle of contact with the surface of the seed was measured on each side of the seed. The angles were averaged in order to obtain a contact angle. Images were taken at 1-minute intervals for 15 minutes. Images were taken at ascending time steps in order to view the rate of absorption of the water into the seed.

The water absorption measurements were made at time intervals of 1 hour, 2 hours, and 3 hours. The seeds were separated from the water and lightly handled with a cloth to remove any residual water droplets. The mass of the soaked seeds was then recorded next to the pre-soak mass.

In general, the discharge propagates through dielectric aggregate in the form of localized microdischarges and surface ionization waves. Of particular interest is the nature of surface modification exacted on the seed due to the presence of these very different discharge modes. Following general water absorption and contact angle measurements, an experiment was conducted in order to determine which plasma discharge mode had the most effect on water absorption. The various locations of surface and microdischarges occurrence were marked to determine the effect if any on surface conditions. A 1.0μL droplet of water was placed at the marked locations of interest. A reduced volume water drop was used for contact angle measurements in this case in order to ensure positioning in the effected area of interest.

5.3 Inorganic vs. Organic Micro-discharges: 2-Dimensional Cell

Seeds were arranged in the 2-D apparatus in a hexagonal array similar to that studied previously with inorganic dielectric media.[85] However, precise orientation of each soybean varied from position to position owing to variations in seed size and shape. Single as well as accumulated images (100) were acquired with a 5 nanosecond exposure. An Andor iStar334 iCCD camera with a 2.4x magnification connected to a pulse delay generator allowed for time-resolved imaging of the discharge.

Of particular interest is how the discharge propagates through organic media in comparison with inorganic dielectrics. Biological material in general such as seeds surfaces are highly textured and can be a source of desorption gases, which can locally modify the discharge as well as the composition of the local discharge. In previous work, with hexagonal packing of inorganic material, the discharge tended to propagate through the media as an ionization wave consisting of a spatially and temporally alternating propagation mode in which micro-discharges formed between media, which in turn gave way to surface charge deposition resulting in the formation of surface discharges along the surface media in the general direction of the applied electric field. This propagation phenomenon was studied as a function of the pressure and dielectric constant, showing the discharge to be localized and consistently filamentary micro-discharges (FMs) at gaps of shortest separation between dielectric disks.

Figure 5-3 (a) is a close-up view (2.4x magnification) of the 2-dimensional representation of the packed bed reactor and (b) is a macroscopic view of the same discharge but of the entire system. The disks are labeled 1-7 for ease of discussion as can be seen in the macroscopic image view and are labeled in a similar manner for the soybean setup. Settings for the inorganic material were single pulses of 120 nanosecond pulse widths with voltages at 20, 14, and 12 kV. Images represented here only include results from the 20 kV data set for brevity.

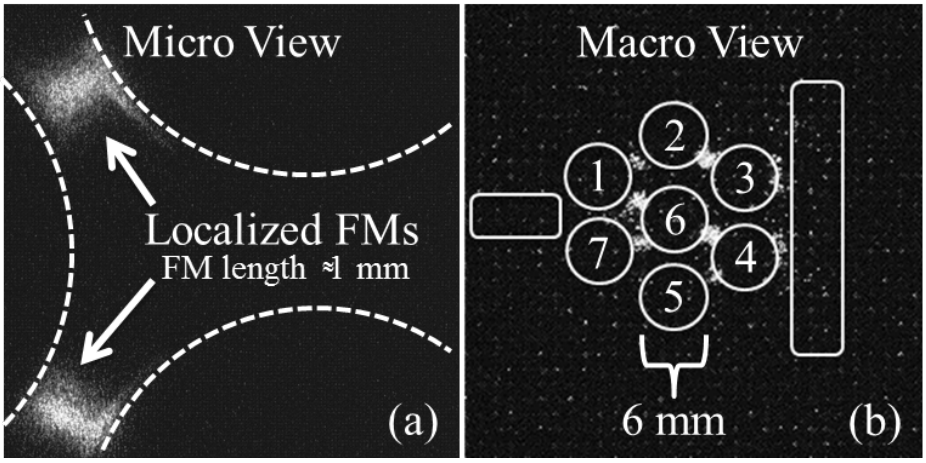

Figure 5-3: (a) is a close-up of FM between the disks of inorganic aggregate. (b) is a macroscopic view of the discharge throughout the inorganic aggregate at atmospheric pressure; showing that the FMs are localized in the interstitial spaces between disks.

Discharge image data for the organic material was obtained using the same procedure as used with the inorganic material for direct comparison. Figure 5-4 represents a microscopic view of the organic aggregate discharge with a monochrome image capture. Images (a) and (b) of the figure are taken at the same time step but one can see that there is significant pulse-to-pulse variation. For instance, in (a) a more intense FM can be seen in the top-left corner of the discharge but in b) the discharge appears to be more diffuse.

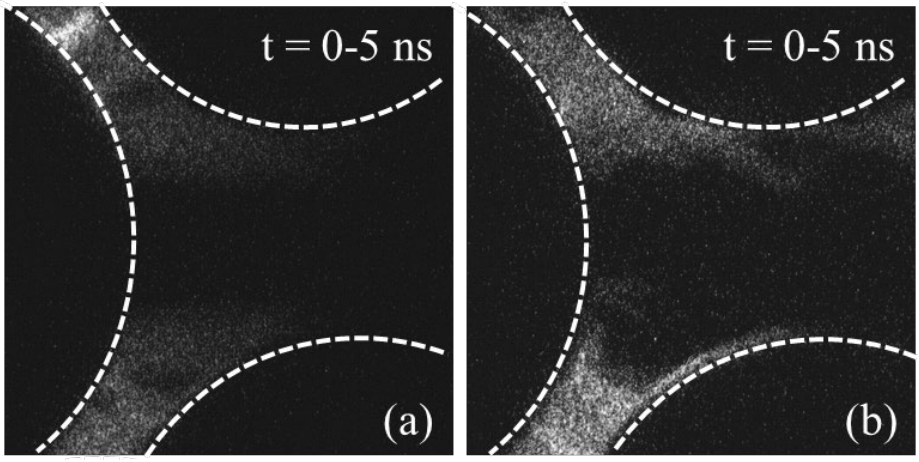

Figure 5-4: Two, 5 ns exposure images of a 20 kV, 120 ns pulse through the soybean aggregate taken at the same time step to show variation in pulse to pulse discharge paths versus the consistency of inorganic material.

A number of possible mechanisms could contribute to the shot-to-shot variation including surface etching, desorption of gases such as water vapor, modification to seed surface texture/protrusions, and spatial variations in surface conductivity. In order to gain better insight into the degree of the shot-to-shot variation, acquisitions including 100 overlaid shots were acquired. Figure 5-5(a) shows the significant contrast between inorganic dielectric media and the seeds. Figure 5-5(a) is a representation of 100 accumulated images involving inorganic media (zirconia disks in this case) and Figure 5-5 (b) shows 100 accumulated images of discharge with the organic media. One can see that the spatial occurrence of discharges in the organic material varies significantly from pulse-to-pulse.

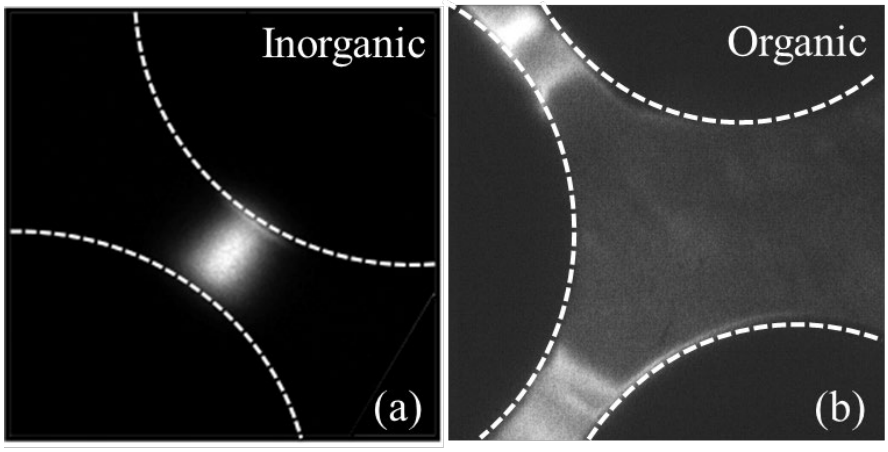

Figure 5-5: 100 Accumulated images with each accumulation having a 5 ns exposure. (a) Shows micro-discharge location with inorganic material verses (b) the stochastic nature of organic material. The contrast between the (a) and (b) with that of the background shows the consistency of the location of the FMs with the inorganic FMs being much more localized than the organic aggregate FMs.

The micro-discharges, while still localized, tend to attach over a larger area. This may be a desirable attribute as it suggests that at least the plasma-induced surface modification of the seed is associated with a larger treatment footprint and perhaps the stochastic nature of where the micro-discharge occurs may give rise to more of the seed surface being treated directly. The seemingly random attachment points suggest that the organic aggregate surface is being modified in some way. The reactive species and

energetic particles colliding with the aggregate are interacting with the organic material, causing the discharge location to vary up to a few hundred micrometers. Figure 5-5 (a) with the inorganic material shows a consistent FM discharge region and not the significantly larger region in Figure 5-5 (b). Again, some of these modifications could be due to surface etching of the seed coat or outgassing of the seed. Other possible explanations include biochemical changes as a result of the reactive oxygen and nitrogen species interaction with seed coat cells. A more conclusive understanding of nature of discharge evolution with the soybean aggregate is left for future work.

The energy per pulse of the discharge was on the order of 3 mJ and this was determined by the analysis of the captured voltage-current waveform. The resulting energy deposited per pulse suggests that the surface of the seed is being modified in some way. The energy per pulse is not enough for the vaporization of water but very localized heating has the ability to remove some moisture from the seed coat. Most likely, however, is the pulse-to-pulse variations are due to the 3 mJ of energy being deposited and absorbed by the molecular bonds of the seed coat. This in turn changes the orientation of the bonds as well as possible generating new radicle attachment sites. A slight shift in surface bond energy from 13.6 eV to 13.2 eV of a radish seed was observed based upon sub-atmospheric plasma treatment of 80 W at 5 minutes. This changed the bond from a C-O to a C-C. This slight modification locally changes the plasma interaction with the surface and may attribute to the pulse-to-pulse observed variations with the soybean aggregate as well.

Plasma propagation through the 2-dimensional setup with organic aggregate is shown in Figure 5-6 via a macroscopic image capture with the iCCD camera. The first image is a reference image showing the placement of the seeds within the cell. Seed were chosen based upon their size in order to obtain uniformity although there are some slight differences in seed shape. The following images (b), (c), and (d) show the plasma formation at the pin electrode with FMs followed by SIWs across the nearest seeds. Figure 6(d) shows a later time-step in which FMs have begun forming from the center seeds towards those nearest the planar electrode, much like that with the inorganic aggregate.

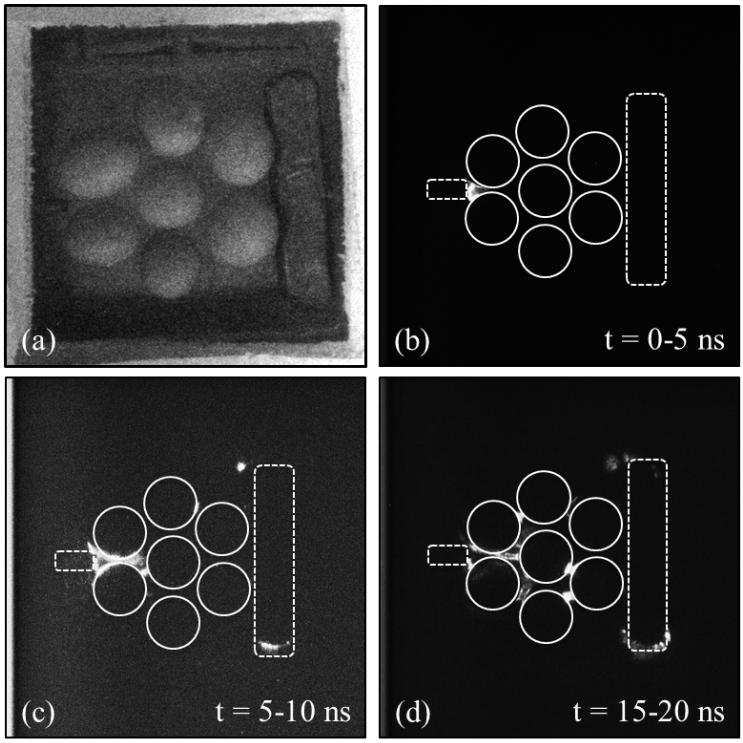

Figure 5-6: (a) Reference image of the seeds and electrodes configurations in the 2-D cell. (b-d) accumulated, 5 ns exposure images of the plasma formation and propagation through the organic aggregate with a wide angle lens. This figure shows the dominating propagation method and is similar to that found in the inorganic discharge images.

The importance of Figure 5-6 is that the time-resolved system-wide images are similar to those taken with the inorganic material, suggesting that the macroscopic plasma propagation properties mimic the inorganic discharge mechanisms. A direct

comparison between the inorganic and organic aggregate with the wide lens is shown in Figure 5-7.

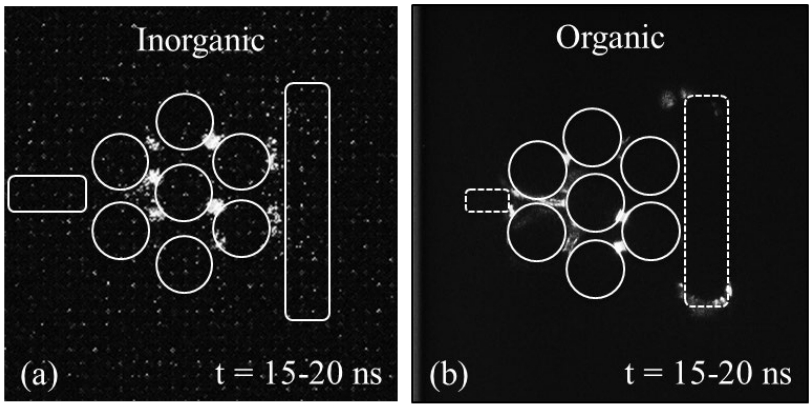

Figure 5-7: Direct comparison of the difference in wide lens exposure capture with (a) inorganic aggregate and (b) organic aggregate. Emphasizes the importance of similar macroscopic discharge modes between the inorganic and organic aggregate.

Qualitatively, the discharges look similar for the two cases on the macroscopic scale. However, in each case, the intensity of FMs appears to scale with dielectric enhancement. Here, zirconia $\varepsilon/\varepsilon_0$ = 26.6 and for the soybeans $\varepsilon/\varepsilon_0 \approx 12$.[90] Owing to contrast and intensity scaling, the wide lens images are more sensitive to FM mode but surface waves are indeed present.[85,91] What is not so clear is the determination of which discharge mode (FM or SIW) modifies seed physical properties such as seed coat porosity and seed water absorption capacity (imbibition), metabolic properties, and germination rates the most?

5.4 Contact angle as a function of treatment parameters

Plasma interaction with organic substrates in particular can greatly affect the surface energy. This is exploited for a variety of applications with the treatment of polymers with reactive air plasma. The degree to which the surface is modified is typically characterized through the measurement of the surface contact angle.[92,93] Surface modification of the seeds was also assessed using contact angle measurement. Data used to calculate seed contact angle changes were acquired by imaging droplets on the surface

of a seed with a microscope. Images were taken with a microscope camera at 1-minute intervals up to 15 minutes in order to determine whether the treated seeds had become more hydrophilic or hydrophobic after treatment (see Figure 5-8). The measurements made for contact angle was produced from an average from a triplicate data set.

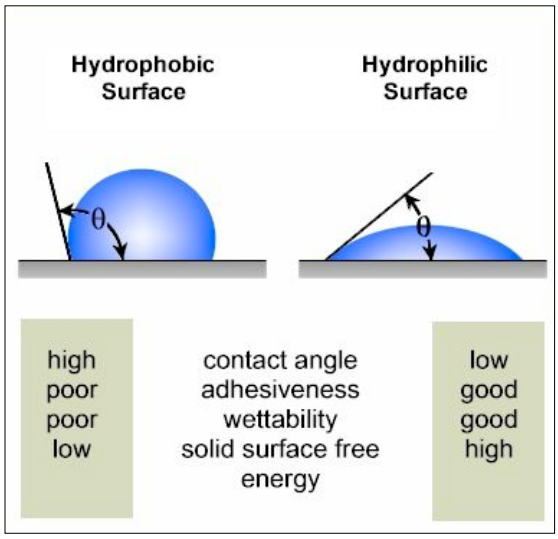

Figure 5-8: This image taken from Rame-Hart Instruments Co. presents the differences in contact angles of hydrophobic versus hydrophilic surfaces as well as lists physical properties represented by each contact angle.

Three treated seeds were taken from each treatment and angles were recorded on each side of the seed and then averaged. Figure 5-8 is an excellent example of how contact angles are measured on a flat surface. The measured angles of the treated seeds and those wetted with PAW were then compared to the control group of non-treated seeds with only tap water as the droplet. The contact angle of the PAW water was investigated because of its acidic properties, which can etch polymeric surfaces. An example of a water droplet on the seed surface is shown in Figure 5-9.

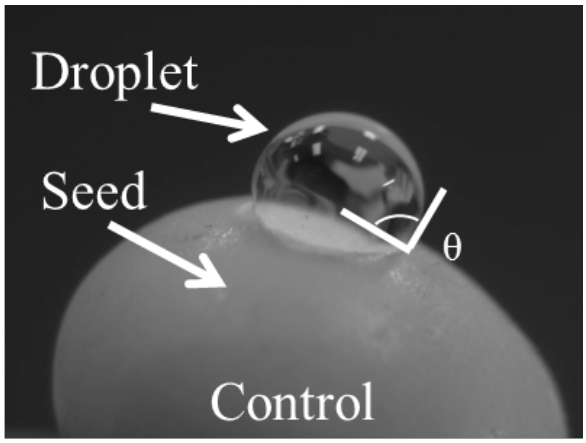

Figure 5-9: Example of the contact angle measurement made with a droplet of tap water on an untreated soybean seed acting as the control. This image has a 2.5 microLiter droplet for emphasis. Actual measurements were made using a 1.0 microLiter water droplet.

The figure shows a 2.5 µL pipette delivered droplet of water on the surface of an untreated seed with the angle of interest overlaid on the image. The water droplet was decreased in size from 2.5 µL to 1.0 µL for improved contact angle accuracy. In order to take into account any possible curvature effects of the droplet on the rounded surface, measurements were based upon the average of the contact angles taken from each side of the visible water droplet. The water used in this experiment was fully characterized beforehand. Droplet water properties such as pH, conductivity, nitrate and nitrite levels, and peroxide levels are presented in Table 5-2.

Table 5-2: Organized PAW treatment parameters including voltage, frequency, and pulse width with their measured water properties. The table shows the influence of plasma interaction with water causing changes in water properties.

Treatment	Voltage (kV)	Freq. (kHz)	Pulse Width	pH	Conductivity (µS/cm)	H_2O_2 (ppm)	NO_2^- (ppm)	NO_3^- (ppm)
PAW1	20	1.5	220 ns	7.22	785.4	10< x <25	10	50 < x < 100
PAW2	20	1.5	110 ns	7.47	799.7	5< x <10	10-20	100
PAW3	20	3	260 ns	7.48	777.1	2	20	50
Control	N/A	N/A	N/A	9.08	737.6	X < 0.5	< 10	< 10

Analysis of the collected data suggested that argon feedstock gas plasma treatment led to a significant change in the contact angle of the water droplet on the seed

surface. Figure 5-10 is a plot of the measured contact angle as a function of time from 1-10 minutes. Data was collected for each of the treatment parameters that have been outlined before in Table 5-1. As one can see, the argon gas treated sets labeled with "Ar" had significantly lower starting contact angles than those not treated using an argon feedstock gas. Angles less than 20 degrees, however, have high uncertainty in numerical value of the angle due to difficulty in measuring the small angle difference between the water droplet and the curved surface of the seed. In general, argon treated seeds tended to result in the largest changes in contact angle. The reason for this is not clear. Argon plasma can be expected to have a higher plasma density.

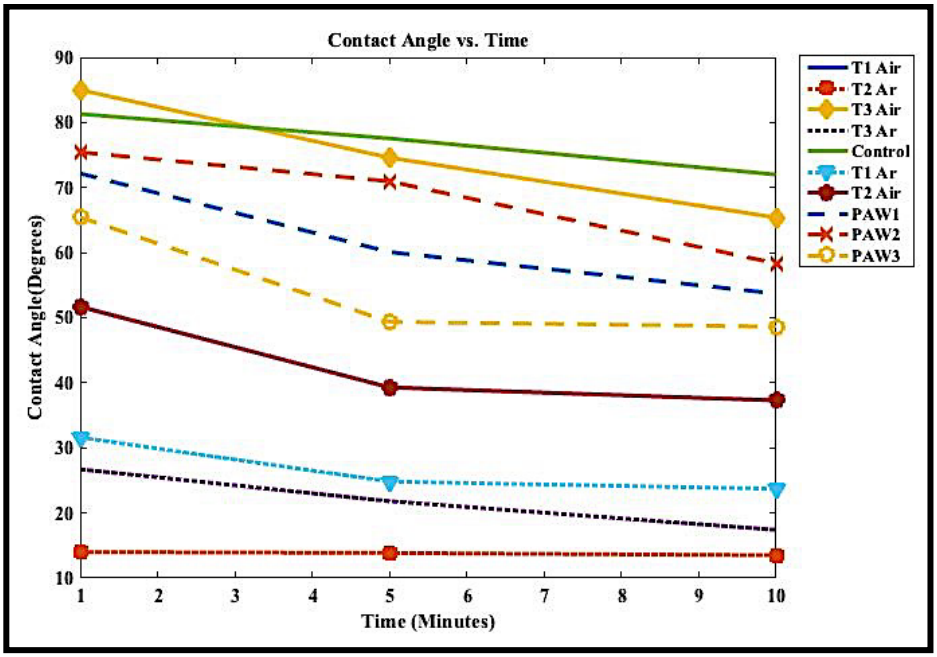

Figure 5-10: Recorded data for the contact angle measurements. 'Ar' corresponds to the treatments using an argon feedstock gas and air utilizing compressed air as the gas. Overall the argon treatments led to a much lower contact angle than the air treatments.

The UV light produced in an argon plasma compared to an air plasmas is different so the nature of UV driven surface modification such a surface bond breaking would be different as well. The argon-air mixture in this case may translate to a higher population

of reactive oxygen species. Excited argon can also disassociate and ionize nitrogen molecules, which can lead to the formation of reactive nitrogen species.

Table 5-3 lists possible gas phase reactions, labeled as 'Nr,' that prevail in argon air plasmas.[94] A more thorough list may be found in reference 36 detailing kinetic modeling of an argon plasma jet in humid air as well as references for kinetics on each reaction.

The resulting contact angle differences between the different plasma treatments may be associated with plasma chemistry on the substrate. Argon plasmas would tend to be more reducing that the air plasma which drives advanced oxidation of the surface which can lead to localized oxidation, mineralization and perhaps pinhole formation. Other research as suggested that argon treatment can fundamentally effect the cell wall via altered gene expressions.[95] Argon plasma in the work by Winters et al, was shown to have a greater effect on bacteria than the air plasma. Their report cites significant alteration of gene expressions that correspond to anaerobic processes as well as the argon plasma inducing more interactive responses with the cell walls. The air plasma mostly interacts with the biological organisms via advanced oxidation. The argon plasma was observed to present as the higher UV radiation dose . Due to the radiative nature of excited argon as well as an expected significant change in the observed species, argon plasma was seen to have a greater impact on the contact angle. Future work will provide greater insight as to the inner workings of this system.

Table 5-3: A table represents some of the many possible reaction mechanisms in which reactive species are produced within the argon-air mixture plasma.

Nr	Reaction name	Nr	Reaction name
1	$e^- + Ar \rightarrow Ar^* + e^-$	18	$e^- + N_2^+ \rightarrow N + N$
2	$e^- + N_2 \rightarrow 2N + e^-$	19	$e^- + NO \rightarrow e^- + N + O$
3	$e^- + Ar_2^* \rightarrow Ar_2^+ + 2\,e^-$	20	$e^- + NO \rightarrow N + O^-$
4	$e^- + O \rightarrow O + e^-$	21	$e^- + NO \rightarrow 2\,e^- + N^+ + O$
5	$e^- + O \rightarrow O+ + 2\,e^-$	22	$e^- + NO_2 \rightarrow 2\,e^- + NO^+ + O$
6	$e^- + O + O_2 \rightarrow O^- + O_2$	23	$e^- + NO_2 \rightarrow 2\,e^- + NO_2^+$
7	$e^- + O + N_2 \rightarrow O^- + N_2$	24	$e^- + NO_2 \rightarrow NO + O + e^-$
8	$e^- + O + Ar \rightarrow O^- + Ar$	25	$e^- + N_2O \rightarrow O+ + N_2 + 2\,e^-$
9	$e^- + O + H_2O \rightarrow O^- + H_2O$	26	$e^- + N_2O \rightarrow NO + N + e^-$
10	$e^- + O + H_2 \rightarrow O^- + H_2$	27	$e^- + H \rightarrow H^* + e^-$
11	$2e^- + O+ \rightarrow e^- + O$	28	$e^- + H_2 \rightarrow H_2^* + e^-$
12	$e^- + O^- \rightarrow O + 2\,e^-$	29	$e^- + H_2O^+ \rightarrow e^- + H^+ + H + O$
13	$e^- + O_2 \rightarrow O_2^+ + 2\,e^-$	30	$e^- + OH \rightarrow e^- + O + H$
14	$e^- + O_2 \rightarrow O_{2,vibx} + e^-$	31	$e^- + H_2O_2 \rightarrow OH + OH^-$
15	$e^- + O_2 \rightarrow O + O + e^-$	32	$Ar^* + O_2 \rightarrow Ar + 2O$
16	$e^- + O_3 \rightarrow O + O_2^+ + 2\,e^-$	33	$Ar^* + N_2 \rightarrow Ar + 2N$
17	$e^- + N+ \rightarrow N$	34	$N + O \rightarrow NO$

The contact angles measured from the plasma treated water were significantly different than what was seen with the directly treated seeds. For instance, the contact angle measurements for the treated seeds varied over a wide angle of degrees, 85 degrees to 11 degrees, whereas the plasma activated water contact angle differences only varied from 75 degrees to 40 degrees. The differences in the treated water were the H_2O_2 levels, slight differences in pH and conductivity, and in the nitrate/nitrite levels. Due to close similarities within the treated water groups, a significant difference in contact angle measurements was not expected and only a slight difference was seen. These higher contact angles show that under these plasma water treatment conditions, not much of a difference is can be observed between this values and the control for contact angles of a water droplet on a seed coat. The large difference between the PAW contact angle and the direct seed treatment contact angle is however expected. The reactive species and

UV as well as the charged particle interactions with the seed coat can be expected to have a much more direct impact on the permeability of the coat than slight modification of the water properties that were seen.

An investigation was also performed in order to determine which discharge mode (FMs or SIWs) influenced the contact angle of the water droplet to a greater degree. Filamentary micro-discharge locations on the seed coat were marked as well as the regions of SIW interactions. These regions of interest were then studied using contact angle measurements. The results suggest that FM treated surfaces led to greater water absorption than that of the SIW surface morphology. The measured FM contact angles on average were approximately 10 degrees less than that of the SIW region of interest (contact angle of 47 degrees verses 56 degrees). These results suggest that the FM treated surfaces are modified to a greater degree than SIW treated surfaces. There are a number of interaction differences that could account for this such as surface ion bombardment and higher reactive species dose owing to the highly localized nature of the FM. These measurements give insight into the design of treatment reactors. For example, based on these preliminary findings, it may be desirable to promote more filamentary micro-discharges than the SIWs. Further studies are required to fully assess the impact of discharge mode type on seed viability. For example, exposure time and damage considerations will have to be explored as well.

5.5 Water Absorption

5.5.1 Direct Seed Treatment

The aforementioned treatment parameters were applied to more treatment sets of seed and activated water for water absorption tests. A percent mass difference was then calculated for each trial at differing respective time intervals. The seeds for each set

under investigation were placed in identical containers for 1, 2, and 3-hour intervals with the same amount of water. Enough water was placed in the containers such that the water would not be fully absorbed in that amount of time. Figure 5-11 shows the percent mass difference of the treated seeds using the seed mass before and after soaking the seeds in water. The red 'dashed' line across the figure is the percent mass increase of the control at the end of three hours.

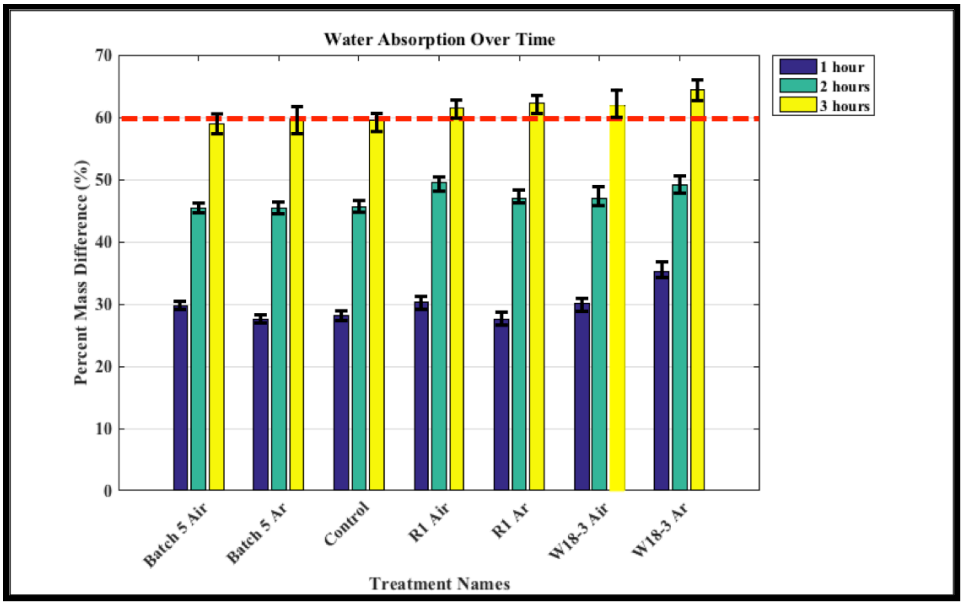

Figure 5-11: Representation of the percent mass difference from the recorded mass of the data set after treatment and then again after the allotted absorption time. The red 'dashed' line represents the value of percent mass difference of the control at three hours and allows for easy visual comparison of the results. The labels 'Ar' represent the argon feedstock gas treatments verses the 'Air' feedstock gas.

The dashed line allows for easy visual comparison amongst the different treatment sets with the control. Within the first hour, the control group absorbs more water than 3 of the 6 treated sets but is only comparable at the 2-hour mark and then falls into last place at the 3-hour mark when comparing strictly to the treated seed data. After three hours, the control group had an increased mass percentage of 58.9% but was 5.5% behind the T3-Argon treated group that had the most water absorption after three hours.

Following the leading group at the three-hour absorption measurement was another argon gas treatment set then two air treated sets followed by the short duration argon treatment.

When comparing the percent mass difference from the water absorption trials to that of the contact angle measurements, one can see the expected correlation of a lower contact angle resulting in higher water uptake. Figure 5-10 represents the contact angle measurements of the seeds treated within the reactor. The correlation of the low contact angle measurements of the T3-Argon and T2-Argon sets with Fig. 11 shows agreement with hydrophilic effects of the argon treatments. A point of interest of these figures is that the T2-Argon treatment granted the lowest contact angle measurement but resulted in the second most water absorption behind the T3-Argon treatment. This result suggests that there may be some influence on the conditions of the treatment and the biological response that also impact water absorption of the seed.

5.5.2 Plasma Activated Water Results

Water absorption with plasma-activated water (PAW) is also of interest as PAW is reported to have beneficial developmental effects reported within the literature. Plasma activated water is of interest as manipulation of water properties may help promote biological growth and development of certain organisms. Plasma activated water was included in this report to determine if modifying water properties had an influence on imbibition and contact angle. The seeds used were not plasma treated although the water droplet had been modified.

Treatments of the PAW occurred over a duration 5 minutes. Water absorption measurements were made using a set of untreated seeds within the 53 ± 0.15 gram limit. The plasma activated water was then supplied to the seeds for the various 1, 2, 3-hour interval sets. Results of the water absorption test had shown less of a percent mass

difference than the control group at time interval as shown in Figure 5-12. The overall water absorption for each of the three PAW sets at the end of three hours of absorption did however remain close to the final control value of 58.9% with percent mass differences of 57%, 56.9%, and 57.6%. The water uptake similarities between the plasma activated water trials and the control was expected to be similar if one correlates to the proceeding argument regarding contact angle measurements and water absorption. Since the PAW had contact angle values similar to that of the control seed and control water, a significant difference here would be surprising. The difference that is seen, however, may be attributed to the different chemistry within the water due to the plasma treatment and therefore may also interact biologically different to the seed coat.

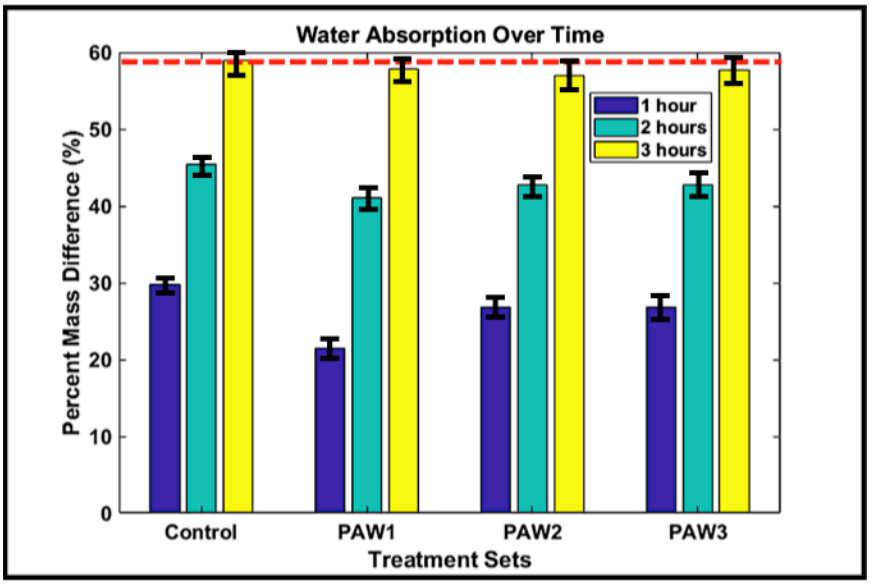

Figure 5-12: Representation of the percent mass difference from the recorded mass of the data set before absorption and then again after the allotted absorption time using the PAW. The red 'dashed' line represents the value of percent mass difference of the control at three hours and allows for easy visual comparison of the results.

The nature of plasma propagation through a bed of seeds was investigated in both a 2-D and 3-D apparatus. It was found that morphologically, plasma propagation through a seed aggregate is similar to that of inorganic media. That is, discharge propagated as an ionization wave featuring FMs between media and SIWs along the surface of media. FM tended to be less localized in the case of the seeds suggesting feedback from the surface

due to etching or outgassing. Such feedback tended to increase the active areas exposed to the more intense micro-discharges. The effect of plasma treatment of seeds was also assessed via contact angle and water absorption tests. It was found the Ar mixtures tended to have the greatest effect on seed contact angle.

The filamentary micro-discharges also influenced the contact angle more so than the regions in which surface ionization waves had dominated. This work should provide insight into the design of packed bed reactors for seed treatment. An investigation was conducted in regards to the surface energy of the seed coat by measuring the contact angle of treated seeds and treated water. These tests resulted in argon treatment of the seeds leading to a much lower contact angle than the identical air treatment. The plasma activated water also had a different contact angle than just the control seed and control water with an initial angle resulting around 70 degrees for each trial set with the control being around 80 degrees and the treated seeds from 85 degrees down to 11 degrees. Finally, a correlation was made between the contact angle measurements and the amount of able to be absorbed by the seed in a set period of time. A lower contact angle was shown to result in higher mass amount of water absorption by the seed. In this work, the direct treatment trials exhibited higher water absorption than the plasma activated water trails. Plasma activated water absorption was found to be similar to the control group.

5.6 Concluding Chapter Remarks

The experimental campaign pursued within this chapter was to determine the effects of the direct plasma treatment of seeds on water absorption as well as the inclusion of plasma activated water. It was shown that the direct treatment of the seed did have an impact on the contact angle observed on the water droplet. Air treatments were shown to decrease the contact angle but not nearly as much as the argon plasma

treatment. This was then correlated to water absorption results in which the lower contact angles resulted in higher water absorption amounts as expected. The argon plasma has different reactive species and plasma densities that attributed to the difference in surface group energies on the seed, which have been seen in preliminary x-ray photoelectron spectroscopy work. This work is being performed as a collaboration between two NASA John F. Kennedy Space Center research groups (the VEGGIE group and the Applied Chemistry Laboratory). The lower energies present evidence that the binding energies on the surface of the seed have been modified from the plasma treatment. The work will be completed by August 2019 with results being published shortly thereafter and the reader is referred to the upcoming publication for greater insight into the biological aspect as well as more physics insight.

Chapter VI

Discussion of Future Work

Packed bed reactors have many future applications in environmental remediation and chemical processing techniques. In order to develop efficient systems, a greater understanding of the plasma physics of these discharges is required. This dissertation presents some of the findings for a greater manipulation of these applications. Each experimental chapter of this dissertation provides opportunities for further investigations using additional diagnostic techniques and studies.

The results in this work were based upon single pulse observations. The formation and propagation methods provide insight into system design and plasma initialization. After the system's initial pulse, however, the second plasma pulse will be generated in a modified environment derived from the previous pulse history. The preceding pulse can locally change the surface temperature, introduce charged species, give rise to possible residual material charging, drive surface texturing and the formation active sites, and introduce new gaseous species associated with plasma driven outgassing from organic aggregate. The aforementioned findings are essential for plasma breakdown but future work involving the same system and experiments looking at the third or fourth pulse in a series would provide insight to the system evolution as a function of time.

Additional work in Chapter III, many more investigations may take place utilizing the 2-dimensional cell. For instance a greater understanding of the packing fraction effects on the discharge could be performed. This would be done with pellets of varying

sizes of the same dielectric material in a limited volume. This was not performed for this report, as manufacturing of the materials is difficult and expensive. Additionally, the implementation of a laser for laser induced fluorescence measurements would give information on the plasma such as electron temperature and species densities. Changing the dielectric constant of the material while keeping the same aggregate shape and size would also be an insightful investigation as to how the electron temperature and species density profile's would change.

Chapter IV would build off of the different investigations of continuing the work of Chapter III. Optical emissions spectroscopy techniques and laser-induced fluorescence provide additional details to this work and allow for a greater understanding of the plasma manipulation. The work here leads to the ability to manipulate the species produced with the dielectric aggregate material. Additional work in this chapter would include an increase in the variation of aggregate with larger dielectric constant values. Investigations of aggregate particle size on the discharge species would also be of interest for the optimization of packed bed reactors.

Chapter V is an understanding of the plasma biological interactions. The results presented herein provide insight as to how the plasma forms and propagates in an organic packed bed reactor system. The findings led to a greater understanding on how to change the contact angle of the seed and which plasma treatment conditions resulted in the highest recorded water absorption. Future work in this chapter would involve surface analysis of the soybean seed coat as well as a more complete characterization of the plasma activated water. For the direct plasma interaction with seeds, surface analysis would include scanning electron microscope (SEM) imaging, x-ray photoelectron

spectroscopy (XPS), and atomic force microscopy (AFM). The SEM imaging would provide visual inspection of the seed surface to determine any morphology from the plasma interaction with the polymer-like seed coat. Additionally XPS would determine the modifications in the surface bond energies due to the plasma interactions. The XPS system etches away surface layers as well that would provide insight as to the penetration of plasma species into the biological material. A slight shift in the measured surface energies will tell whether the surface is a C-O dominated bond or a C-C or C-N. This data will also provide information on the energy of the particles bombarding the surface. Lastly, AFM may be used to correlate the bonds found with the XPS system. Precaution must be taken with the AFM as it may influence the measurements based on the methodology of the measurement.

The plasma activated water for agricultural purposes in this section are preliminary and the first task of future work would be to better characterize the water modifications resulting from plasma interactions. Following this, the characterized water properties from plasma treatment may be correlated to the suited growing conditions of the plant for growth trials. Resulting in a tailored water treatment for the promotion of specific plant growth.

Appendix A is on the application of a plasma packed bed dielectric barrier discharge in an agricultural setting. The work presented here was a starting point into the investigation of direct plasma treatment on germination and early growth development. Additional work here needs to be performed with a large number of treated seeds in order to gain a better statistical result. To understand the effects on primary and secondary root development, the roots need to be separated from the plant and dried in an oven. The

overall root dry mass for each treatment would tell how the different treatments affect early root development beyond the taproot length measurements presented. An experimental campaign may also be undertaken in regards to the mRNA up and down transcription. The transcription process observes protein production rates of a specific gene that may then be correlated to select physiological traits. A selection of the gene UPBEAT1 has already been chosen for these tests as it correlates to root development. Equipment is available at the University of Michigan to begin these tests and contact has been made with an associate professor for training and use of the machines. The growth and germination trials mentioned within Chapter VI would also now involve the plasma activated water in parallel experiments that record the same metrics. Direct comparisons may then be discussed between the direct plasma treatment of the seeds and the effects of plasma activated water.

Overall the discharges of packed bed reactors and micro-porous media are complex and the report of this thesis is to shed light on the discharge propagation and formation. A greater understanding of the discharge propagation was found and relates to factors such as voltage, dielectric constant of the media or aggregate, packing fraction, frequency, species production, and whether the material is organic or inorganic in nature. Each chapter grants a new understanding of the packed bed setup with the final two chapters providing an application approach.

Appendix A

Plasma Interactions With Organic Material:
Applications To Agriculture

A.1 Introduction to *Glycene max:* The Soybean Organism

A.1.1 Brief History of the Soybean and its industrial use in the United States

The soybean was first cultivated in southeastern Asia region of China, Manchuria, and Korea in the wild form of the plant called *Glycine ussuriensis*.[96] The cultivation of the soybean plant is recorded in ancient Chinese literature. The importance of the soybean in modern day use is that the seeds can be produced more cheaply as compared to other similar crops, is rich in oil, high in protein for edible products, and has a high yield capacity. The first extensive use of soybeans in the European market was for the to make soft soaps and later in the United States for soap, paints, lard, and butter substitutes with the ground cake being used for cattle feed.

Soybean integration into US markets at significant levels started just after the first World War. Soy foods were encouraged as a source of protein during the war when nearly a decade before, George Washington Carver determined its value by producing edible oil and meal.[97] Soybeans saw extensive use as a supplement for animal feed during this time. The development of the combine in 1920 greatly improved harvesting efficiency of the soybean. Then in 1922, the first U.S. soybean processing plant opened in Decatur, Illinois which brought about wide-spread implementation of the crop in the

Midwest region.[98] An interesting use of the soybeans between world wars was implemented by Henry Ford. Henry Ford had directed the Ford Motor Company to create a car that was constructed from soy-based plastics.[99] The project had however ended at the start of World War II due to refocusing of industry on the war effort. During the war, soy became an essential part of the American diet for its oil use as well as tofu.[100] Post-war, the soybean became an inexpensive, valuable source of protein and production bloomed drastically as the U.S. livestock and poultry production began to increasingly use the soy meal in feed. The domestic market expanded greatly throughout the 1950s and 60s giving rise to the American soybean market to become the largest for exports. From the 1970s onward, soybeans remained a significant part of American exports by volume and dollars. Technological advances have brought upon genetically modified organisms (GMOs), which have resulted in higher yields along with advanced machinery allowing ease of harvest and processing, and more efficient industrial processing techniques.

Figure A-1: Semi-aerial view of soybeans being grown on Engeling Bros. Farms in the central Illinois region.

A.1.2 Soybean Biological make-up

Soybeans like most angiosperms develop from seeds to seedlings to mature plants. The first stage of growth in the seeds is germination in which the seed begins to awaken with the emergence of the seed radicle.[101] Following the emerging radicle, the cotyledons develop from the hypocotyl, which are the first photosynthetic structures of the soybean plant. The representation of the soybean plant and each of the structures are

shown in Figure A-2 for reference. These cotyledons are the first source of nutrient collectors by acting as the

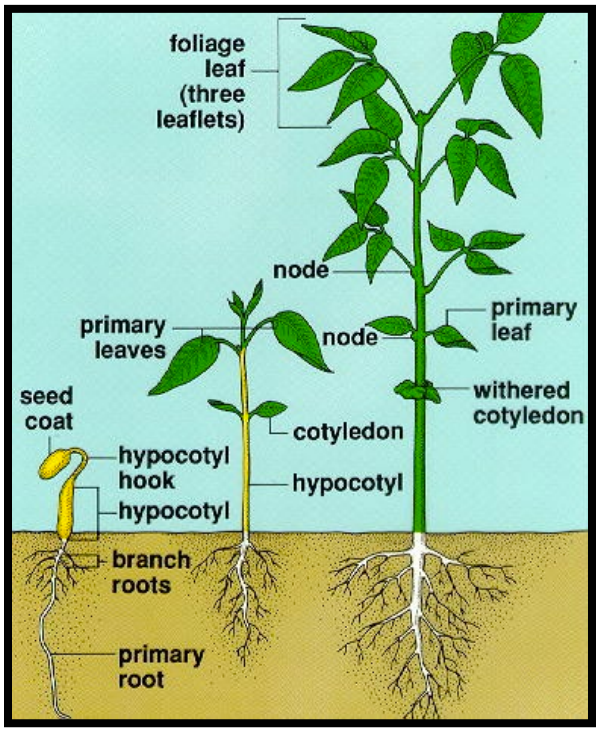

Figure A-2: A diagram that represents the stages of soybean development with the plant's components labeled.

seed's leaves for the first 7 to 10 days. Following the first stage of germination is when the seed begins to mature and develop its first leaves and then additional leaves as the plant develops. Reproductive stages of the soybean plant are based on flowering, pod development, seed development, and plant maturation. The pods produced almost reach full size before the seeds begin to develop. As the plant matures, the leaf and pod begin to yellow at the same time and therefore showing maturation. The duration in which maturation is achieved depends on the variety of the plant but generally occurs on the order of days to weeks. The root system has three distinctly defined components known as the primary root or taproot, the secondary or lateral roots, and then the tertiary roots that originate from the lateral roots.[102]

One of the most important structures of the soybean is its seed coat. The seed coat is responsible for water imbibition, prevents soaking damage[103, 104,105,106] and protects against deterioration.[107] Seeds that do not readily uptake water are considered hard and may not even begin development in favorable conditions for prolonged periods.[108] The barrier system for soybean seed coats for water permeability is similar to some genotypes of *Glycine max* are composed of structural and chemical composition.[109] Vu et al., performed water absorption experiments and acquired scanning electron microscope images of the seed coat surfaces of six different genotypes in order to study the seed coat. This study indicated where water entered into the seeds via fluorescent trace dye. Variations in rate of water imbibition, the compositions of the seed coat, and locations of water entry into the seed were assessed as well. Overall soybean development can be influenced by temperature, day length, and variety among other factors and therefore this can lead to considerable variation to the number of days between developmental stages.[110,111]

A.1.3 Influence of electroporation effects on soybean on soybean germination

Electroporation of cell membranes in order to increase the permeability is widely used in research and industry.[112] Electroporation is the application of an external electric field via electric pulses that force open pores in cells. It is generally classified into a four stage multi-step process: 1) charging and polarization, 2) temporal destabilization and pore creation, 3) expansion pore radii, and 4) re-sealing and memory effects.[113] The duration of the electric pulse is dependent upon the target organism's cell size and structure. The typical pulse durations for small organisms is on the microsecond time scale and milliseconds for large organisms.[114] Time-scales of the electric pulses utilized within this dissertation, however, are on the nano-second time scale. Based on previous

work, electroporation effects based upon pulse width are only of interest below 10 ns and the pulses used here are either 60 ns or 120 ns.[115] Additionally it was found that the electric fields needed for cell apoptosis are on the order of 2x greater than those simulated within the ANSYS: Maxwell model. Additionally, the opening of the cells and conductance was seen to be reversed after nearly two minutes in another study, negating water absorption from electroporation.[116] After treatment of the seeds, a time greater than two minutes was required for equipment disassembly and seed transfer. In this regard, electroporation effects in this work have been disregarded. Future work may further investigate and validate this assumption.

The most applicable use of current day electroporation is for gene insertion and drug delivery into living cells. The cell membrane opens up because the conductivity of the cell membrane is order of magnitude lower than the cell cytoplasm and cellular medium as described in work elsewhere.[117,118,119] The effects of electroporation may be reversible or irreversible based upon the parameters of the electric pulses. For the opening of the cell membrane to be fluid, a threshold value of the membrane potential may not be exceeded in which the membrane disintegrates and usually ends with cell loss.[120] Overall, electroporation is a beneficial procedure for biotechnological and medical applications. The details of the physics and biological response are beyond the scope of this work and is left for further investigation by the reader within the referenced articles.

A.1.4 ROS/RNS Roles with physiological development

Reactive oxygen (ROS) and reactive nitrogen (RNS) species are naturally occurring within the cells of organisms. Through metabolic processes plants produce some of the same ROS that are produced by air plasma.[121,122,123,124] These ROS and

RNS play roles in various processes in the developing plant such as dormancy alleviation and germination (high accumulation of ROS during these processes and then ultimately a high release of ROS during germination, thought to potentially be involved in pathogen defense). Figure A-3 depicts the complexity of the ROS and RNS cross-talk within the plant structure corresponding in the plant *Arabidopsis*.[125]

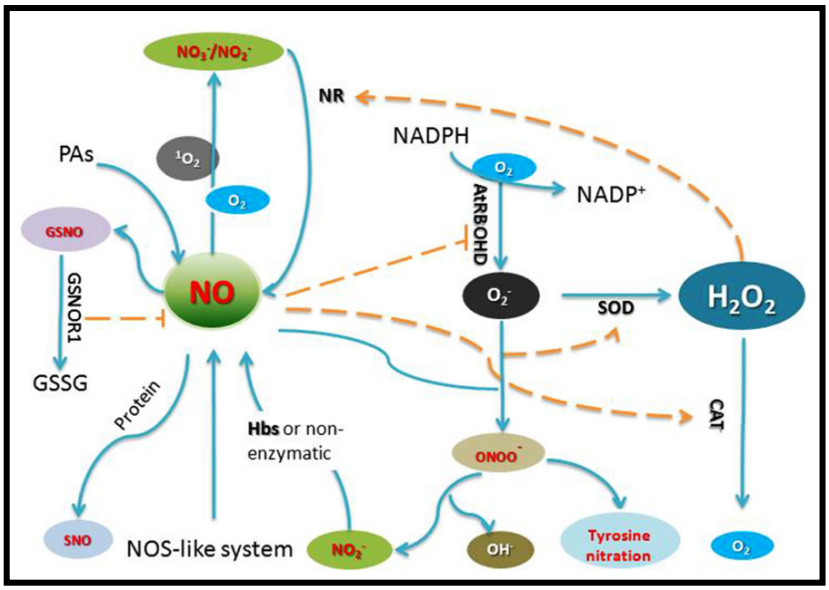

Figure A-3: Chart produced by Y. Yang et al. that shows the cross-talk of some of the ROS and RNS species in the well characterize plant *Arabidopsis*.

H_2O_2's involvement in these processes has been well studied to date. Proteins in particular are sensitive to the presences of ROS and RNS.

Zhang et al., had shown that argon plasma can have a growth-inducing effect on soybean sprouts.[Error! Bookmark not defined.] This effect was determined by studying the regulation of demethylation levels of energy metabolism-related genes. A 6-day-old sprout was in contact with the argon plasma. This work related gene expression of adenosine triphosphate (ATP), target of rapamycin (TOR), growth-regulating factor (GRF), and the corresponding mRNA expression. The group used an AC dielectric barrier discharge reactor operating at 60 Hz and 10-22 kV rms. The power of the reactor during experiment varied from 3.4 to 15.6 Watts. This work found that argon plasma

could give rise to positive or negative biological responses depending on discharge parameters.

A.2 Overview of Experimental Campaign

The effects associated with the interaction of plasma with living cells is not well understood. This is attributed to the complex chemistry that follows the interaction of plasma with organic media. Plasma is a source of a gas phase active species that interacts with the biological substrate. Direct plasma driven surface interactions such as photon/ion/electron bombardment, etching, gaseous diffusion, and off-gassing, add to the complexity of the interaction. In this work, the physical impact of plasma flux upon the surface of seeds is explored; additionally, the impact of treatment on germination is explored. The seeds utilized for these experiments were the Asgrow AG43X7 variety with a 4.3 relative maturity and are designated as Roundup Ready 2 Xtend. The 4.3 relative maturity refers to the average days required for full maturation and the Roundup Ready means it has been modified to be resistant to roundup chemicals. Argon and compressed air were used as the feedstock gas for the packed bed plasma reactor. Compressed air had been chosen due to being readily available and low cost. On the other hand, air plasma chemistry is complex thus making interpretation of the interaction not straightforward. Therefore, argon gas was chosen for ease of simpler kinetic studies.

The experimental setup for the plasma treatment of soybeans is shown in Figure A-4. The electrodes were set up in a coaxial geometry with a central rod electrode made of stainless steel and an outer, copper mesh electrode outside of the glass cylinder as shown in (b). After each treatment set, the end caps and rod electrode were removed from the reaction chamber. Isopropyl alcohol was used to rinse the cylinder as moisture and sediment would build-up on the inner surface. The glass cylinder was then dried

with a cloth through the inner opening. During the treatments, oxidation of the electrode would also occur and therefore after each operation the electrode was cleaned with sandpaper, rinsed with isopropyl alcohol, and dried before re-installation into the 3-dimensional chamber.

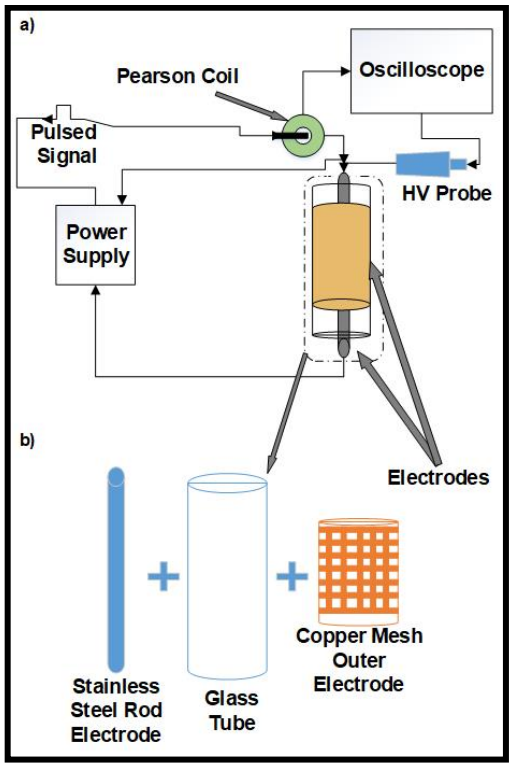

Figure A-4: A simple schematic of the experimental setup utilized for the treatment of the soybeans for germination in growth trials.

The complete seed treatment parameters are presented in Table A-1. Batch #2* and Batch #12* are denoted from values modifying for the 7-day growth period. These values were modified by accident but led to positive results. The direct treatment of the seeds within the packed bed reactor varied based upon voltage, frequency, duration, pulse width, and feedstock gas type. The discharge conditions set for treatment with a pulse width of 60 ns, pulse peak voltage of 18 kV, and a frequency of 5 kHz. This maximized plasma coverage of the aggregate. At the beginning of the experimental campaign, 13 different treatments were chosen at varying ranges of power deposition as shown in Table

A-1. Settings were chosen for both 'high' and 'low' power output in regards to supply limitations. The reactor was packed for treatment based upon selected mass amount of seed. This means that each treatment had a number of seeds that weighed 7.7 +/- 0.15 grams. A set mass was chosen due to the variations in soybean size and shape. An image of plasma formation throughout the 3-dimensional packed bed reactor is shown in Figure A-5 following the treatment parameter table.

Table A-1: A complete list of all of the treatment parameters employing the EHT-NSP-120 power supply for plasma generation during the soybean seed treatment in the packed bed reactor.

Treatment Name	Voltage (kV)	Frequency (kHz)	Treatment Duration	Pulse Width (ns)
Batch #1	14	2	20 mins.	60
Batch #2	14	4	15 mins.	60
Batch #3	14	2	15 mins.	60
Batch #4	14	2	10 mins.	60
Batch #5	14	2	3 mins.	60
Batch #6	14	4	10 mins.	60
Batch #7	14	4	3 mins.	60
Batch #8	12	4	20 mins.	60
Batch #9	12	4	15 mins.	60
Batch #10	12	6	20 mins.	60
Batch #11	12	6	15 mins.	60
Batch #12	12	4	10 mins.	60
Batch #13	12	6	10 mins.	60
Batch #2*	14	2	15 mins.	60
Batch #12*	14	3	3 mins.	60
W18-1	16	3	30 s	60
W18-2	16	3	30 s	120
W18-3	18	3	30 s	60
N-1	18	2	2 min	60
N-2	10	3	7 min	30
E-1	15	2	5 min	90
R-1	12	2	10 min	60

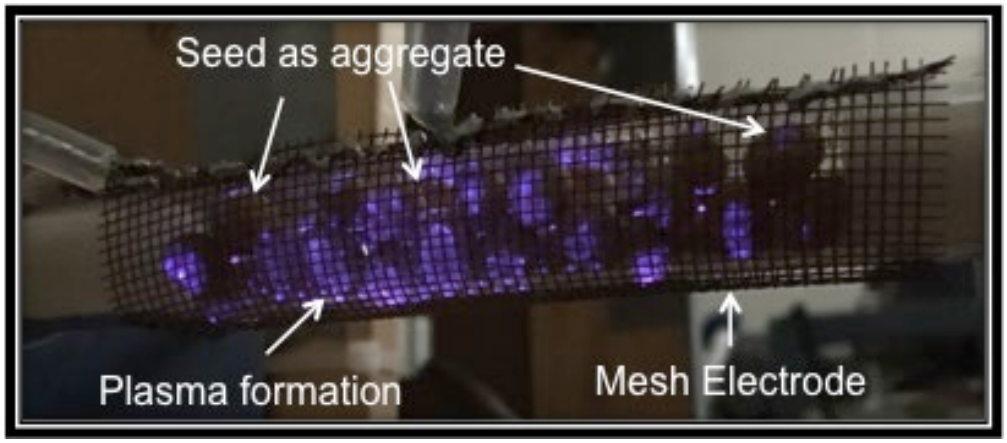

Figure A-5: Image of the plasma formation and propagation in the 3-dimensional packed bed reactor filled with soybean aggregate.

At some of the power settings condensation was seen on the inside of the tube, burn spots on the seed, as well as carbon buildup on the central rod electrode, and a burnt smell. The trials at the higher power for longer durations were significantly more damaging to the seed coat upon visual inspection. The damage which included cracking or splitting and will be discussed in the following subsections with more detail. Electrical diagnostic waveforms were captured with two P6015A Tektronix high voltage (HV) probes and a Model 0585 Pearson coil. A HV probe was placed at each electrode of the reactor with the grounds of each probe jumpered to Earth ground. A Model 585 Pearson coil recorded the current.

Plasma activated water used for the germination and growth trials was produced using an underwater plasma jet. This jet was excited using low frequency sine waves and a low frequency, nanosecond pulse. An FID and Eagle Harbor Techn. Supply explored the ns regime. Air flow rate into a quartz tube of ≈ 710 SCCM. Different power supplies were implemented into this study due their varying effects on the properties of the treated water. For instance, the AC plasma jet over a comparable time period led to more thermal heating, greater change of the pH, NO_3^- concentration, and NO_2^- concentration

than the pulsed systems. The pulsed systems, however, produced more H_2O_2 and had no thermal heating.

The treated water sets were based on a measured 300 mL of tap water. The starting water was tap water. The treatment parameters of the various systems are tabulated in Table A-2. In some of the trials, the underwater plasma jet was operated without air flow. Here the jet generated its own bubble (steam) in which the plasma formed. It should be pointed out that treatment times for the Elgar excited samples was limited owing to the fact that significant increases in water temperature were observed with this low frequency discharge. In some of the trials, the underwater plasma jet was operated without air flow. Here the jet generated its own bubble (steam) in which the plasma formed. It should be pointed out that treatment times for the Elgar excited samples was limited owing to the fact that significant increases in water temperature were observed with this low frequency discharge.

Table A-2: Listing of the power supply settings for the generation of plasma activated water.

Treatment Name	Voltage (kV)	Frequency (kHz)	Time	Pulse Width (ns)	Type
FID-15	10	7.5	15 mins.	100	Steam Jet
FID-5	10	7.5	5 mins.	100	Steam Jet
FID-5	10	7.5	5 mins.	100	Bubble Jet
FID-15	10	7.5	15 mins.	100	Bubble Jet
Elgar-6	9	5	6 mins.	N/A	710 SCCM
Elgar-2	9	5	2 mins.	N/A	710 SCCM

A.2.1 Germination Tests

Seed germination is a crucial step in the physiological development of plant organisms. Therefore an early stage germination and development experimental campaign was performed. Soybeans were used for the study at the University of

Michigan Botanical Gardens using the packed bed dielectric barrier discharge method with the Eagle Harbor Technologies nanosecond pulser. The average germination rate of this particular organism is 1-2 days and emergence from the soil occurring three or more days after planting according to the Asgrow information website.[126] The study allowed for data to be collected over the course of four days. This was to allow for collection of data on seeds that might germinate later than the published average. The extra time also allowed for early primary root development measurements to be made, color changes to begin occurring, and in some cases even the significant emergence of the cotyledons. Measuring the primary root length during these tests was important because 76 percent of soybean roots grow in the top 38 centimeters of soil under the best conditions, with the ability to grow downward at a rate of 1.25 cm per day. Therefore, the primary root growth rate and root emergence time is important.

Post treatment, the seeds were placed in an open, well-ventilated container in direct sunlight and enveloped in a paper cloth. The paper cloth was implemented to help retain moisture. 50 mL of tap water was added to the seeds within the vented container on the first day with the paper cloth retaining the moisture. Each additional day during the 4-day test, 10 mL of additional tap water was added to the treated set to ensure the seeds did not dry out. The temperature was kept around 29.5 °C, receiving equal amounts of sunlight per day via time-controlled lamps. The seeds were then carefully removed from the bag at the same time for each trial at the end of the fourth day. The color of the seeds was recorded as well as the taproot length and any secondary root development. Data was logged via pictures and measurement spreadsheets that were connected to the respective treatment parameters.

A.2.2 Growth Trials

Early developmental growth trial experiments were performed to gain insight into the possible effects of plasma treatment of seeds during early physiological development. The results of the germination tests showed an influence on germination parameters but these do not necessarily correspond to changes in early stage development. Therefore in order to study development, the botanical gardens at the University of Michigan was utilized to actually plant the seeds. A large volume of soil of one type was acquired to eliminate variability. The growth trials were allowed to germinate and develop for the duration of 12 days before being harvested for measurements. The seeds were placed individually in a flat that contained 72 pods. Up to 10 flats would be in use at one time. Each pod was filled two-thirds full with fresh soil before a seed was placed. The exposed seed was then covered with soil up to the brim of the pod. Each freshly planted pod then received 20 mL of tap water and was placed in the greenhouse. The plants were in a climate-controlled environment at the Matthaei Botanical Gardens at the University of Michigan.

Every other day, an additional 10 mL was pipetted unto each pod. The controlled watering ensured equal conditions for each of the seeds and the flats were evenly spaced underneath the growth lights. The temperature within the research greenhouse was only allowed to fluctuate a few degrees Fahrenheit, ensuring similar conditions for each data set. The overhead grow lamps were set to a timer, controlling the amount of growth light available. An example of the facility and setup of the soybean growth trials is shown in Figure A-6. The various treated seeds were marked by a colored tag placed in the pod corresponding to

Figure A-6: Image representation of the flat of a growth trial in which the treated and control seeds have been designated with a color-coded tag.

the treatment performed on the seed. Each flat had 72 pods divided into sections of 6 pods. Within each section, seeds from all of the treatment sets were planted randomly with their colored tag. This is to ensure that no one treatment set received more light than other sets based upon physical location in relation to the growth lights. After each watering, the flats were re-positioned in order to try and promote an even irradiance during the trial period.

The soybean plants were "harvested" after their growth period with notes taken on appearance. The harvesting of the plants involved carefully removing them from the pod and gently washing the roots to remove and soil particulates still adhering to the surface. The 12-day grown plant was then laid out and measured from the tip of the taproot to the top of the primary growth node. Observations of cotyledon color and primary leaf emergence was also noted. Each plant height from the various treated groups and the control was then compared as well as a group mean and averaged was computed. The primary root length and plant height was measured by a cut made separating the roots

from the plant near the point of soil emergence. The point on the stem in which photosynthesis had begun to affect the stem's color determined the cut location. Although taproot length data is crucial for analysis, it was also important to determine the amount of secondary root development as it differed drastically depending on the treatment.

In order to determine the promotion of additional secondary roots, two different procedures were considered. The first procedure involves counting each branching secondary root and each of the further branching nodes off of the secondary root. The second method involved performing a dry mass measurement of the entire root system. The roots, after being cut and measured, were placed upon wax paper and allowed to dry in an oven at 70 degrees celsius for the duration of three hours in order to get approximately 90% of the moisture out. In order to attain 100% moisture loss, a bake-out time on the order of three hours was required. A longer bake-out time was not chosen for the data collection due to the interest of time. This shortened bake-out time was consistent for each of the trail sets. Future work involving a research grade laboratory oven would allow for the longer bake-out times required for near 100% moisture expulsion. Additional information such as the number of leaf and secondary leaf development could have also been recorded for further insight into physiological development but was not collected at this time.

A.2.3 Disinfection and Sanitation in the Literature

Plasma sterilization has been considered for the disinfection of pathogens for applications ranging from sterilization of medical tools to the removal of bacterial from fruits and vegetables. [127,128] Such methods can be used to remove the bacterial load on

seed surfaces thereby extending seed storage life as well as improved survivability during germination

Plasma sanitation of the seeds during pre-sowing treatment or the sprouts post treatment may prevent some of the fungal developments seen below in Figure A-7(b). In (a), one can see that fungus has decimated the germination and growth of a significant portion of the flat with a close-up image in (b). Of the 72 untreated seeds in this flat, only 26 of the plants germinated with 10 of those 26 having any significant growth development. Of the remaining 46 non-germinating pods, 38 had shown little to severe fungal growth. The ability to determine if the plasma treatment of the seeds, before or after being sown into the ground, improves plant survivability is a goal of this study.

Figure A-7: Example of some of the fungal developments that may occur with older, unsterilized seed. The images were taken from a control data set in which no seeds were treated with (a) being the entire flat and (b) a close-up.

A.3 Results of Germination Trials

A.3.1 Air Treatment Germination Results

Compressed air was the first feedstock gas to be used with the packed bed dielectric barrier discharge reactor for the germination test study. The feedstock gas inlet

was connected to the chamber via a plastic tubing connection at the end cap. The flow rate was set to 30 SLM with an exit on the opposite end of the reactor. The treated seeds' roots were measured using a ruler and measured from the point of primary root emergence from the seed to the end of the taproot. Figure A-8 (a-f) shows examples of different germinated seeds as they are organized and measured. The declaration of germination was determined by a color change, emergence of the primary root from the seed, splitting and movement of the cotyledons, and shedding of the thin seed coat layer. Some of the resulting trials resulted in little to no germination. These trials were noted and repeated two more times for consistency. The trend of little to no germination continued and therefore these treatment parameters were not included for the 7 and 14-day growth experiments.

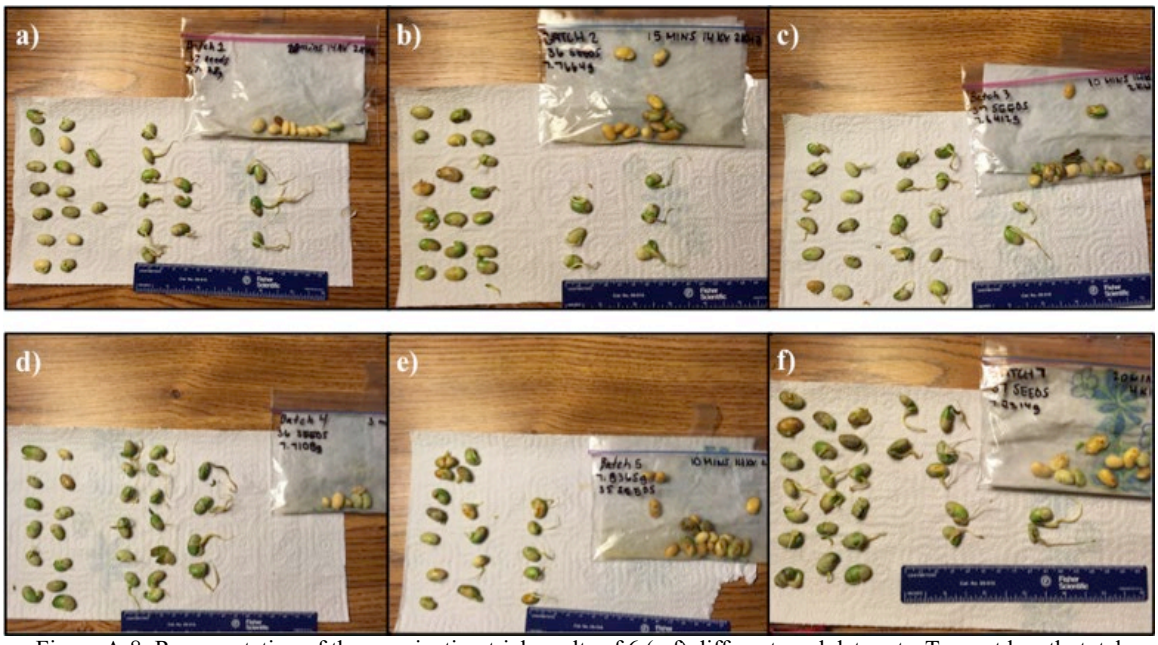

Figure A-8: Representation of the germination trial results of 6 (a-f) different seed data sets. Taproot length, total number germinated, and notes about the color of the seeds were all recorded.

It was found that the plasma treated seeds displayed a range of responses ranging from beneficial to detrimental relative to the control group. The experiments were performed in triplicate remove data outliers and ensure repeatability. Results from the air

treated germination studies over the first treated parameter sets led from germination values ranging from 17% to 76.50% as compared with the control whose germination percentage was near 72%. The results of the seeds with germination percentages comparable to the control and will be considered for future implementation is shown in Table A-3.

Table A-3: Results from the first four germination trial data sets.

Air-plasma Treatment Germination Tests	
Treatment Name	**Avg.% Germ.**
Control	**71.80**
1	**76.50**
2	**69.50**
3	**68.65**
4	**67.30**
5	**72.60**
7	**64.71**
9	**71.90**
12	**70.85**

The germination tests generally resulted in values that were comparable to the control for the air-plasma treated soybeans. Batch #1 appeared to germinate on average about 5% higher than the control group. These results were used to select the appropriate treatment parameters for 14-day growth tests. Each of the treatments presented in Table A-3 were repeated and planted. As one will notice in the following sections, Batch #1 eventually is no longer mentioned and this is due to poor performance during the growth trials when compared to other treatments. Therefore the results from the germination trials allowed for a down select to occur for treatments with high germination rates and then the later growth trials determine the longer-term effects of the plasma treatment for

further down-selection. To determine if the higher germination percentage would correlate the same with a different feedstock gas such as argon but with the same treatment parameters, another experimental campaign was performed.

A.3.2 Argon Treatment Germination Results

Argon germination trials were held to the same standards and procedures as the air treated plasma data sets. The seeds were treated and then placed into the soil and given 20 mL of water each initially and then 10 mL of water for every second day after treatment. A point of concern when performing the argon trials was that the seeds had begun to lose germination capabilities due to long-term storage that was not in ideal storage conditions. The results from the argon treatment trials will be discussed here but only briefly as the experiments should be repeated with fresh seed to better determine plasma-induced effects and not natural biological effects.

The argon treatment germination trials were performed for and compared amongst the W18-3 and R-1 treatment parameters with a control. Future work was to involve experiments involving the complete list treatment parameters seen previously in Table A-1. For each argon treatment, there was an identical air-plasma seed treatment performed in order to reduce the effects of natural seed longevity mechanisms. Briefly, the comparisons of the argon germination trials were on the same order of the control and air treatments within 3% of each other's average germination percentage near an 85% average. The main difference between these germination tests and the previous germination tests is that these tests were performed on the select group of treatments that had the highest germination parameters and therefore varied less than some of the previous germination trials. For the W18-3 air and argon, the germination percentages for each when compared to itself was within 2% and therefore considered identical.

However, for the air and argon feedstock gas treatments utilizing the R-1 parameters, a drastic change was recorded. For the air treatment, a germination percentage was recorded to be near 80% for these data sets but the R-1 treatment with argon feedstock gas led to a reduction in germination to only 20%. Further diagnostics of the plasma properties and species being produced is needed to have a more conclusive reasoning behind such a drastic difference.

A.3.3 Plasma Activated Water Influence on Germination Results

The plasma activated water was treated in three different ways for germination trials. The first form of treatment was a steam jet employing the use of an FID nanosecond pulser with the voltage set to 10 kV and the frequency set to 7.5 kHz with a pulse width of 100 ns. The second was performed using the same power supply but varying the compressed air flow rate to where the plasma would form in bubbles and then enter the water and therefore changing the reaction mechanisms occurring within the water. The third treatment of generating the plasma activated water in this section implemented the AC supply from ELGAR with 9 kV voltage and 5 kHz frequency with a compressed air flow rate of 710 SCCM. These trials were not performed in large quantities and therefore only preliminary data is presented here. Future work should involve larger number of flats for less chance of natural statistics influencing the data.

The resulting germination percentages from each of the small seed trials resulted in a range from 91-100% as shown below in Table A-4. Some caution should be taken with these numbers until a larger data set is acquired but the acquired data is presented below albeit brief. The results had shown the best results with the steam jet treated water on germination than the other plasma activated water treatments. The control was given tap water for the tests.

Table A-4: Tabulated germination results from the use of plasma activated water for six differing treatment parameters.

Treatment	% Germ.	Duration
Steam Jet	100	15 mins.
Steam Jet	100	5 mins.
Bubble Jet	95.83	5 mins.
Bubble Jet	91.67	15 mins.
Elgar	91.67	6 mins.
Elgar	95.83	2 mins.
Control	97.92	N/A

Although it seems as though the steam jet plasma activated water resulted in the best germination percentages, more extensive testing is required. When comparing the water properties of the various treatments, the Elgar supply had shown the most change in pH level with the 6-minute treatment leading to reading of 4.97 and the 2-minute with 6.61. The tap water of Ann Arbor maintains a pH level near 8 and the bubble Jet trials had brought the pH to a 7.25 and 6.72 level readings for the 5 and 15 minute treatments, respectively. The steam jet saw little to no change in pH with the readings remaining in the high 7's. The conductivity of the water was recorded and ranged from the 500's $\mu s*cm^{-1}$ in the bubble and steam jets to 600 and 760 $\mu s*cm^{-1}$ for the 2-minute and 6-minute Elgar treatments. A more extensive study on water properties affecting soybean germination and development is required in order to provide a more definitive analysis of the plasma activated water effects. Therefore, this section remains non-conclusive on complete effects of the aforementioned treatments but do suggest that there is some biological response to the varying water properties.

A.3.4 Comparisons between the Effect of Air and Argon Discharge

Treatments that had led to higher secondary root development or longer length taproots did not necessarily correspond to the best results as seen with the germination

tests. For instance, some had better germination test results such as Batch #1 but overall eventually was no longer utilized with the growth trials that occurred over the 14-day trial due to poor performance. In order for more insight to be gleaned from the direct plasma interaction with the seeds, it was necessary to begin the growth trials and collect data on germination, root development, and shoot length. Continuing the growth cycle to full maturation would provide the most data for analysis on physiological development, yield, long duration water uptake, and disease resistance among other traits. The selected seeds require 110 days to reach full maturation and therefore only data on the early developmental stages was collected and will be discussed in the following sections. Overall, the results of the plasma activated water trials provided insight into both beneficial and detrimental effects on the soybean plant and further studied to obtain a greater understanding in how long term physiological development is modified.

A.4 Growth Trials

Air plasma treated growth trials are split into two collective data sets. One treatment set had a 14-day growth period and the second set with a 7-day growth period. Each growth period will be discussed with their respective data set. Growth trials were initially started with 13 different treatment sets shown in Table A-1 utilizing the EHT NSP-120 power supply and allowed to grow over a two-week period. The different treatments were chosen over a broad power deposition range in order to perform a broad study for proof-of-concept before narrowing down to a more specific voltage, frequency, and pulse width range. Table A-5 is a representation of the 14-day growth trial treatment parameters. The results of the two-week trials had led to selection of the best treatment parameters to be continued for further testing. Each of the 'Batch' trials was chosen from the preliminary results with best germination, root development, and growth seen.

Following the initial trials, additional treatments were implemented to explore various pulse widths as well as shorter duration treatment times. Further exploration of these parameters is left for future work but the second set of growth trials as well as any of the argon feedstock gas treatments involved the parameters seen in Table A-5.

Table A-5: Categorized power supply settings for the EHT NSP-120 during the treatments for the growth trials. These settings were determined from previous proof-of-concept preliminary data results. The treatment names are arbitrary and provide no context to the supply settings.

Treatment Name	Voltage (kV)	Frequency (kHz)	Time	Pulse Width (ns)
Batch #1	**14**	**2**	**20 min**	**60**
Batch #2	**14**	**2**	**15 min**	**60**
Batch #5	**14**	**2**	**3 min**	**60**
Batch #9	**12**	**4**	**15 min**	**60**
Batch #12	**14**	**3**	**3 min**	**60**
W18-1	**16**	**3**	**30 s**	**60**
W18-2	**16**	**3**	**30 s**	**120**
W18-3	**18**	**3**	**30 s**	**60**
N-1	**18**	**2**	**2 min**	**60**
N-2	**10**	**3**	**7 min**	**30**
E-1	**15**	**2**	**5 min**	**90**
R-1	**12**	**2**	**10 min**	**60**

The results of this section were performed with the 14-day trial set parameters as well as the new exploratory treatments. The differences in visual plasma observations have been excluded for brevity. The newer treatments involved sub-minute long treatment sets. A shorter duration treatment time is desired to be explored for the essence of economics of plasma generation but is outside the scope of this thesis.

A.4.1 Air growth trials

Air growth trials were conducted in two separate experimental campaigns. The first preliminary testing involved 14-day growth trials in which the top treatments were chosen for continued testing for the 7-day growth trials. This transition was made such that more data could be collected in a more manageable timeline with quicker

experimental turnaround. The growth trial plants were carefully harvested by gently removing the plant from the flat and placing the roots with soil still attached to them in a few centimeters of water. This was done in order to soften up the dirt that attached to the root system. They were only allowed to soak for a few minutes in order to prevent any effect on the plant itself. The soaking of the plants in water is shown in Figure A-9.

Figure A-9: A captured image of the freshly harvested soybeans after the 14-day growth trial.

The 14-day growth trials were done over a broad parameter range with treatment duration times on the order of minutes. Figure A-10 shows the resulting data of three treatments (Batch #1, Batch #2, and Batch #12) and the control group. The germinated seeds were placed into four differing categories based upon the length of the primary root or taproot at the end of the four-day, controlled experiment. Category nomenclature was designated as short (0-3 cm), medium (3-6 cm), long (6-9 cm), very long (9-12 cm), and other as 12+ cm in length. As one can see, the dominating portion of each respective chart is within the short taproot length range with percentages ranging from 50-74%. The average germination of the different groups over the triplicate data set is seen in the

Figure A-10. The variation in percent germination of these four selected data sets is only 7% from the lowest to highest.

Not represented in the Figure A-10 are treatments that had a significantly negative impact on the germination percentages of the seeds with few or none of the seeds germinating. The treatment parameters resulting in low germination rates were repeated in triplicate.

Overall Batch #1 held a 6% higher germination rate than control group with the other presented data differing by only a few percentage points. Recording the length of the primary root during the germination trials led to the first insight into the plasma induced physiological changes have other than strictly affecting contact angle and water absorption. For instance, not only did Batch #1 have a slightly higher germination rate than the presented data set in Figure A-10, the overall length of the primary root was on average longer. Having a longer taproot is important for the development of the plant. A longer taproot provides benefits such as a better anchor to the soil and able to obtain water from deeper locations during droughts. The fibrous roots, however, are quick to absorb surface water and can also respond more quickly to any fertilizer applications.

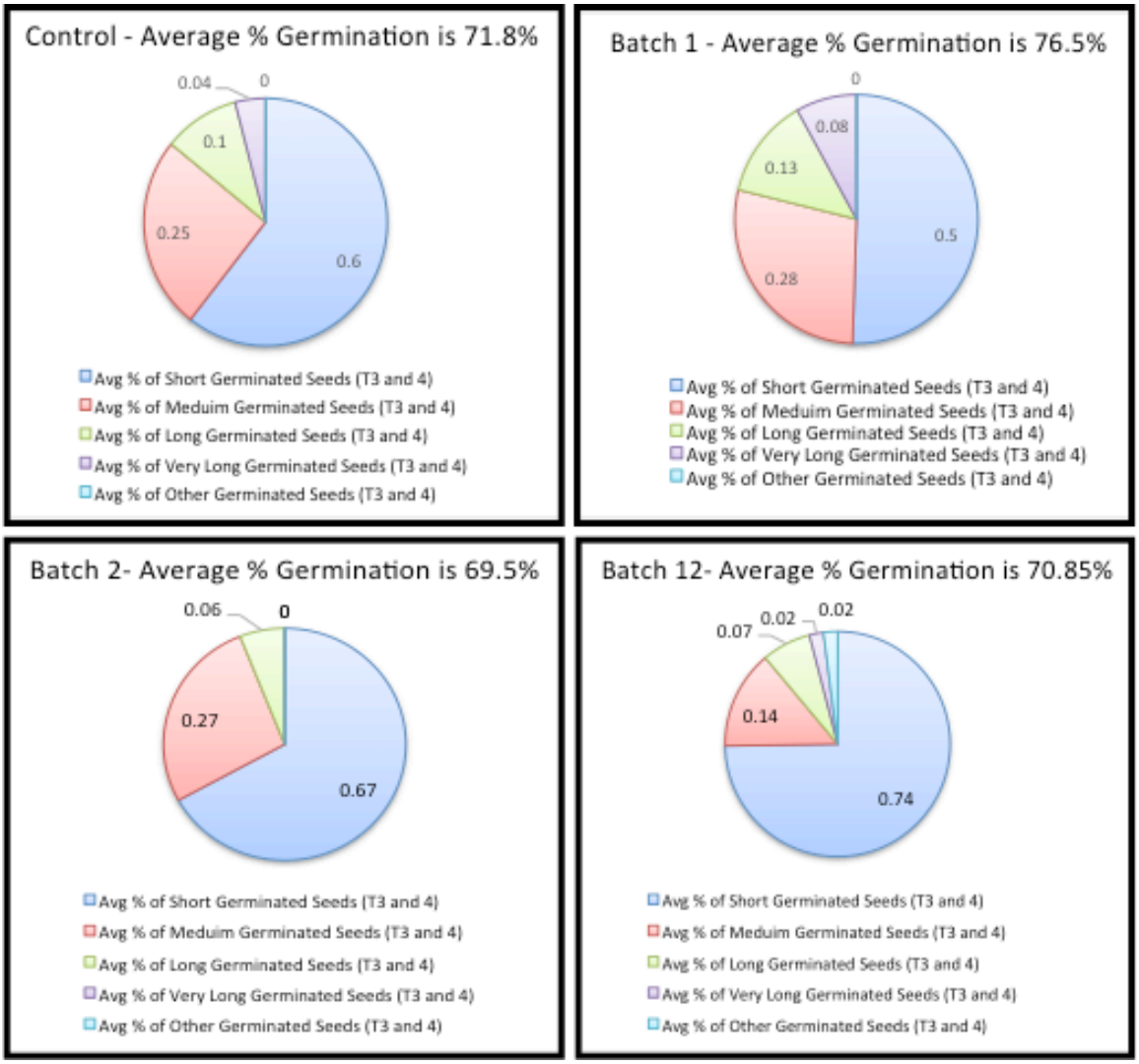

Figure A-10: Plots of the 14-day growth trials comparing the best of Batch #'s 1-12 with the control group are shown in (a-d). Each includes the length of the primary taproot as well as average germination percentages.

The results of the two-week growth trials also included observations on the tertiary or secondary root development of the plants. The plasma treatments were seen to have beneficial and negative impacts on secondary root development. In cases of positive effects, the branching nodes of the primary root were more numerous as well as having a more fibrous branching on each of the offshoots. Counting of each of the secondary and fibrous roots was not performed due to the essence of time. Dry root mass measurements were planned for greater insight for future experimental data collection but

an error was made in the data collection and was never repeated. The roots were cut near the point of emergence and allowed to bake in an oven at 70°C for 45 minutes. An image of roots cut and dried out for the mass measurement in such a procedure is shown in Figure A-11.

Figure A-11: Image in regards to the procedure for how the dry root mass measurements were baked in an oven for 45 minutes. Photo Credit: Joseph Xu, Senior Multimedia Producer at the University of Michigan.

The second set of data collected for air plasma growth trials was the shorter, 7-day growth period that involved the treatment sets of the 14-day growth trials as well as new treatments. The new parameters varied in voltage, frequency, and pulse width but with much shorter treatment durations. The sub-minute treatments were implemented in this data set to elucidate whether or not short treatments would have beneficial physiological effects as well as improving cost-benefit economics. The air growth trials conducted over 7-days resulted in data the led to the *W18-3* treatment having the best positive influence on root development, shoot length, and taproot length as shown in Table A-6. The data present has been placed in descending order based upon the highest average and mean length numbers determined from the data collected.

Table A-6: Results in measurements of the 7-day growth trials.

Treatment Names	Avg. Shoot Length (cm)	Avg. Tap Root Length (cm)	Mean Shoot Length (cm)	Mean Taproot Length (cm)
W18-3	9.35	9.165	10.01	9.25
Batch #5	9.01	8.795	10.1	8.9
R-1	9.41	8.575	9.9	7.9
Control	8.74	8.12	9.29	8.11
N-2	8.41	7.64	8.75	7.225
W18-1	7.68	7.85	8.45	8.5
W18-2	6.61	6.64	6.8	7.05
N-1	7.55	5.98	7.6	6.65
E-1	4.93	3.63	4.5	3.9

Four out of the four growth trials performed when comparing the *W18-3* treatment data to the entire data set resulted in this treatment having the best results out of other treatment sets and the control group. The only time the W18-3 treatment resulted in a second place growth data set was with a different feedstock gas and will be discussed in the concluding remarks of this section. Of all the resulting trials for 7-day growth, 3 out of the 9 selected treatments averaged better than the control groups averaged as shown in Table A-6. Of the 3 treatments that averaged better than the control groups, one set (W18-3) had a treatment duration of 30 seconds with the other two, Batch #5 and R-1, having times of 3 minutes and 10 minutes, respectively. The results of these trials suggest that the shorter treatment times are not only more cost-effective from an economic standpoint but also resulted in an increase in average and mean shoot and taproot lengths over the course of a 7-day grow period.

Some cases led to short primary roots with numerous, fibrous secondary root development whereas a few treatment parameters led to mostly single, lengthy primary roots. Figure A-12 shows an example of root variations of a select few plants from the

control group (a), Batch #2 treatment (b), and Batch #12 parameters (c). Upon investigation of (a), one can see that the primary root of the soybean plant has a primary taproot length of a few centimeters with fibrous secondary roots beginning

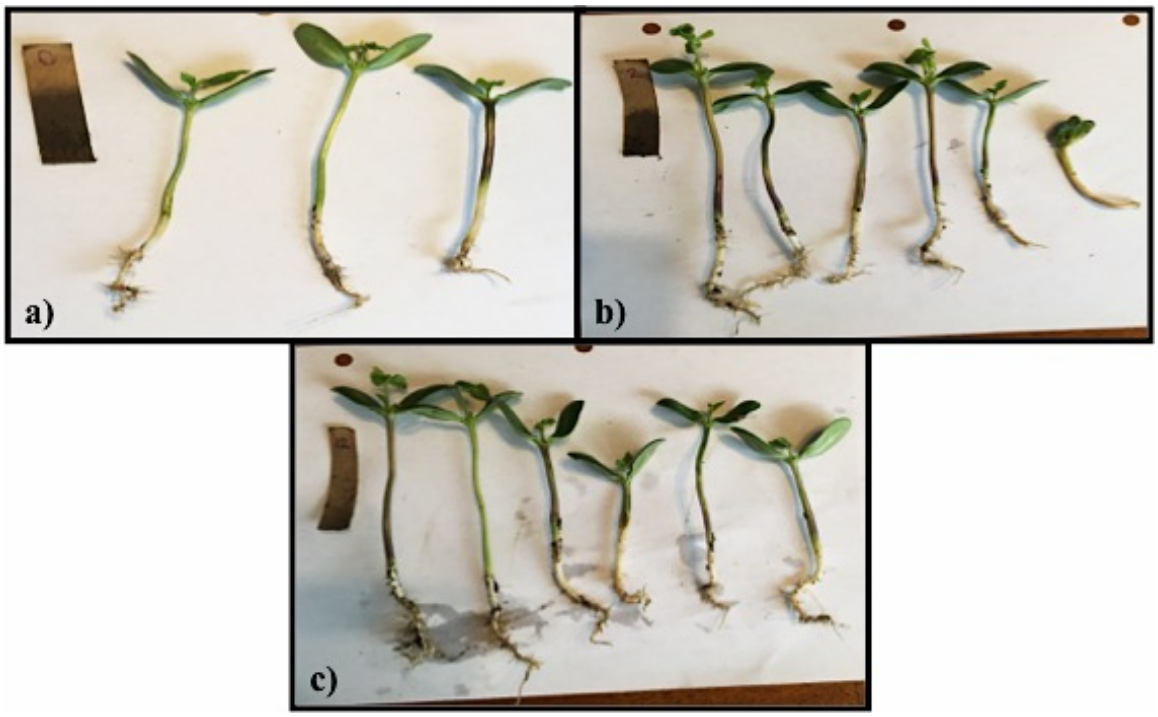

Figure A-12: Image comparing the primary and secondary root development traits of the control (a), Batch #2 (b), and Batch #12 (c).

to develop. The treatment named 'Batch #2' led to visually similar results as seen in (b). Finally, in Figure**Error! Reference source not found.** A-12(c) one can see more significantly more secondary root development as opposed to the images in Figure A-12(a) and (c). The easiest way to observe this difference is to observe the large amount of soil still clinging to the root system. A thorough cleaning was not performed for fear of damaging and removing the secondary roots.

A.4.2 Argon growth trials

Although the air trials were much more numerous in study, some argon plasma treated seed growth studies were also performed and data were recorded. The argon

plasma differs from the air plasma in the variation and population of reactive oxygen and nitrogen species within the packed bed reactor. The populations of the reactive species are controlled by the implementation of argon gas as the plasma generating gas. Since argon is a noble gas and flushes out the air within the reaction chamber, the populations of plasma generated ROS and RNS would be significantly lower than that of air plasma. A point of concern when performing the argon trials was that the seeds had begun to lose germination capabilities due to long-term storage (under non-ideal conditions). The results from the argon treatment trials will be discussed here but only briefly as the experiments should be repeated with fresh seed to better determine plasma-induced effects and not natural biological effects. Table A-7 is a representation of a select few treatments in which the operational parameters were implemented for air and argon feedstock gas supplies.

Table A-7: Tabulated measurement results from the argon gas treatments to the air treatments.

Treatment	Feedstock Gas	AVG. Shoot Length (cm)	AVG. Taproot Length (cm)	Mean Shoot Length (cm)	Mean Taproot Length (cm)
W18-3	**Air**	**9.90**	**8.93**	**10.53**	**8.87**
W18-3	**Argon**	**8.42**	**6.68**	**8.73**	**6.55**
R-1	**Air**	**8.19**	**7.84**	**8.30**	**7.90**
R-1	**Argon**	**8.10**	**4.26**	**8.80**	**4.30**
Control	**N/A**	**9.26**	**7.72**	**9.59**	**7.08**

The tabulated data was acquired for a 7-day growth period. The data in Table A-7 shows that the values for the W18-3 air treatment had the highest averages for shoot and taproot lengths as well as the highest mean values. Although these results were obtained with a smaller data set than the 14-day air treatment trials, the variation in length obtained from the data sets suggests plasma influence on plant development past the stage of germination. These results were also surprising when comparing them to the water

absorption and contact angle measurements presented in the preceding chapter. Argon gas treatments were shown having a lower contact angle and therefore treated seeds were able to absorb more water as confirmed in the water absorption tests. The benefit of being able to absorb more water did not directly correlate to more rapid growth development as presented by the comparison of values between the W18-3 air and W18-3 argon sets. The average shoot length of the air set was 1.48 centimeters longer with the taproot length holding a 2.25 cm increase. The mean of the shoot and taproot lengths were also 1.8 and 2.22 cm higher for the air treatment, respectively. The differences in the argon and air trials from water absorption and contact angle measurements to the early stages of physiological development suggest the important role that the plasma generated ROS and RNS might play.

Overall, the W18-3 data set with a shorter duration treatment time had led to more beneficial results than the other treated sets and the control. The control for these results came in a tied second place with another air feedstock gas trial (R-1) and once again insinuating the importance of having ROS and RNS species within the plasma. The tests repeated on a larger scale and for a longer duration grow period would further provide insight into the effects on later stage development.

A.4.3 PAW growth Trials

The second set of PAW was generated for 2 and 6-minute durations using the AC Elgar supply. This method had a greater influence on the plasma pH than the FID nanosecond pulsers with the pH of the water for the 6-minute treatment getting as low as 4.21. Such a low pH of the water generated positive results on the germination and development of the soybean seeds over the 7-day growth period. The results on the physiological development of the soybean utilizing plasma activated water is presented in

Table A-8. The results of these tests are preliminary and should still be further investigated with increased number of studied plants.

Table A-8: Tabulated results from the 7-day growth trials that implemented plasma activated water instead of direct seed treatment.

Treatment	Duration	AVG. Shoot Length (cm)	AVG. Taproot Length (cm)	Mean Shoot Length (cm)	Mean Taproot Length (cm)
Steam Jet	**15 mins.**	**7.67**	**7.12**	**7.45**	**5.8**
Steam Jet	**5 mins.**	**7.09**	**5.26**	**6.85**	**5**
Bubble Jet	**5 mins.**	**9.14**	**9.16**	**9.5**	**8.7**
Bubble Jet	**15 mins.**	**11.18**	**7.58**	**11.3**	**7.7**
Elgar	**6 mins.**	**8.81**	**8.68**	**10.05**	**7.9**
Elgar	**2 mins.**	**11.51**	**7.97**	**11.6**	**7.4**
Control	**N/A**	**8.90**	**6.81**	**9.57**	**6.70**

Soybeans typically grow well in a slightly acidic soil with the optimal pH range between 6.3 and 6.5.[129] The low pH of the PAW generated with the Elgar supply seemed helped to simulate the acidity and seemed to help promote germination. Overall the 2-minute Elgar PAW data set with a pH of 6.5 seemed to have the best results of the entire data set. The shoot length was an average of 2.59 cm longer than the control with the taproot being 1.16 cm longer on average. The group that performed the second best utilized the FID GmbH nanosecond pulser for a duration of 15 minutes and was similar to the Elgar 501SL supply with average shoot length being 0.4 cm less and average taproot 0.39 cm less. If either of these supplies were implemented on an industrial scale for applications in agriculture, a cost analysis would be performed based upon power consumption and the more efficient per kilowatt-hour system would be preferred.

This conclusion, however, should be further investigated, as the pH of the water was not the only property to be affected by the plasma interaction. The nitrate and nitrite levels of the water changed as well as the peroxide levels. In order to gain a better

understanding of the effects on pH, on soybean germination and growth, a more controlled study should be performed without plasma treatment and only manipulation of the various water properties.

A.4.4 Concluding Remarks

The results of the various experimental parameters previously discussed have shown that plasma treatment of soybeans and plasma activated water has the potential to beneficially effect the physiological development of soybeans during the germination and early growth stages. Germination results have shown that the treatment of seeds with air show improvements over an untreated control and with argon as the feedstock gas resulting in slightly negative effects. Growth trials of the 14-day and 7-day experimental campaigns have shown that plasma effects shoot length by increasing the average height of the plants as well as increasing the average length of the taproot. These results correlate oppositely to the higher water absorbing treatments in the previous chapter and suggest that although argon feedstock gas treatments increase water absorption, the ROS and RNS generated in air-based plasma cause a more beneficial biological response.

A.4.5 Anecdotal evidence of an effect

During the growth trials, 2-4 treated sets were recorded with better physiological development than the control. A similar amount would have results comparable to the control group with the remainder performing poorly. These results occurred consistently over 9 separate growing trials comparing the entire set of the differing treatment parameters. A final, 10^{th} round of treatment sets was also recorded during the campaign in which the seeds were set to germinate in grow in unfavorable temperature conditions with the background temperature stabilizing near 20°C which is 9.5°C below the favored temperature range of the *Glycine max.*[130] Low temperatures are known to retard seedling

emergence and leaf development causing the emergence stage to vary from 5 to 15 days. Visual observation of this data set before harvesting had shown the entirety of the treated set performing more optimistically than the untreated control. By this, the stem of the treated plants were on average nearly 3 centimeters longer in length than the control group and had more secondary root development than the control with comparable taproot length. The results of this test were set to be repeated within a walk-in climate controlled system in order to ensure repeatability of the test but the facility was never acquired. A future study of plasma treatment allowing germination of the plants in harsher environments might lead to an extension of the growing season from the current timeline by an estimation of a week and therefore promote socio-economic change for farmers in various climate regions.

A.5 Future work

The resulting efforts presented in this Appendix and the preceding Chapter V have led to numerous discussions involving extensive experimental campaigns of current studies and new directions to pursue. First, all of the experiments of interest should be repeated on a large scale in a controlled environment such as the botanical gardens at the University of Michigan. The data collection of at least 14-day growth trials would include germination results, shoot length, taproot length, noted comments, as well as dry root mass measurements. From significant data collected on increased quantities of treated soybeans, a better understanding of the plasma effects may be learned. Following the controlled environment studies, plants would need to be evaluated on the outdoor, acre size scale otherwise known as test plots should be selected randomly and at least a ten-plant sample for every 10 acres to determine an average stage of development.[131] The

test plot studies would show how the seeds would respond in an uncontrolled environment and determine the viability of the treatments for real-world implementation.

During the large-scale growth trials, experiments within the laboratory setting should be performed simultaneously that involve characterizing the plasma as well as species produced in the reaction chamber. More involved work with optical emission spectroscopy, laser induced fluorescence, Fourier Transform InfraRed (FTIR) analysis, and mass spectroscopy gas chromatography would characterize the entirety of the treatments. This data could then be used and correlated with that in the published literature of the nutritional needs of the treated plant and further optimize the treatment. Another laboratory scale test that would be of interest is the repeating of a cold environment for germination characteristics. The results mentioned in the anecdotal section of this chapter were quite unexpected and exploration of the reasons behind this would be of interest to the agricultural community.

BIBLIOGRAPHY

[1] D.B. Graves. "Low temperature plasma biomedicine: A tutorial review," Phys. Plasmas **21**, 080901 (2014).

[2] F.F. Chen. *Introduction to Plasma Physics and Controlled Fusion.* 1984.

[3] M. A. Lieberman and A. J. Lichtenberg. *Principles of plasma Discharges and Materials Processing.* 2nd edn. Wiley & Sons, Inc. 2005.

[4] R. Brandenburg. "Topical Review – dielectric barrier discharges: progress on plasma sources and on the understanding of regimes and single filaments," Plasma Sources Sci. Technol. **26**, (2017) 053001.

[5] U. Ebert and D. D. Sentman. "Streamers, Sprites, Leaders, Lightning: from micro- to macro-scales," J. Phys. D: Appl. Phys. **41**, (2008).

[6] X. Tu, H.J. Gallon, and J.C. Whitehead. "Transition behavior of packed-bed dielectric barrier discharge in argon," IEEE Trans. On Plasma Sci. **39**, 2172-2173(2011).

[7] X. Tu, B. Verheyde, S. Corthals, S. Paulussen, and B.F. Sels. "Effect of packing solid material on characteristics of helium dielectric barrier discharge at atmospheric pressure," Phys. Plasmas **18**, 080702 (2011).

[8] W. Siemens. Poggendorff's Ann. Phys. Chem. **102**, 66 (1857).

[9] U. Kogelschatz. "Dielectric-barrier discharges: their history, discharge physics, and industrial applications," Plasma Chem. Plasma Proc. **23**, 1-46 (2003).

[10] M.A. Lieberman and A.J. Lichtenberg. *Principles of plasma discharges and materials processing.* 2nd edn. Wiley. (2005).

[11] R. Brandenburg. "Dielectric barrier discharges: progress on plasma sources and on the understanding of regimes and single filaments," Plasma Sources Sci. Technol. **26**, 053001 (2017).

[12] S. Liu and M. Neiger. J. Phys. D **34**, 1632 (2001).

[13] J. Kruszelnicki, K.W. Engeling, J.E. Foster, and M.J. Kushner. "Propagation of negative electrical discharges through 2-dimensional packed bed reactors," J. Phys. D: Appl. Phys. **50**, 2016.

[14] T.C. Manley. "The electric characteristics of the ozonator discharge," Trans. Electrochem. Soc. **84**, 83-96 (1943).

[15] A.V. Pipa and R. Brandenburg. "The equivalent circuit approach for the electrical diagnostics of dielectric barrier discharges: the classical theory and recent developments," Atoms. (2019).

[16] X.-M. Zhu and Y.-K. Pu. "Optical emission spectroscopy in low-temperature plasmas containing argon and nitrogen: determination of the electron temperature and density by the line-ratio method," J. Phys. D: Appl. Phys. **43**, 403001 (2010).

[17] M.A. Lieberman and A.J. Lichtenberg. *Principles of plasma discharges and materials processing.* 2nd edn. Wiley & Sons. (2005).

[18] H.L. Chen, H.M. Lee, S.H. Chen, and M.B. Chang. "Review of Packed-bed plasma reactor for ozone generation and air pollution control," Ind. Eng. Chem. Res. **47**, 2122-2130 (2008).
[19] L.B. Loeb and J.M. Meek. "The mechanism of spark discharge in air at atmospheric pressure," J. of Appl. Physic. **11**, 438 (1940).
[20] C. Montijn and U. Ebert. "Diffusion correction to the Raether-Meek criterion for the avalanche-to-streamer transition," J. Phys. D: Appl. Phys. **39**, 2979-2992, (2006).
[21] I. Michielsen, Y. Uytdenhouwen, A. Bogaerts, and V. Meynen. "Altering conversion and product selectivity of dry reforming of methane in a dielectric barrier discharge by changing the dielectric packing material," *Catalysts.* **9**, (2019).
[22] X. Tu, B. Verheyde, S. Corthals, S. Paulussen, and B.F. Sels. "Effect of packing solid material on characteristics of helium dielectric barrier discharge at atmospheric pressure," Phys. Plasmas. **18**, 080702 (2011).
[23] T. Butterworth, R. H. Elder, and R. W. K. Allen. "Effects of particle size on CO_2 reduction and discharge characteristics in a packed bed plasma reactor,"*Chem. Engin*. *J.* **293** (2016) 55-67.
[24] H.P. Nguyen, M.J. Park, S.B. Kim, H.J. Kim, L.J. Baik, and Y.M. Jo. "Effective dielectric barrier discharge reactor operation of decomposition of volatile organic compounds," J. of Cleaner Production **198**, 1232-1238 (2018).
[25] Z. Ye et al. "An in-depth investigation of toluene decomposition with a glass beads packed bed dielectric barrier discharge reactor," Ind. Eng. Chem. Res. **56**, 10215-10226 (2017).
[26] A.M. Vandenbroucke, R. Morent, N. De Geyter, and C. Leys. "Review: Non-thermal plasmas for non-catalytic and catalytic VOC abatement," J. Haz. Mat. **195**, 30-54 (2011).
[27] T. Butterworth and R.W.K. Allen. "Plasma-catalyst interaction studied in a single pellet DBD reactor: dielectric constant effect on plasma dynamics," Plasma Sources Sci. Technol. **26**, 065008 (2017).
[28] S. Pancheshnyi, B. Eismann, G.J.M. Hagelaar, L.C. Pitchford, Computer code ZDPlasKin, http://www.zdplaskin.laplace.univ-tlse.fr (University of Toulouse, LAPLACE, CNRS-UPS-INP, Toulouse, France, 2008).
[29] E. Choiniere and B.E. Gilchrist. "Self-consistent 2-D kinetic simulations of high-voltage plasma sheaths surrounding ion-attracting conductive cylinders in flowing plasmas," IEEE Trans. On Plasma Sci. **35**, 2007.
[30] http://www.comsol.com.
[31] K. Van Laer and A. Bogaerts. "Fluid modeling of a packed bed dielectric barrier discharge plasma reactor," Plasma Scources Sci. Technol. **25**, 015002 (2016).
[32] W. Wang, H-H. Kim, K. Van Laer, and A. Bogaerts. "Streamer propagation in a packed bed plasma reactor for plasma catalysis applications," Chem. Eng. J.. 334 (2018) 2467-2479.
[33] I. Michielsen, Y. Uytdenhouwen, J. Pype, B. Michielsen, J. Mertens, F. Reniers,

V. Meynen, and A. Bogaerts. "CO_2 dissociation in a packed bed DBD reactor: First steps towards a better understanding of plasma catalysis," Chem. Eng. J. **326**, 477-488 (2017).

[34] W.C. Chung, I.Y. Tsao, and M.B. Chang. "Novel plasma photocatalysis process for syngas generation via dry reforming of methane," Energy Conversion and Management, **164** 417-428 (2018).

[35] M. Okubo, H. Yamada, K. Yoshida, and T. Kuroki. "Simultaneous reduction of diesel particulate and NO_x using catalysis combined nonthermal plasma reactor," Proc. 2016 Electrostactics Joint Conference.

[36] Y. Cheng, W. Song, J. Liu, H. Zheng, Z. Zhao, C. Xu, Y. Wei, and E. J. M. Hensen. "Simultaneous NO_x and particulate matter removal from diesel exhaust by hierarchical Fe-doped Ce-Zr oxide," *ACS Catal.* 2017. **7**, 3883-3892.

[37] J. Hoard, R. L. Bretz, and Y Ehara. "Diesel exhaust simulator: design and application to plasma discharge testing," SAE Technical Paper Series. *2003 SAE World Congress, Detroit, Michigan* March 3-6, 2003.

[38] Ch. Subrahmanyam, M. Magureanu, A. Renken, and L. Kiwi-Minsker. "Catalytic abatement of volatile organic compounds assisted by non-thermal plasma: Part 1. A novel dielectric barrier discharge reactor containing catalytic electrode," Applied Catalysis B: Environmental. **65**, 150-156 (2006).

[39] H.H. Kim and A. Ogata. "Nonthermal plasma activates catalyst: from current understanding and future prospects," Eur. Phys. J. Appl. Phys. **55**, 12806 (2011).

[40] E.I. Karpenko, V.E. Messerle, A.B. Ustimenko. "Plasma-aided solid fuel combustion," Proceedings of Combustion Institute **31**, 2252-2260 (2007).

[41] D.A. Lacose, D.A. Xu, J.P. Moeck, and C.O. Laux. "Dynamic response of a weakly turbulent lean-premixed flame to nanosecond repetitively pulsed discharge," Proceedings of the Combusion Institute **34**, 3259-3266 (2013).

[42] M. T. Lanagan. J. K. Yamamoto, A. Bhalla and S. G.Sankar, "The dielectric properties of yttria-stabilized zirconia," Matls. Lett. **7**, 437 (1989).

[43] B. W. Hakki and P. D. Coleman, "A dielectric resonator method of measuring inductive capacities in the millimeter range", IRE Trans. Microwave Theory Techn., **8**, 402 (1960).

[44] A Bogearts et al., "CO_2 conversion by plasma technology: insights from modeling the plasma chemistry and plasma reactor design", Plasma Sources Sci. Technol. **26,** 063001 (2017).

[45] T. Butterworth, R. Elder and R. Allen, "Effects of particle size on CO2 reduction and discharge characteristics in a packed bed plasma reactor", Chem. Engr. J. 293, 55 (2016).

[46] N. Y. Babaeva, A. N. Bhoj and M. J. Kushner, "Streamer dynamics in gases containing dust particles, Plasma Source Sci. Technol. **15**, 591 (2006).

[47] S. A. Norberg, E. Johnsen and M. J. Kushner, Plasma Sources Sci. Technol. **24,** 035026 (2015).

[48] R. Dorai and M. J. Kushner, J. Phys. D. Appl. Phys. **36,** 666 (2003).

[49] J. Kruszelnicki, K.W. Engeling, J. E. Foster, Z. Xiong, and M. J. Kushner. "Propagation of negative electrical discharges through 2-dimensional packed bed reactors", J. Phys. D. Appl. Phys. **50,** 025203 (2016).

[50] T. Butterworth, R. Elder and R. Allen, "Effects of particle size on CO2 reduction and discharge characteristics in a packed bed plasma reactor", Chem. Engr. J. 293, 55 (2016).
[51] S. Tsukamoto, T. Namihira, H. Hori, K. Shinozaki, S. Katsuki, R. Hackam, et al. "An analysis of pulsed streamer discharge using a high-speed camera", Proceedings of Pulsed Power Plasma Science, Las Vegas, USA, (2001).
[52] E. C. Neyts, K. Ostrikov, M. K. Sunkara, and A. Bogaerts. "Plasma Catalysis: Synergistic effects at the nanoscale," Chemical reviews 115 **24,** 13408-13446 (2015).
[53] D. Mei, X. Zhu, C. Wu, B. Ashford, P. T. Williams, and X. Tu. "Plasma-photocatalytic conversion of CO_2 at low temperatures: Understanding the synergistic effect of plasma-catalysis," Applied Catalysis B: Environmental **182**, 525-532 (2016).
[54] J.C. Whitehead. "Plasma catalysis: A solution for environmental problems," Pure and Applied Chemistry. **82** (2010).
[55] J.C. Whitehead. "Plasma-catalysis: the known knowns, the known unknowns and the unknown unknowns," J. Phys. D: Applied Physics **49**, 243001-243024 (2016).
[56] Laux, C.O., "Radiation and Nonequilibrium Collisional-Radiative Models," von Karman Institute Lecture Series 2002-07, Physico-Chemical Modeling of High Enthalpy and Plasma Flows, eds. D. Fletcher, J.-M. Charbonnier, G.S.R. Sarma, and T. Magin, Rhode-Saint-Genèse, Belgium, 2002.
[57] M. S. Simeni, B.M. Goldberg, C. Zhang, K. Frederickson, W.R. Lempert, and I.V. Adamovich. "Electric field measurements in a nanosecond pulse discharge in atmospheric air," J. Phys. D: Appl. Phys. **50** (2017).
[58] N.M. Jordan, Y.Y. Lau, D. French, R. Gilgenbach, and P. Pengvanich. "Electric field and electron orbits near a triple point," J. Appl. Phys. **102**, 033301 (2007).
[59] Michielsen, Y. Uytdenhouwen, J. Pype, B. Michielsen, J. Mertens, F. Reniers, V. Meynen, and A. Bogaerts. "CO2 dissociation in a packed bed DBD reactor: First steps towards a better understanding of plasma catalysis," Chemical Engineering Journal 326, 477-488, (2017).
[60] M. Kraus, B. Eliasson, U. Kogelschatz, and A. Wokaun. "CO2 reforming of methane by the combination of dielectric-barrier discharges and catalysis," Phys. Chem. Chem. Phys., 3, 294-300. (2001).
[61] M. Abdul Mujeebu, M.Z. Abdullah, M.Z. Abu Bakar, A.A. Mohamad, and M.K. Abdullah."Applications of porous media combustion technology – A review,". Applied energy 86, 1365-1375 (2009).
[62] Z. Machala, M. Janda, K. Hensel, I. Jedlovsky, L. Lestinska, V. Foltin, V. Martisovits, and M. Morvova. "Emission spectroscopy of atmospheric pressure plasma for bio-medical and environmental applications," Journal of Molecular Spectroscopy 243, 194-201, (2007).
[63] J.E. Foster, S. Mujovic, J. Groele, I. M. Blankson. "Towards high throughput plasma based water purifiers: design considerations and the pathways towards practical application," J. of Phys. D.: Appl. Phys. 51, 29 (2018).
[64] H.H. Kim and A. Ogata. "Nonthermal plasma activates catalyst: from current understanding and future prospects," Eur. Phys. J. Appl. Phys. 55, 13806 (2011).

[65] R. M. Wheeler. “Agriculture for Space: People and places paving the way,” Open Agriculture. 2, 14-32 (2017).
[66] L. Ling, J. Jiafeng, L. Jiangang, S. Minchong, H. Xin, S. Hanliang, and Dong Yuanhua. ‘Effects of cold plasma treatment on seed germination and seedling growth of soybean,’ Scientific reports 4, 5859 (2014).
[67] L. Sivachandiran and A. Khacef. ‘Enhanced seed germination and plant growth by atmospheric pressure cold air plasma: combined effect of seed and water treatment,’ RSC Adv., 7, 1822-1832 (2017).
[68] P. Puligundla, Je-Wook Kim, and C. Mok, “Effect of corona discharge plasma jet treatment on decontamination and sprouting of rapeseed (Brassica napus L.) Seeds,” Food Control 71, 376-382, (2017).
[69] I. Filatova, V. Azharonok, E. Gorodetskaya, L. Mel’nikova, O. Shedikova, and A. Shik. “Plasma-radiowave stimulation of plant seeds germination and inactivation of pathogenic microorganisms.” (Jan. 2009).
[70] K. Matra. “Non-thermal plasma for germination enhancement of radish seeds,” 2016 International Electrical Engineering Congress, iEECON2016, 2-4 March 2016, Chiang Mai Thailand. Procedia Computer Science 86, 132-135 (2016).
[71] J. Jiang and J. Li. “Effect of cold plasma treatment on seed germination and growth of wheat,” Plasma Science and Technology, 16, (2013).
[72] L.D. Nooden, K. A. Blakley, and J. M. Grzybowski. “Control of Seed Coat thickness and permeability in soybeans,” Plant. Physiol. 79, 543-545 (1985).
[73] J.J. Zhang, J.O. Jo, D.L. Huynh, R.K. Mongre, M. Ghosh, A.K. Singh, S.B. Lee, Y.S. Mok, P. Hyuk, and D.K. Jeong. “Growth-inducing effects of argon plasma on soybean sprouts via the regulation of demethylation levels of energy metabolism-related genes,” Sci. Rep. 7, 41917 (2017).
[74] P. Held. “An introduction to reactive oxygen species measurement of ROS in Cells,” Biotech Instruments, 1-14. (2012).
[75] H. El-Maarouf-Bouteau and C. Bailly. “Oxidative signaling in seed germination and dormancy,” Plant Signaling & Behavior 3, 175-182. (March 2008).
[76] A.J. de Jong, E. T. Yakimova, V. M. Kapchina, and E. J. Woltering. “A critical role for ethylene in hydrogen peroxide release during programmed cell death in tomato suspension cells.” Planta 126, 156-166 (2002).
[77] T. Jabs, R. A. Dietrich, and J. L. Dangl. “Initiation of runaway cell death in an Arabidopsis mutant by extracellular superoxide,” Science. 27, 1853-1856 (1996).
[78] J. H. Joo, Y.S. Bae, and J. S. Lee. “Role of auxin-induced reactive oxygen species in root gravitropism,” Plant Physiol. 126, 1055-1060 (2001).
[79] K. Cui, G. Xing, X. Liu, G. Xing, and Y. Wang. “Effect of hydrogen peroxide on somatic embryogenesis of Lycium barbarum L.,” Plant Sci. 146, 9-16 (1999).
[80] J. P. Wisniewski, P. Cornille, J. P. Agnel, and J. L. Montillet. “The extension multigene family responds differentially to superoxide or hydrogen in tomato cell cultures,” FEBS Lett. 447, 264-268 (1999).
[81] L.K. Randeniya and G. J. J. B. de Groot. “Non-thermal plasma treatment of agricultural seeds for stimulation of germination, removal of surface contamination and other benefits: A review,”. Plasma Process. Polym. 12, 608-623 (2015).

[82] Kelly-Wintenberg, K. Hodge, A. Montie, T. C., Deleanu, L., Sherman, D., Roth, J. R., et al. "Use of a one atmosphere uniform glow discharge plasma to kill a broad spectrum of microorganisms," Journal of Vacuum Science & Technology A, 17, 1539-1544 (1999).

[83] Lee, K., Paek, K. H., Ju, W. T., and Lee, Y. "Sterilization of bacteria, yeast, and bacterial endospores by atmospheric-pressure cold plasma using helium and oxygen," Journal of Microbiology, 44, 269-275 (2006).

[84] Shintani, H., Sakudo, A., Burke, P., and McDonnell, G. "Gas plasma sterilization of microorganisms and mechanisms of action. Experimental and therapeutic medicine," 1, 731-738 (2010).

[85] K. W. Engeling, J. Kruszelnicki, M. J. Kushner, and John E. Foster. "Time-resolved evolution of micro-discharges, surface ionization waves and plasma propagation in a two dimensional packed bed reactor," Plasma Sources Sci. and Techn. Vol 27. (2018).

[86] Electrotechnologies for extraction from food plants and biomaterials. Editors: E. Vorobiev & N. Lebovka. Food Engineering Series, (2008).

[87] P. Bruggeman and C. Leys. "Topical Review: Non thermal plasmas in and in contact with liquids," J. of Phys. D.: Appl. Phys. 42, (2009).

[88] J. Foster, B. Weatherford, E. Gillman, and B. Yee. "Underwater operation of a DBD plasma jet," Plasma Sources Sci. Technol. 19, 025001 (2010).

[89] Y. Yuan and T. Randall Lee. "Chapter 1: Contact Angle and Wetting Properties," G. Bracco, B. Holst (eds.), Surface Science Techniques, Springer Series in Surface Sciences 51, (2013).

[90] Stuart O. Nelson. "Dielectric Properties of Agricultural Materials and their Applications," Elsevier Inc. (2015). ISBN: 978-0-12-802305-1.

[91] J. Kruszelnicki, K. W. Engeling, John E. Foster, Z. Xiong, and M. J. Kushner. "Propagation of negative electrical discharges through 2-dimensional packed bed reactors," J. of Phys. D.:Appl. Phys. 50, 025203 (2017).

[92] A. Vesel, I. Junkar, U. Cvelbar, J. Kovac, and M. Mozetic. "Surface modification of polyster by oxygen- and nitrogen-plasma treatment," Sur. Interface Anal. 40. 1444-1453 (2008).

[93] M. Gilliam, S. Farhat, A. Zand, B. Stubbs, M. Magyar, and G. Garner. "Atmospheric Plasma Surface Modification of PMMA and PP Micro-Particles," Plasma Process. Polym. 11, 1037-1043 (2014).

[94] W. Van Gaens and A. Bogaerts. "Kinetic modeling for an atmospheric pressure argon plasma jet in humid air," J. of Phys. D.: Appl. Phys. 46. 275201 (2013).

[95] T. Winter et al. "Common versus noble *Bacillus subtilis* differentially responds to air and argon gas plasma," Proteomics. 13, 2608-2621 (2013).

[96] C. V. Piper and W. J. Morse. "The Soybean," McGraw-Hill Book Company, Inc.

[97] "The history of the soybean," Illinois Soybean Association Checkoff Program. Bloomington Illinois.

[98] W. Shurtleff and A. Aoyagi. "History of A.E. Staley Manufacturing Co.: Work with Soy (1867-2018)," Soyinfo Center. Lafeyette, CA. (2018)

[99] R.M. Wik. "Henry Ford and Grassroots America," The University of Michigan Press. 151-152 (1972).

[100] W. Shurtleff and A. Aoyagi. “History of World Soybean Production and Trade.” A chapter from History of soybeans and Soyfoods. Soyinfo Center, Lafeyette, CA. (2004).
[101] L. C. Purcell, M. Salmeron, and L. Ashlock. “Soybean Growth and Development,” *Arkansas Soybean Production Handbook*. (2014).
[102] N.S. Lersten and J.B. Carlson. “Soybeans: Improvement, production and uses,” Vegitative morphology. ASA, CSSA, and SSSA, Madison WI. 15-57 (2004).
[103] F. Ma, E. Cholewa, T. Mohamed, C.A. Peterson, and M. Gijzen. “Cracks in the palisade cuticle of soybean seed coats correlate with their permeability to water,” Ann. Bot., **94**, 213-228 (2004).
[104] D. Qutob, F. Ma, C.A. Peterson, M.A. Bernards, and M. Gijzen. “Structural and permeability properties of the soybean seed coat,” Botany. **86,** 219-227 (2007).
[105] S. Shao, C.J. Meyer, F. Ma, C.A. Peterson, and M.A. Bernards. “The outermost cuticle of soybean seeds: chemical composition and function during imbibition,” J. Exp. Bot. **58**, 1071-1082 (2007).
[106] M. Koizumi, K. Kikiuchi, S. Isobe, N. Ishida, S. Naito, and H. Kano. “Role of seed coat in imbibing soybean seeds observed by micro-magnetic resonance imaging,” Ann. Bot. **102**, 342-352 (2008).
[107] S. Zhou, H. Sekizaky, Z. Yang, S. Sawa, and J. Pan. “Phenolics in the seed coat of wild soybean (*Glycine soja)* and their significance for seed hardness and seed germination,” J. Agric. Food Chem. **58**, 10972-10978 (2010).
[108] S.S. Zamin, and M.A. Ajmal Kahn. “The role of seed coat phenolics on water uptake and early protein synthesis during germination of dimorphic seeds of *Halopyrum mucronatum* (L.) staph,” J. Bot., **42**, 227-238 (2010).
[109] D.T. Vu, V. Velusamy, and E. Park. “Structure and chemical composition of wild soybean seed coat related to its permeability,” Pak. J. Bot., **46**, 1847-157 (2014).
[110] D. Wright and A.W. Lenssen. “Staging Soybean Development,” *Agriculture and Environment Extension Publications,* **191** (2013).
[111] J. Glinski and J. Lipiec. “Soil physical conditions and plant roots,” CRC Press, Boca Raton, FL (1990).
[112] E. Vorobiev and N. Lebovka, (eds.). “Electrotechnologies for extraction from food plants and biomaterials,” Food engineering series book. Springer Science and Business Media LLC. (2008).
[113] E. Vorobiev and N. Lebovka eds. “Electrotechnologies for extraction from food plants and biomaterials,” Food Engineering Series. Springer (2008).
[114] W.S. Meaking, J. Edgerton, C.W. Wharton, and R.A. Meldrum. “Electroporation-induced damage in mammalian cell DNA,” Biochimica et Biophysica Acta **1264**, 357-362 (1995).
[115] D. Jordan. *Ultrawideband Electrochemotherapy.* Dissertation. University of Michigan. 2005.
[116] I. Semenov, S. Xiao, and A.G. Pakhomov. “Electroporation by subnanosecond pulses,” Biochem. Biophys. Rep. 253-259 (2016).
[117] E. Nuemann, A.E. Sowers, and C.A. Jordan. Electroporation and electrofusion in cell biology. Plenium press, New York (1989).
[118] P. Marszalek, D.S. Liu, and T.Y. Tsong. “Schwan equation and transmembrane

potential induced by altering electric field," Biophysical Journal **58**, 1053-1058 (1990).
[119] T. Kotnik, F. Bobanovic, and D. Miklavcic. "Sensitivity of transmembrane voltage induced by applied electric fields – a theoretical analysis," Bioelectrochemistry Bioenergetics **43**, 285-291 (1997).
[120] M. Danfelter, P. Engstrom, B.R.R. Persson, and L.G. Salford. "Effect of high voltage pulses on survival of Chinese Hamster V79 lung fibroblast cells," Bioelectrochemistry and Bioenergetics **47**, 97-101 (1998).
[121] J.J. Zhang, J.O. Jo, D.L. Huynh, R.K. Mongre, M. Ghosh, A.K. Singh, S.B. Lee, Y.S. Mok, P. Hyuk, and D.K. Jeong. "Growth-inducing effects of argon plasma on soybean sprouts via the regulation of demethylation levels of energy metabolism-related genes," Nature: Scientific Reports. **7:41917** (2017).
[122] H. El-Maarouf-Bouteau and C. Bailly. "Oxidative signaling in seed germination and dormancy," Plant Signaling & Behavior. **3** 175-182 (2008).
[123] K. Apel and H. Hirt. "Reactive oxygen species: Metabolism, oxidative stress, and signal transduction," Annul. Rev. Plant Biol. **55**, 373-399 (2004).
[124] C.H. Foyer and G. Noctor. " Redox homeostasis and antioxidant signaling: A metabolic interface between stress perception and physiological responses," Plant Cell. **17**, 1866-1875 (2005).
[125] Y. Wang, G.J. Loake, and C. Chu. "Cross-talk of nitric oxide and reactive oxygen species in plant programmed cell death," Front. Plant Sci. (2013).
[126] https://www.aganytime.com/asgrow/mgt/growing-season/Pages/Stages.aspx
[127] N. Khamsen, D. Onwimol, N. Teerakawanich, S. Dechanupaprittha, W. Kanakbannakorn, K. Hongesombut, and S. Srisonphan. "Rice (*Oryza Sativa* L.) seed sterilization and germination enhancement via atmospheric hybrid nonthermal discharge plasma," ACS Appl Mater. Interfaces. **8**, 19268-19275 (2016).
[128] R. Zhou, J. Li, R. Zhou, X. Zhang, and S. Yang. "Atmospheric-pressure plasma treated water for seed germination and seedling growth of mung bean and its sterilization effect on munb bean sprouts," Innov. Food Sci. and Emerg. Techn. (2018).
[129] M. Staton. "Managing soil pH for optimal soybean production," Michigan State University Extensions. OutreachWeb Article. Accessed 03.31.2019.
[130] R.L. Musser, S.A. Thomas, and P.J. Kramer. "Short and long term effects of root and shoot chilling of ransom soybean," Plant Physiol. **73**, 778-783 (1983).
[131] W.R. Fehr and C.E. Caviness. "Stages of Soybean Development," *Special Report.* 87 (1997).